



12-2018

Interfacing to Biological Systems Using Microfluidics

Peter Golden Shankles

University of Tennessee, pshankle@vols.utk.edu

Follow this and additional works at: https://trace.tennessee.edu/utk_graddiss

Recommended Citation

Shankles, Peter Golden, "Interfacing to Biological Systems Using Microfluidics. " PhD diss., University of Tennessee, 2018.

https://trace.tennessee.edu/utk_graddiss/5315

This Dissertation is brought to you for free and open access by the Graduate School at TRACE: Tennessee Research and Creative Exchange. It has been accepted for inclusion in Doctoral Dissertations by an authorized administrator of TRACE: Tennessee Research and Creative Exchange. For more information, please contact trace@utk.edu.

To the Graduate Council:

I am submitting herewith a dissertation written by Peter Golden Shankles entitled "Interfacing to Biological Systems Using Microfluidics." I have examined the final electronic copy of this dissertation for form and content and recommend that it be accepted in partial fulfillment of the requirements for the degree of Doctor of Philosophy, with a major in Energy Science and Engineering.

Scott T. Retterer, Major Professor

We have read this dissertation and recommend its acceptance:

Steven M. Abel, Mitchel J. Doctycz, Jennifer L. Morrell-Falvey

Accepted for the Council:

Dixie L. Thompson

Vice Provost and Dean of the Graduate School

(Original signatures are on file with official student records.)

Interfacing to Biological Systems Using Microfluidics

**A Dissertation Presented for the
Doctor of Philosophy
Degree**

The University of Tennessee, Knoxville

Peter Golden Shankles

December 2018

Copyright © 2018 by Peter Golden Shankles
All rights reserved.

DEDICATION

I dedicate this work to David Shankles. I hope to live my life as intensely and as fully as he lived the 19 years he was given on this Earth.

ACKNOWLEDGEMENTS

This dissertation would not be possible without all the people that helped me along the way. I would like to thank my family for supporting me through the years with steady encouragement, a positive disposition, and reminders that success is multifaceted. I would also like to thank my girlfriend, Jenna, who has been my biggest supporter through the ups and downs of grad school. And to my lab mates and classmates, community and sharing ideas have added depth to the papers that makeup this dissertation. Finally, thank you to my advisor who taught me to ask important questions and build knowledge to share with others.

ABSTRACT

Biological systems operate on scales ranging from nanoscale chemical reactions to the global flow of nutrients and energy. Building knowledge of each level requires techniques and technologies that can address the biological system at the chosen level of interest. On the cellular and community levels, microfluidics are able to replicate the spatial scales of the natural system from the cellular, to community through the local microenvironment while providing engineering solutions to control flow through the system and interfaces with the system through microscopy and chemical sampling. Herein, biological interfaces were created using microfluidics to control cellular interactions and chemical reactions. At the subcellular scale, molecular exchange bioreactors enhanced the protein production of a cell-free protein synthesis system by using a microscale serpentine channel to reduce lateral diffusion distances. Size dependent transport of reactants into, and byproducts out of, the reaction channel through the nanoporous barrier extended the reaction time and enhanced protein yield. Nanoporous membranes were also developed for studying cellular interactions. Membranes confined cells within culture chambers while allowing transport of nutrients and signal molecules between the chambers and support channels. Quorum sensing within the microfluidic chambers was modeled using a quasi-steady-state PDE based approach to estimate relative concentrations. The platform facilitated the use of brightfield imaging and analysis to characterize morphological changes of a growing biofilm as the oral microbe *Streptococcus gordonii* formed aggregates only when co-cultured adjacent to *Fusobacterium nucleatum*. The investment of capital and time to start incorporating microfluidic into research can be prohibitive. To combat this, tools were created to provide researchers the ability to create microfluidics using 3D printing to simplify the process and remove the need for cumbersome and expensive cleanroom facilities. The technique was used in two common microfluidic applications of

chemical gradient and droplet formation in addition to building 3D fluidics that cannot be replicated directly with microfabrication techniques. These microfluidics controlled the spatiotemporal environment on the scales of biological systems to enhance the effectiveness of protein synthesis, give insight to morphological effects of cell signaling, and introduced technology to enable others to do the same.

TABLE OF CONTENTS

| | |
|---|----|
| CHAPTER 1 INTRODUCTION..... | 1 |
| Microfluidics..... | 1 |
| Cell-Free Protein Synthesis Systems | 3 |
| 3D Printed Microfluidics | 4 |
| Microfluidic Cell Culture | 6 |
| Cell Signaling..... | 8 |
| Biofilms | 10 |
| Oral Microbiome | 11 |
| Modeling Bacterial Growth and Signaling | 13 |
| Research Aims | 14 |
| CHAPTER 2 FABRICATION OF NANOPOROUS MEMBRANES FOR TUNING MICROBIAL INTERACTIONS AND BIOCHEMICAL REACTIONS..... | 17 |
| Abstract | 20 |
| Introduction..... | 21 |
| Experimental..... | 24 |
| Nanoporous Exchange Device..... | 24 |
| Electron Beam Lithography | 26 |
| Microchannels | 26 |
| Reactive Ion Etching of Fluidic Network and Membrane | 27 |
| Silicon Dioxide Coating of Nanopores | 27 |
| Device Testing..... | 28 |
| Cell Culture Device | 29 |
| Photolithography | 29 |
| PDMS Casting and Device Bonding | 31 |
| Device Testing and Cell Culture | 32 |
| Results and Discussion | 33 |
| Nanoporous Exchange Device..... | 33 |

| | |
|--|----|
| Cell Culture Device | 37 |
| Summary and Conclusions..... | 40 |
| Acknowledgements | 41 |
| CHAPTER 3 A NANOSTRUCTURED CO-CULTURE ENVIRONMENT | |
| ENABLED STUDY OF CHEMICAL SIGNALING BETWEEN BACTERIA..... | 42 |
| Abstract | 43 |
| Introduction..... | 44 |
| Materials and Methods | 48 |
| Cell Culture | 48 |
| Microfluidic Device Fabrication | 49 |
| Well-Plate Microfluidics Fabrication | 50 |
| Well-Plate Preparation..... | 51 |
| APTES Bonding Procedure | 52 |
| Assembly..... | 52 |
| Uncured PDMS Procedure | 53 |
| Imaging | 56 |
| Modeling | 56 |
| Experimental Procedure..... | 60 |
| Characterization of Chemical Gradients..... | 60 |
| Microbial Signaling Experiments | 60 |
| Results and Conclusions | 61 |
| Signal Gradient Across Chambers..... | 61 |
| Cellular Signaling | 63 |
| Oral Biofilm Signaling..... | 65 |
| Conclusion..... | 69 |
| Acknowledgements | 70 |
| Appendix..... | 71 |
| CHAPTER 4 ACCESSING MICROFLUIDICS THROUGH FEATURE- BASED DESIGN SOFTWARE FOR 3D PRINTING..... | |
| | 73 |

| | |
|--------------------------------------|-----|
| Abstract | 74 |
| Introduction..... | 75 |
| Materials and Methods | 79 |
| Feature-Based Design Software | 79 |
| Printer Setup | 79 |
| Fabrication Process | 79 |
| Droplet Generator | 82 |
| Gradient Generator | 82 |
| 3D Microfluidics..... | 83 |
| Results and Discussion | 84 |
| Design Software..... | 84 |
| Printing Process..... | 87 |
| Applications..... | 89 |
| 3D Microfluidics..... | 91 |
| Conclusions | 94 |
| Acknowledgements | 95 |
| Appendix..... | 96 |
| Supporting Information..... | 96 |
| CHAPTER 5 CONCLUSION | 100 |
| REFERENCES..... | 103 |
| APPENDIX | 118 |
| Plasma Bonding Protocol | 119 |
| PDMS to Glass | 119 |
| Materials | 119 |
| Bonding Protocol..... | 119 |
| Plasma Bonding Silicon to PDMS | 120 |
| Materials | 120 |
| Bonding Protocol..... | 120 |
| Form 2 3D Printer Operation: | 122 |

| | |
|---|-----|
| Materials | 122 |
| Operation | 122 |
| Post Processing | 122 |
| PDMS Casting in 3D Printed Molds | 124 |
| Materials | 124 |
| Mold Design Considerations | 124 |
| Mold Preparation..... | 125 |
| PDMS Molding and Bonding | 125 |
| Fluxion Device Fabrication | 126 |
| PDMS Device Fabrication and Bonding to the Bottom of a 48-Well Plate | 126 |
| Materials | 126 |
| Device Fabrication | 126 |
| Well Plate Preparation | 127 |
| Bonding PDMS to Well Plate | 127 |
| Bonding Glass Coverslip to Well Plate Device | 127 |
| <i>E. coli</i> 502/503 Signaling in Microfluidic Culture Chambers Protocol . | 129 |
| Microbe Culture..... | 129 |
| Materials | 129 |
| Day 1: Media and Device Prep | 129 |
| Media | 129 |
| Device Prep | 130 |
| Day 2: Experiment | 131 |
| Culture | 131 |
| Plate Reader | 131 |
| Device | 132 |
| Protocol for Analyzing Cell Chamber Pictures | 134 |
| Required Software | 134 |
| Bright Field Images for OD Measurements | 134 |

| | |
|---------------------------------------|-----|
| FITC Images for Signal Response | 135 |
| VITA | 136 |

LIST OF TABLES

| | |
|--|-----|
| Table 1- Parameters and their values that are incorporated into the model..... | 59 |
| Table 2 - Microwell plate layout for baseline 502 and 503 growth and fluorescence. | 132 |

LIST OF FIGURES

- Figure 1 - Nanoporous exchange device. (a) An early iteration of the exchange device with microporous membrane with an inset of the channels. (b) (1) A 500nm thick silicon dioxide layer is patterned onto a bare silicon substrate. (2) Nanopores are then patterned with e-beam lithography and etched into the oxide layer with RIE. (3) Microchannels are patterned onto the wafer using conventional photolithography. (4) Microchannels are etched through the oxide layer followed by deep RIE etching into the silicon substrate. (5) Photoresist is removed from the wafer and (6) the nanopores are subsequently etched into the substrate. (7) Pore size are reduced with PECVD and ALD oxide deposition.....25
- Figure 2 - Microporous cell culture device. (a) The device is made up of a central cell culture chamber flanked by two nutrient exchange channels. (b) (1) Lines defining the pore width are patterned into a 200nm oxide using photolithography and (2) reactive ion etching. (3) Fluidic network are then aligned and patterned over the pores in SU-8. (5) PDMS casting is then used to replicate the patterns. (6) The PDMS casting is removed and later plasma bonded to a glass slide.....30
- Figure 3 - Nanoporous membrane images. (a) Two microfluidic channels, 200 and 75 μm wide, separated by a 25 μm wide nanoporous membrane with an inset of the nanoporous membrane. (b) Nanopores prior to silicon dioxide deposition. (c) Nanopores coated with silicon dioxide to reduce pore size. .34
- Figure 4 - Diffusion of fluorescein dye under constant flow. Top image shows the flow direction through the serpentine channel and the dots represent sampling points. (a) At the inlet fluorescein is in one channel only. (b) Diffusion begins within 92 μm of the inlet, 5% of the total length. (c) After 1.2m, 66% of the channel, signals from each channel are similar.35

Figure 5 - Protein diffusion across the membrane of the nanoporous exchange device. (a) A protein gel run with effluent from the reaction and feeder channels of the device after a 24hr incubation. (b) Analysis of the gel shows that the steepest slope of the graph and the transition between restricted proteins and non-restricted proteins based on molecular weight happens occurs between 6.5kDa and 17kDa.36

Figure 6 - Culture Device (a) SEM image of the entire device with two culture chambers and two nutrient exchange channels. (b) Expanded view of the membrane separating the nutrient channel and the culture chamber. (c) The pores are 200nm deep by 1µm wide and 25µm long.38

Figure 7 - (a) Overview of the culture chamber device with a dotted outline of the expanded section in b-d. (b) 750µm beads are isolated in the culture chamber and aggregate at the pores under positive pressure. (c) Fluorescein dye loaded into the culture chamber. (d) Fluorescent signal within the support channel increases over 30min due to transport of fluorescent dye.39

Figure 8 - *E. coli* growth in the culture chamber. (a) bright field image of the culture chamber. Fluorescent images show the chamber after (b) loading, (c) 24hr of incubation, and (d) 48hr of incubation.40

Figure 9 - Microfluidic design overview. (a) Natural environments are heterogeneous and vary in confinement and inversely, how they facilitate communication. Confinement varies across environments. (b) Confinement levels across natural environments mediate nutrient availability, spatial confinement, and chemical signaling. To incorporate these aspects into our platform (b) nanoporous barriers enable communication between spatially separated cultures and are maintained by support channels.45

Figure 10 - Diagram of the fabrication process with the APTES process above and PDMS glue below.52

Figure 11 - The prepared PDMS device is shown in a. and the prepared well-plate is shown in b.53

Figure 12 - The well-plate was exposed to air plasma and submerged in a water/APTES solution to modify the surface chemistry and enable bonding between PS and PDMS. A coverslip was then plasma bonded to the PDMS surface.54

Figure 13 - The PDMS device was first bonded to a coverslip (a) and then bonded to a well-plate using uncured PDMS (b). c shows the completed device from the top and side view.....55

Figure 14 - Operation of the well-plate microfluidics can be done with either a pipet as shown (a) or a well-plate manifold pressure controller. The hydrostatic pressure within the wells is enough the cause flow through the fluidic channels (c) and fill the outlet well (b).....57

Figure 15 -Chemical gradient profiles measured using model dye and bioreporter. (a) Fluorescein dye and buffer solution flowing through the left and right support channels respectively create a signal profile in the culture chambers through diffusive transport. The fluorescent profile across support channels and culture chambers along with a diffusion-only model is shown (b). (c) Composite image of receiver cells, *E. coli* bioreporter, seeded into each culture chamber. The signal is provided from the support channel on the left. The relative fluorescence of each of the chambers in (d).....62

Figure 16 - Engineered sender and receiver signaling and AHL concentration model. (a) A quasi-steady state model built in COMSOL shows AHL concentrations in the culture chambers between 0 and 24 hrs. The relative AHL concentration between the chambers at each of the time points is shown below. (b) Receiver cells produce GFP in response to being grown in co-culture with sender cells. The graph below shows the fluorescence signal increase between mono-culture and co-culture experiments of the receiver cells.64

Figure 17 – Brightfield analysis of oral co-culture growth. The *Streptococcus gordonii* culture chamber was thresholded at pixel intensities 150, 120, and 90 to analyze chamber coverage and culture density (inset). Without chemical communication (a) the culture is more diffuse and lighter. In communication with *Fusobacterium nucleatum* (b) the *S. gordonii* forms aggregates. The total growth rate is similar in both cases (c), but the AI-2 causes aggregation of *S. gordonii* (d).....66

Figure 18 –Cell cluster sizes of *S. gordonii* increase in co-culture with *F. nucleatum* relative to mono-culture at a threshold of 150. (a) At five hours, the cluster sizes of *S. gordonii* with and without AI-2 present are similar. (b) After 24hr culture with AI-2 producing *F. nucleatum*, the average cluster size increased significantly more in the co-culture case.....68

Figure 19 - Large pore fluorescent profile. When the diffusion profile experiment is run with a large pore device, the resulting fluorescent profile has a sharp change in concentration at the center of the culture chamber. This indicates that transport is dominated by advection rather than diffusion as seen in the nanoporous device.71

Figure 20 - Signal switching the culture chamber with imbalanced support channel flow rates. (a) The relative flow rate is changed between the fluorescein and buffer support channels every 30 min. (b) shows a detailed version of one transition from the buffer support channel to the fluorescein support channel. (c) epifluorescent micrographs of the culture chamber in the beginning of a transition period at 0, 1, and 5 min.72

Figure 21 - Fabrication process. (a) The device was designed by combining fluidic parts into a custom fluidic network. (b) The design was sent to an FDM 3D printer. (c) The ABS mold is removed from the PDMS device after being cast on the heated print bed. The device was cut into individual devices, and (d) bonded to a substrate for use.....81

Figure 22 - Feature parameters and program GUI. (a) Table of features available for the design process. The GUI consists of 3 sections (b) the printer and feature parameters are given, (c) the design is represented graphically, and (d) the parameter list of all the parts in the current design for editing.86

Figure 23 - Fabrication process diagram. (a) The device was printed on a heated print bed. (b) Acetone was applied to the surface of the device to anneal the ABS surface. (c) PDMS was cast over the mold, (d) a vacuum degassed the PDMS, and (e) the heated print bed cured the device. (f) The device was removed from the bed and ABS mold and (g) bound to a glass slide.88

Figure 24 - Acetone annealing gradient generators. (a) SEM images show the surface of the ABS mold annealed by applying acetone. (b) A microfluidic gradient mixer produced using our ABS mold printing process. (c-d) Images of the device show dilution channels recombining. (c) Annealing smooths the surface for more even imaging. (d) Non-annealed device shows rough surfaces from the printing process. (e) The maximum fluorescent intensity from the individual channels prior to rejoining shows greater variability in non-annealed devices. (f) The fluorescent intensity profile in the channels after recombining show the gradient forming. Variation in the chamber height from 3D printing causes variation across the profile deviating from the expected linear gradient.90

Figure 25 - Droplet generators. (a) The T-junction device was operated with the fluorescein flow rate at 1 μ L/min and the oil at (a1) 5 μ L/min and (a2) 20 μ L/min. (b) The flow-focusing device operates with the same flow rates. (b1-2) show the oil channels pinching off a droplet from the fluorescein channel. (c) Formed droplets are highly replicable and can be controlled by altering the oil flow rate from 2 μ L/min to 20 μ L/min.92

Figure 26 - 3D microfluidics. Using 3D capabilities of the feature-based software, bridges were printed to create an overlapping design with three channels from an offset (a) and side (b) view. (d)Top view - overlapping channels

remain separate from one another. (c) Side view - the bridging structure raises off the plane of the glass slide. The expanded view shows the printing direction for the bridging structures. (e) The microfabricated structure along with an inset of the chambers with each channel independent of one another. (f) Shows 3D printed structures connecting channels and overlapping to simplify the device control.93

Figure 27 - 3D bridge printing process. The printer extrudes posts, allows them to solidify, and suspends a filament from the post to the print bed. The process is done continuously rather than layer by layer.....96

Figure 28 - Feature parameters and part list. Printer parameters for each parameter are shown in (a). Adding parts to a design populates the graphical area (b) as well as the Feature list (c). The order of parts in the list indicates the printing order.....97

Figure 29 - Device designs used. The completed designs for each device used are shown in the Matlab design environment. The droplet generator (a) and gradient generator (b) show replication of common microfluidic designs. The second droplet generator design is not shown. The coil design (c) and the network architecture (d) were used to show the 3D capabilities of the printing process.98

Figure 30 - Printer characterization from the Solidoodle printer used. The number of layers do not affect the width of the channel (a), but the number of lines can affect the height of the channel. The smallest channels were roughly 1mm wide and 200µm in height.99

Figure 31 - Fluidic connections and flow direction during priming.....130

Figure 32 - Fluidic connections and flow direction during experiment.....133

CHAPTER 1

INTRODUCTION

The field of biology focuses on understanding the complexity of living organisms and the systems that they makeup. Delving deeply into microbiology requires an understanding broader than of the organism itself, but of the environment and other organisms that influence development and reproduction. From an engineering perspective, an understanding of biology can inform design in medicine, agriculture, energy, and beyond. Studying on the cell and community scales requires high levels of precision, and the technology required to dive deeper into the driving forces of nature draws on many different fields that make microbiology highly interdisciplinary. By approaching biology from an engineering perspective, this dissertation aims to broaden the tools and technologies available to biologists to interface with biological systems.

Forms of microfluidics and microfabrication are used herein to increase the range of applications for biological systems by taking advantage of the spatial resolution afforded by microfabrication. These technologies include new design and fabrication techniques in 3D printed microfluidics using a filament deposition modeling (FDM) 3D printer to novel platforms. Microfluidic bioreactor design enhanced cell free protein synthesis (CFPS) reaction efficiency with long channel bioreactors. Multi-chamber cell culture microfluidics enabled interactions between spatially separate bacterial communities. Cell signaling between chambers was informed by signal modeling in COMSOL. Each advance adds to the set of tools available to biologists and shows applications in interfacing with biological systems across scales.

Microfluidics

The concept of microfluidics was first developed in the field of chemical analysis in the form of capillary tubes for chromatography and electrophoresis

techniques¹. Small volume analysis is still touted as a route to lower cost reactions, but the advantage goes beyond reducing the number of high-cost reagents used. With the use of small channels, the analysis techniques could accurately identify species from smaller and smaller sample sizes or in lower concentrations. This advantage of small volume analysis has since been a major driver for the field of chromatography. In cell culture, microfluidics has allowed analyses to move from bulk reactions to single cell manipulation² and single cell genomic analysis³. Micro *in vivo* like environments can be created to enhance *in vitro* culture.

Microfluidics have since evolved into its own field by developing the tools to incorporate concepts such as valving, pumping, microscopy, and on-chip sensors. Combining many of these capabilities into a single microfluidic device leads to the nickname of “lab-on-a-chip”, the idea that sample prep, culture, and analysis can be carried out on a single chip. Pneumatic valves have been developed to use multiple layers of polydimethylsiloxane (PDMS)^{4,5}. Applying a pressure differential between the channels can actuate an elastomeric membrane separating the two layers. Pneumatic valves can be used for pumping by combining multiple valves and controlling the order and frequency of pressure application⁶. On-chip valving systems have been used with automation software to control flow of samples based on analysis of images⁷. Similar to digital computers, valves can be arranged to act as gates that allow for logic circuits to be built into fluidic networks⁸⁻¹⁰.

The broad range of applications and tools can be attributed to the broad range of materials available from brittle glass to highly flexible elastomers. A range of properties and costs have developed from silicon or glass to polymers including polycarbonate (PC), cycloolefin copolymer (COC), and polymethylmethacrylate (PMMA)¹¹, but most popular has been PDMS^{12,13}. PDMS is a heat-curable elastomer that is optically clear and can be irreversibly bound to itself, glass, or silicon with the use of plasma activation that forms covalent bonds

rather than adhesives or melting that may deform small features. Many polymers are biocompatible and can be processed more easily than silicon or glass using injection molding, hot embossing, casting, or the increasingly popular 3D printing¹⁴. Developing a range of materials and fabrication processes makes adapting to new applications less complicated.

Microfluidics are further advantaged because they facilitate real-time imaging in a fluid environment. Analytical methods have developed with the field to go beyond fluorescent and bright field images into other sensor applications developed to be incorporated in microfluidic applications. For example, sensors have been incorporated into microfluidic platforms in order to measure oxygen concentration¹⁵⁻¹⁷, refractive index¹⁸, and cell properties using microwaves¹⁹. Microfluidic chemostats have been developed to incorporate various layers of information using these types of sensors^{15,20}. With tools available, it is important to focus on how these technologies can control chemical exchange and how that influences biological systems.

Cell-Free Protein Synthesis Systems

Cell-free protein synthesis systems use the components of a cell to produce a desired protein while removing limitations of maintaining engineered cells in culture. The machinery of a cell can be extracted and combined with amino acids, energy, and DNA coding for a specific protein to produce the encoded protein. That protein can be produced at higher concentrations than a cell can typically maintain and without the reagents being used to support other basic cellular functions of living cells²¹. This technology has been demonstrated to work at larger scales²², but post translational modification and membrane proteins require either specialized extracts that have lower yield than *E. coli* or extract supplementation²³. Microfluidics used in this field have primarily been used to promote the yield and functionality of proteins by controlling the physical environment of the reactions.

Typically, CFPS reactions are done in small tubes. Such systems are simple and easy to work with, but higher yields have been achieved with engineered reaction hardware²⁴. Primarily this has been done using two-chamber devices incorporating dialysis membranes to extend the duration of a reaction by replenishing depleted resources through diffusion across the membrane^{25,26}. Another approach is to use microfluidics to control when reagents are mixed with one another and fluid stresses during the reaction process²⁷. We approach the problem from this end to incorporate microfluidics and nanoscale membranes to decrease diffusion distances and allow for nutrients and amino acids to be replenished to keep a reaction going for longer^{28,29}. This can either be used to extend the useful life of a CFPS reaction on industrial scales or to make doses of medicine using fewer reagents in applications where space and weight are a limiting factor³⁰.

3D Printed Microfluidics

Microfluidic devices are primarily patterned using photolithography to replicate architectures in PDMS, silicon, or glass. This process creates designs with high resolution with features as small as 1 μ m in a range of materials that are often compatible with biological samples³¹; but the cost of the process, fabrication time, and poor scalability of throughput have been seen as limitations to distributing and commercializing microfluidic devices³². The microfluidics field has begun to look at 3D printing as a route to reduce fabrication costs and time³³⁻³⁵ while providing a route to commercialize concepts that are developed in the lab^{14,36}. 3D printed microfluidics also opens applications for DIY biology applications much like 3D printing did for prototyping at home³⁷. Filament extrusion, stereolithography, and two-photon lithography have all been used to create microfluidics³⁸. The popularity of 3D printed microfluidics has grown recently, but additive manufacturing has been used with microfluidics for some time.

During the advent of PDMS based microfluidics additive manufacturing was proposed as a method of mold fabrication^{12,13,39}. The growing availability of 3D printers enables this route but requires further refinement to the interface created between the used and the final microfluidic application. Using 3D printed molds to create microfluidics out of a castable material has been refined to be used with a number of polymers⁴⁰ most commonly in PDMS^{41,42}. Fabricated molds can have 2D structures like those from photolithography or 3D features that form channels through the cast material. The introduced software aided in the design of microfluidic devices for 3D printing similar molds along with an optimized workflow to fabricate PDMS based devices that incorporate fabrication of 3D structures⁴³. The embedded mold can then be removed mechanically⁴⁴⁻⁴⁶, or by using sugar or polymers as the mold material and dissolving them away^{47,48}. Alternatively, 3D structures can be fabricated using multiple layers of patterned PDMS similar to conventional microfabrication techniques⁴⁹. Combinations of fabrication techniques have been used to produce multi-component devices from materials with different properties⁵⁰.

Additive manufacturing has also been used to fabricate microfluidic devices with internal channels directly without the use of molds^{51,52}. This type of microfluidics has been primarily done with filament deposition modeling (FDM)⁵³ or with stereolithography⁵⁴. Devices that include valves and other control units have been developed in printable materials⁵⁵⁻⁵⁷. In order to make microfluidics more modular, Lego type microfluidic pieces allow the user to join together a fluidic device from components without going through the printing process each time^{58,59}. Direct writing can be used to take advantage of some thermoplastic solvent resistances and characteristics for organic chemistry⁶⁰. Other polymers such as PEG-DA have been used to improve optical clarity of devices⁶¹.

While many studies up to this point have been expanding the capabilities and probing the engineering space, 3D printed microfluidics have also been used in biological and chemical applications^{38,62}. An ABS plastic device was used

to grow and isolate a resistant strain of Streptococcus⁶³. Printed microfluidics have been used to identify influenza⁶⁴. Hydrogels have been used to create 3D structures for cells to incorporate into⁶⁵. The field of 3D printed microfluidics is growing to the point that substantial biological discoveries have been made with printed devices along with providing a path to commercialization for microfluidics that is simpler than PDMS based approaches. Most plastics used in 3D printing can be injection molded, providing a more straightforward road to commercialization than other techniques.

Microfluidic Cell Culture

Performing cell culture in microfluidics takes advantage of the small length scales and control of the fluid environment to improve control of nutrient flow and monitor individual cells during growth. The 3D architecture of microfluidics has been used to better replicate physiological conditions of natural environments and reduce the differences between *in vitro* and *in vivo* by constructing experiments to be run in microfabricated, silicon-based modules⁶⁶. Designs for cell culture devices range from simple stamping techniques for patterning cells^{67,68} to nanofabricated cages that facilitate 3D culture of cells and can be manipulated using magnetic fields⁶⁹. Flow through the systems can also be manipulated to provide nutrients to the culture and see cell response to shear⁷⁰. Organ-on-a-chip devices have shown that cells can perform their natural function *in vitro* by providing the architecture required to form as they would in the body^{4,32,71-74}. Each of these examples utilize the capabilities of microfluidics to better control the growth conditions for cells.

Many of the devices being developed are focused around mammalian cells and because of this, the scales required to control cells are on the order of microns rather than a few hundred nanometers for bacterial cells⁷⁵. The fundamentals of these types of culture devices can be used and adapted to bacterial culture in many cases²⁰. The resolution in these cell culture devices has

reached the scale of single cells and has been used for many different applications⁷⁶. Single-cell platforms generally use droplet microfluidics to control discrete volumes of liquid with the ability to move the droplet through screening and sorting steps⁷⁷. Droplets can be made with different materials including oleic acid⁷⁸, air⁷⁷, surfactant stabilized aqueous solutions⁷⁹, or various types of hydrogels⁸⁰. Using single-cell droplet techniques allows for stochastic combinations of cells with reactants to monitor how viability changes in a much higher throughput fashion than traditional microtiter assays⁸¹. Going further with single cell culture, platforms can be used to screen for phenotypes and study and evaluate the evolution of a species⁸². Multiplexed reactions with small volumes provide a simple way to create stochastic seeding of bacterial communities and increase the test cases being sampled^{83,84}. In addition to culture, microfluidics can be used to sample and sequence small samples using droplet microfluidics^{3,85}.

With the use of valves and built in peristaltic pumping, microfluidic chemostats were developed to grow cells by replenishing nutrients and continuously mix the reaction. At any point, lysing chemical can be added to lyse the cells for analysis⁸⁶. Systems allow for the measure of many environmental factors and control of nutrient concentrations, but other microfluidics have applications when control and measurement can be traded for a simpler fabrication process⁸⁷. Many of the 3D printed microfluidic applications are able to address this problem because adding complexity to a device does not necessarily increase the fabrication complexity⁵⁵. Within microfluidics there are a plethora of techniques available to scientists and engineers so that the focus can be returned to biology and answering questions that are out of reach for traditional techniques.

Cell Signaling

Bacterial monocultures have been used to build an understanding of how cells grow and the variability of gene expression between cells of the same species. This field is still being explored and expanded, but the normal gene expression and behaviors of cells cannot be explained fully without also looking at how communities communicate. In multicellular organisms, signaling differentiates cells that have the same genetic makeup into hundreds of unique cell types⁸⁸. Signaling within biofilms regulates gene expression between species resulting in a more robust community. What role the environment, other organisms, and the physical architecture play in gene expression of a single cell is still widely unknown. In microbiology this concept is being explored to understand how cellular communities and biofilms assemble and how they respond to and shape the local environment⁸⁹.

Cell signaling describes several cellular interactions dealing with both inter- and intracellular communication. In quorum sensing, a signal molecule is released into the environment by a cell, and at a minimum cell density the concentration of signal molecule builds up to a threshold level where it changes gene expression within the biofilm⁹⁰. Interkingdom communication has also been identified as a method of bacteria-host interaction. Acyl homoserine lactone (AHL) has been identified as a common signaling pathway among many Gram-negative bacteria as well as signaling with plants⁹¹. Carbon substrates and small molecules exuded by plants into the soil attract bacteria to the root surface. The beneficial bacteria are then able to provide growth hormones or provide improved disease resistance of the plant through their own exudate⁸⁹. The complexity of cell signaling lends itself to study with microfluidics. Microfluidics of this scale enable studying the conversation between host and community.

Microfluidic devices have aided in studying bacterial communication by providing a structured environment in which multiple species can be cultured in communication with one another, with or without physical contact. Separate

cultures that communicate across a porous barrier or membrane can be observed with light microscopy, not relying on individual markers. To measure individual species in a mixed culture, the bacteria need unique fluorescent markers or with single time point staining. These artificial markers can be problematic to engineer or affect the growth characteristics of the cells by consuming cellular resources. The microfluidic design depends on the number of species being co-cultured, the size of culture required, and types of interactions expected⁹². To increase the throughput of a co-culture system the chamber can be replicated into an array pattern with⁹³, or without⁸³ communication between chambers. Higher throughput allows for the observer of stochastic seeding and understand how that affects the trajectory of the culture.

Rather than increasing the throughput of a system, microfluidic devices can also be designed to increase the control over the physical and chemical environment. Hesselman et al. used a micro sieve to hold microbes in place as media with a chemical signal was perfused over the cells⁹⁴. This maintains a constant concentration of signal molecule in the culture. Flow in co-culture systems can remove exuded signal molecule so that the threshold level for quorum sensing is never reached^{95–98}. Some groups have tried to overcome this limitation by applying a directionality to the communication. Lovchik et al. developed a two-chamber device that perfused media over a culture and combined the conditioned media with fresh media to perfuse over the second culture chamber⁹⁹.

To better replicate the natural environment within a biofilm, groups have looked at ways to support a culture within a microfluidic device without continuous flow. Hydrogel barriers between chambers allows nutrients and signals to diffuse through the device but contains bacteria and other cells. Hydrogel barriers have been demonstrated with both bacterial¹⁰⁰, and mammalian cells⁷⁵. In addition, no flow chambers with a membrane separating the culture chamber from a reservoir has been used. Kim et al. constructed a

vertical chamber device that had individual culture chambers on one level that were fluidically connected to allow signaling¹⁰¹. This allows for diffusion of nutrients, but vertically aligned chambers can interfere with imaging techniques. Lambert et al. created microhabitat patches (MHPs) with patterned pores that contain cultures to a chamber with nutrients diffusion across the barrier from a reservoir¹⁰². Herein, aspects of these platforms were utilized to co-culture bacteria in separate chambers in a no-flow configuration with diffusive nutrient replenishment. This allows for long-term culture of bacterial species while allowing quorum sensing molecules to build up within the chamber²⁸.

Biofilms

The microbial communities and chemical signaling described here are often found when microbes are growing together in a biofilm. Biofilms are bacterial communities that have changed in morphology to attach to surfaces and protect themselves by excreting more extracellular polymeric substance (EPS) sometimes also referred to as exopolysaccharides or extracellular matrix (ECM)^{103,104}. The transition from planktonic cell to surface attachment can be signaled by nutrients, antibiotic concentration, or surface cues. This transition causes bacteria to lose their motility and produce higher levels of EPS to promote surface adhesion¹⁰⁵. Fully developed natural biofilms contain multiple species that communicate through quorum sensing to maintain population levels⁹⁰. Within biofilms the makeup is heterogeneous with fluid channels that run through the biofilm and stratification of bacterial species based on their environmental preferences as well as nutrient and oxygen gradients throughout the biofilm¹⁰⁶. The surface of a biofilm is often uneven which increases the surface area with the bulk fluid surrounding the biofilm to better take up nutrients¹⁰⁷. The spatial structure makes biofilms inherently difficult to study using conventional techniques, but microfluidics is showing promise as a method for

culturing biofilms over extended periods of time to show the full life cycle of a biofilm-producing community¹⁰⁸.

Microfluidic platforms have been developed to study different aspects of biofilm formation, growth, communication, and dispersion. Drescher et al. showed that tortuous channels with high shear rates cause biofilm forming bacteria to buildup streamers until the channel clogs¹⁰⁹. Others have looked into different influences that could promote or cause bacteria to form biofilms^{110,111}. Studies have looked at how channel flow characteristics are influenced by a growing biofilm¹¹². Signaling either between species or surface and environmental cues cause changes in gene expression to moderate the cells within the biofilm¹¹³. Many of these experiments do a good job of testing different criteria in the complex problem space, but microfluidics also offers imaging techniques and approaches that allow for the imaging of biofilms over extended periods of time to try to better understand to subtleties of biofilm structure with simultaneous observations and analysis¹¹⁴.

Oral Microbiome

A biofilm producing community of interest is the oral microbiome. The community has been identified to contain around 700 species¹¹⁵ with close to two thirds of those species having been isolated in culture¹¹⁶. Cultivation and study of these communities is complicated by the niches of the oral environment. Mucus suspended microbes can grow in the fluctuating environment while subgingival microbes are often anaerobic and rely on intermediate metabolites provided by the consortia present¹¹⁷. Despite the knowledge surrounding this environment, the exact mechanisms and species involved when a healthy microbiome shifts to diseased is not clearly known. Genetic sequencing can point towards species that are identified in infected microbiomes such as the 'red complex' pathogens *Porphyromonas gingivalis*, *Tannerella forsythia* and *Treponema denticola*, but the total number of species that are found in diseased samples is close to 500¹¹⁸.

to understand which of these bacteria contribute to disease is determined by the interactions of the bacterial community and this relies on further cultivation and screening of bacterial species.

Screening interactions between oral microbes is currently done with both liquid cultures and plating techniques. The culture of *Tannerella* sp. HOT-286 was recently done using plating techniques that required sampling from a sample of subgingival plaque and iterating through sampling from plates after cultivation until a microbe of interest could be isolated. The isolate was then grown with a helper strain of bacteria on the same plate or through a nanoporous membrane to achieve growth¹¹⁹. Siderophores have also been shown to promote the growth of community dependent bacterial strains¹²⁰. Quorum sensing molecule autoinducer-2 (AI-2) has been identified as a growth promoting or inhibiting factor based on species. Produced by *Fusobacterium nucleatum* sp. *nucleatum*, AI-2 was screened with *Streptococcus oralis* and *Streptococcus gordonii* and showed increased biofilm production in *S. gordonii* and decreased production in *S. oralis*^{121–123}. Microfluidic techniques have been tested as methods to screen oral microbes while being able to monitor the cells with microscopy and increase the throughput to improve success rates.

Alternative methods using microfluidics have started to be used to better replicate the 3D environment of the mouth and study quorum sensing within oral biofilms⁶⁶. The physical aspects of surface adhesion and cell-cell interaction distance was covered by Kolenbrander et al¹²⁴. The roll and concentration of AI2 in oral biofilms and how it relates to periodontitis shows how the heterogeneity of a biofilm may lead to accumulation of signal molecules and depletion of oxygen when heavy EPS producers are present and stimulated. Lam et al. has incorporated an oxygen regulating microfluidic culture device that allows for control of the oxygen levels present in the biofilm to monitor the effects on growth^{16,125}. Commercial applications like the Bioflux™ well-plate microfluidics platform have been used to screen oral biofilms for antimicrobial resistance¹²⁶.

Microfluidics used in oral microbiome studies so far do not take advantage of the advancements seen in microfluidic culture devices. The co-culture platform built on microfluidic cell culture techniques to grow spatially separate members of the oral microbiome and study chemical interactions.

Modeling Bacterial Growth and Signaling

The results of interactions between cells can be seen with experimental techniques, but the nutrient and signal concentrations that drive the reactions can only be implied based on observable changes in phenotype structure. Accurate computer modeling of the environment gives a clearer representation of what drives the system from fluid flow and diffusion to the consumption of substrates and cell growth. Using modeling in tandem with experimental techniques provides a more complete understanding. The experimental results act to validate the model and the validated model allows for rapidly testing a broader range of parameters. Modeling is used with our microfluidic chambers to understand the impact of nanoporous membranes on the nutrient and signal levels within the microfluidic culture chamber. With low porosity and negligible flow, the microfluidic device is often limited by nutrient availability rather than the maximal growth rate of the cell. Horn et al. have written a review that covers the techniques commonly used to model biofilms and the state of the art in this field¹²⁷.

Biofilm modeling is done with multiple frameworks. Agent-based modeling looks at cells or groups of cells as the smallest unit. Interactions with the environment are calculated based on environment at the surface of the cell. With this approach, the structure of a biofilm can be altered by the environment. High levels of nutrients resulted in a uniform growth of the biofilm while nutrient-poor conditions resulted in separation between species within the biofilm and a structural change to high surface area configuration that promotes nutrient contact¹²⁸. Agent-based modeling has also been implemented in cancer research

to study how vascularization in tissue effects growth and radiation response of both cancer cells and normal cells¹²⁹. Both examples show the ability of the agent-based method to model the spatial structure of cellular networks.

PDE-based, finite element models have been developed that incorporate growth and quorum sensing of a bacterial community with advection and diffusion¹³⁰. Their model describes a fluidic channel with creeping flow so that the signal being produced by the culture can accumulate rather than being washed away by media perfusion. Movement of species through the biofilm and media are modeled with a variable diffusion coefficient. Other groups have gathered experimental data to verify their model¹³¹. Limited diffusion through the biofilm explains how bacterial communities can achieve quorum sensing even under flow and how biofilms can be highly resistant to antimicrobial treatments.

Others have used a hybrid type approach modeling cells in a chamber as individuals, but with this structured approach the growth of the biofilm is not included in the model, but rather the consumption rates at a few select time points¹³². By building a mathematical model of the culture chambers used, relative concentration of signal molecules can be estimated. The experimental results are used to build the model while the model will provide information about the relative concentration of signal molecules throughout the platform.

Research Aims

The goal of this dissertation is to open new paths to interfacing biological systems through microfluidics. There are three distinct projects that work together to complete this objective. The first project leverages the scale and resource efficiency of microfluidics to maximize the yield of CFPS reactions by introducing a new bioreactor design. In CFPS systems, increasing the yield of a reaction or decreasing the footprint of a production system can open new opportunities in point-of-care medicine, personalized medicine, or overcoming lack of infrastructure in developing areas. A compact serpentine channel device

was created to increase the aspect ratio and decrease diffusion distances while maintaining a useful volume for the reactor. This setup can be run continuously to further increase the potential output. A patterned nanoporous membrane was added to create a dual channel reactor with molecular transport between the reaction channel and the support channel and extend the reaction time. The two devices show how simple microfluidics can be used to increase the productivity in the single channel design and show how advanced fabrication techniques can maximize reaction yields.

The second project introduces novel software and a microfluidic fabrication process to expand the accessibility of microfluidic by eliminating the need for cleanroom facilities using 3D printing technology. The design software was built around microfluidics and uses common microfluidic pieces to design new devices. The program replaces slicer software for the 3D printer and gives the user direct control over the printing process to correct printing mistakes without changing the final design. Along with a streamlined workflow for printing and molding a PDMS device, the process is meant to simplify the process and increase the exposure of microfluidics for potential applications in education and prototyping and production of microfluidics for labs with limited access to cleanroom facilities.

Project three expands cell culture platforms to address engineering problems studying microbial communities. Cell culture and communication approaches employed preserve aspects of the heterogeneity of the natural world while providing control over the environment while allowing for analysis. Patterned membranes between culture chambers confine microbes while allowing diffusion of nutrients and signal molecules between the communities. Characterization with engineered “sender” and “receiver” *E. coli* showed signaling across the membrane using AHL signal pathway expressing GFP in the receiver cells. The production and diffusion of AHL within the platform was calculated in a model to learn about signal buildup within the chambers.

Signaling between members of the oral microbiome was studied using the platform. *S. gordonii* was cultured with and without *F. nucleatum* to study the effects of an AI-2 producing oral microbe on biofilm production in an early colonizer.

CHAPTER 2
FABRICATION OF NANOPOROUS MEMBRANES FOR TUNING
MICROBIAL INTERACTIONS AND BIOCHEMICAL REACTIONS

A version of this chapter was originally published by Peter G. Shankles, Andrea C. Timm, Mitch J. Doktycz, and Scott T. Retterer:

Peter G. Shankles, Andrea C. Timm, Mitch J. Doktycz, and Scott T. Retterer. "Fabrication of Nanoporous Membranes for Tuning Microbial Interactions and Biochemical Reactions." *Journal of Vacuum Science & Technology B* 33(6) (2015): 06FM03.

Cell-free protein synthesis (CFPS) is an exciting field with the potential to change how we produce high value, potent, or complicated products. This paper addresses how the structure and design of the bioreactor plays into the overall production of product. To control transport of molecules, advanced fabrication techniques were implemented to address the biology on a molecular level. The spatial confinement of CFPS components enables extended reactions and increases the yield without consuming more high cost reagents which plays into the economics of the field.

This paper deals heavily with the fabrication of the multiscale platform that facilitates exchange across short length scales and transport of small molecules across nanofluidic barriers. We published two other papers on the production of sfGFP in the fabricated reactors and comparing these results to a commercially available macroscale exchange reactor^{29,30}. One article characterized continuous flow production of protein in a serpentine channel, and the other compared a bulk CFPS reaction, a single channel device, a commercial exchange reactor, and a dual channel exchange reactor.

Large cultures of genetically engineered bacteria or yeast are typically used for synthesis of therapeutics such as insulin run in batches perhaps with feeding steps during the process. This works well for producing large amounts of pharmaceuticals such as insulin, but small volume applications for personalized medicine and point-of-care applications are limited in the cost to develop engineered organisms. CFPS systems are ideal for these small volumes, and the

reaction hardware can be tuned to the specific application and volume required with the flexibility of microfluidics. Continuous flow production of sfGFP was done in a single channel reactor with three inlets. The components of the CFPS reaction were split into nonreacting components of small reagents, DNA, and cell extract. The small channel dimensions lead to efficient mixing of the components by diffusion within the channel. Effective mixing of the reagents within the device lead to 1.39 ± 0.27 higher yield than a bulk reaction²⁹. This application shows the effectiveness of microfluidics for CFPS reactions but incorporating nanoscale exchange has also been used to further improve reaction yields.

Further work incorporated a nanoporous membrane into the serpentine reactor to create a dual channel design. The aspects of a commercial exchange reactor were established in a microfluidic form to combine the advantages of microfluidics shown in the serpentine device and the improved yields shown in exchange devices. In this setup, the CFPS components were loaded into one channel of the device and an osmotically balanced reagent mix was loaded into the other channel. The nanoporous barrier separating the chambers had gap sizes of 10-20nm to confine DNA and large molecules to the reaction channels of the platform. With this setup, the exchange media ratio was varied from <1:1 to 10:1 in our device and held constant at the recommended 14:1 in the commercial reactor. The total protein produced was comparable in our dual channel device and the commercial exchange reactor at a ratio of 7.5 in our device and 14 in the other. At a ratio of 10, dual chamber device was able to produce more protein in 8hr than the commercial reactor did in 24hr. The most efficient use of reagents in general was at the lowest ratio of <1. These results show that depending on the application and restraints, reactors and reactions can be tuned to maximize yield or efficiency based on need.

These results show the importance of device design on something generally seen as independent of geometry like reaction kinetics of a CFPS reaction. Advances will continue in the biochemical side of CFPS to improve yield

and expand the types of proteins that can be produced but Improving bioreactors can lead to more tailored commercial applications. The characterization of the dual chamber design shows the importance of the biological interface created by the processes described below.

Abstract

New strategies for combining conventional photo- and soft- lithographic techniques with high-resolution patterning and etching strategies are needed in order to produce multi-scale fluidic platforms that address the full range of functional scales seen in complex biological and chemical systems. The smallest resolution required for an application often dictates the fabrication method used. Micromachining and micro-powder blasting yield higher throughput, but lack the resolution needed to fully address biological and chemical systems at the cellular and molecular scales. In contrast, techniques such as electron beam lithography or nanoimprinting allow nanoscale resolution but are traditionally considered costly and slow. Other techniques such as photolithography or soft lithography have characteristics between these extremes. Combining these techniques to fabricate multi-scale or hybrid fluidics allows fundamental biological and chemical questions to be answered. In this study, a combination of photolithography and electron beam lithography are used to produce two multi-scale fluidic devices that incorporate porous membranes into complex fluidic networks in order to control the flow of energy, information, and materials in chemical form. In the first device, materials and energy were used to support chemical reactions. A nanoporous membrane fabricated with e-beam lithography separates two parallel, serpentine channels. Photolithography was used to pattern microfluidic channels around the membrane. The pores were written at 150nm and reduced in size with silicon dioxide deposition from plasma enhanced chemical vapor deposition (PECVD) and atomic layer deposition (ALD). Using this method, the molecular weight cutoff (MWCO) of the membrane can be adapted to the system

of interest. In the second approach, photolithography was used to fabricate 200nm thin pores. The pores confined microbes and allowed energy replenishment from a media perfusion channel. The same device can be used for study of intercellular communication via the secretion and uptake of signal molecules. Pore size was tested with 750nm fluorescent polystyrene beads and fluorescein dye. The 200nm PDMS pores were shown to be robust enough to hold 750nm beads while under pressure but allow fluorescein to diffuse across the barrier. Further testing showed that extended culture of bacteria within the chambers was possible. These two examples show how lithographically defined porous membranes can be adapted to two unique situations and used to tune the flow of chemical energy, materials, and information within a microfluidic network.

Introduction

Water filtration can be traced back to 12th century Greece when water would be passed through a cloth sack to purify it. While the efficiency of commercial filters has improved, the basic concept of using an interwoven sheet of fibers as a filter membrane is a common method of filtration to this day. The random alignment of fibers creates tortuous paths through the membrane, limiting what molecules and particles can pass through. Studying this type of filter, Holdich et al.¹³³ found that although spaces between some fibers were greater than 50 μ m, the membrane blocked 99% of particles larger than 3 μ m. The packing of the fibers as well as fouling of the filter controlled the effective pore size. Large particulates filled the void spaces of the filter and caused a reduction in the effective pore size. The effective pore sizes in this case ranged from 2.5 μ m to 5 μ m, 10% of the actual pore size¹³³. Beginning with track etching of cellulose nitrate membranes for filtration studies¹³⁴, micro and nanofabrication techniques have been used to fabricate porous membranes with well controlled permeability¹³⁵. Microfabrication allows improved control of pore size as well as

pore density. These techniques can be categorized as “bottom up” approaches or “top down” approaches.

Bottom up approaches rely upon self-assembling structures to create pores that restrict transport by creating tortuous paths through the membrane. Such membranes have been made using self-assembled nanowires¹³⁶, colloidal self-assemblies¹³⁷, amorphous silicon (a-Si) to porous nanocrystalline silicon (pnc_Si) crystallization¹³⁸, and vertically aligned carbon nanofibers^{139–142}. These membranes still rely on restricting transport with implementation of tortuous paths that molecules must take to pass through the membrane. The distribution of effective pore size depends on the thickness of the membrane. Required membrane thickness is an important property to take into account when incorporating these types of membranes into microfluidic devices. Top-down approaches are able to more tightly control the distribution and size of pores within a nano- or microporous membrane. This has been accomplished using lithographic steps to produce a predefined pattern on a membrane using track etching^{134,143,144} sacrificial oxide layers¹⁴⁵, focused ion beam (FIB) milling¹⁴⁶, reactive ion etching (RIE)¹³⁵, and e-beam lithography¹⁴⁷. Top down approaches produce membranes that have a pore size dependent upon the pore design rather than on fouling of the membrane to create tortuous paths.

Top down fabricated filters have a range of biological applications centered around systems that are regulated by semi-permeable membranes by limiting species transport based on size. Accurately replicating these systems requires the spatial control that is afforded by the use of microfluidics. Membranes have been incorporated into microfluidics by using slits etched into silicon membranes^{147–151}. These devices have been shown to provide control over the transport of materials and energy to support cell-free protein synthesis (CFPS) reactions^{147,151}. Other applications addressed with embedded membrane in microfluidic architectures include dialysis¹⁵², cell-free exchange reactors¹⁵⁰, and even for experimental DNA sequencing techniques¹⁵³.

In addition to molecular transport control, microfluidics have been used in a number of ways to manipulate, grow, and analyze cells by leveraging their fluid flow control and microstructure environmental advantages⁷². Many microfluidic cell culture devices contain membranes to provide nutrients to the cells or control movement of cells through the device^{4,87,154–158}. Microhabitat patches developed by the Austin group were used to limit transport of nutrient in order to study bacterial competition^{155,159–161}. However, a majority of current microfluidic cell culture chambers either deal with larger mammalian cells rather than smaller bacterial cells⁸⁷, or are fabricated in silicon^{155,157} which are slower to fabricate and limit the use of transmitted light microscopy compared to PDMS devices.

In the first approach, e-beam lithography was used to define pores that were etched into a silicon substrate and monolithically integrated into a microfluidic network using RIE. Oxide deposition in the pores was used to tune the MWCO, creating a well-defined nanoporous membrane separating microfluidic channels. These pores were able to tune the exchange of energy and materials to support biochemical reactions. The second approach consisted of a square cell culture chamber and two nutrient channels separated by a microporous membrane. Flat, 200nm deep pores isolated microbial cells in a culture chamber, but allowed for transport of nutrients and chemical signals. These larger pores were fabricated in PDMS to facilitate imaging via live-cell microscopy. GFP expressing *Escherichia coli* cells were grown in the culture chambers with nutrient transport to demonstrate operation. These two applications for incorporation of top down fabricated porous membranes show how fabrication techniques can be adapted to control the transport of energy, materials, and information within a microfluidic network in a manner that is tailored to the scale of the biological system of interest.

Experimental

Two multi-scale fluidic devices were fabricated and tested. The first device incorporated a membrane with nanoscale pores to control transport of chemical species between microfluidic channels, retaining larger molecular weight (MW) molecules and allowing exchange of small MW molecules. Top-down fabrication techniques allowed for tuning of the pore size to control MWCO of the membrane and pore density to influence total exchange. The MWCO of the membrane was tuned by controlled coating of pores to adjust pore size. The second multi-scale device incorporated a microporous membrane designed to confine cell colonies in individual chambers while allowing communication and nutrient transfer. Both devices used porous membranes to control the flow of energy, materials, and information, selectively renewing chemical species critical to the long-term function of the biochemical and biological systems of interest.

Nanoporous Exchange Device

The nanoporous exchange device consists of two parallel, serpentine channels separated by nanopores. A microporous device was first fabricated using photolithography shown in Figure 1 (a). Fluidic devices with nanoporous membranes, having the same design but narrower pores, were created using a combination of e-beam lithography and photolithography to define a silicon dioxide etch mask. Anisotropic silicon etching was used to pattern the microchannel network, and then both the network and nanopores were etched with the same process. The pore size was decreased via silicon dioxide deposition using PECVD and ALD to tune the MWCO. The device was designed with a 200 μm wide primary channel and a 75 μm wide secondary channel separated by a 25 μm thick nanoporous membrane. The pores were 8.5 μm deep while the channels are 60 μm deep.

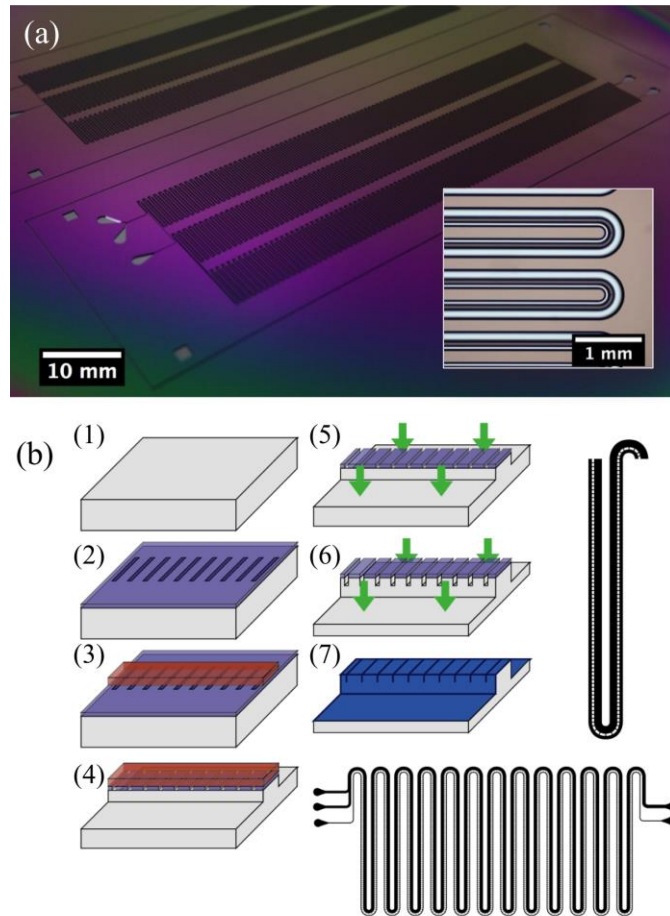


Figure 1 - Nanoporous exchange device. (a) An early iteration of the exchange device with microporous membrane with an inset of the channels. (b) (1) A 500nm thick silicon dioxide layer is patterned onto a bare silicon substrate. (2) Nanopores are then patterned with e-beam lithography and etched into the oxide layer with RIE. (3) Microchannels are patterned onto the wafer using conventional photolithography. (4) Microchannels are etched through the oxide layer followed by deep RIE etching into the silicon substrate. (5) Photoresist is removed from the wafer and (6) the nanopores are subsequently etched into the substrate. (7) Pore size are reduced with PECVD and ALD oxide deposition.

Electron Beam Lithography

Pore features were written directly to each device using e-beam lithography. 500nm of silicon dioxide was deposited onto a bare 4-inch silicon wafer with a thermal oxide process (Temperature: 1000°C, O₂: 3000sccm, H₂O: 3ml/min, Pressure: 1atm, Time: 80 min). ZEP520A (ZEON, Tokyo, Japan) e-beam resist was spin-coated onto the wafer at 1000rpm for 45sec. Pre-exposure bake was done on a hot plate at 180°C for 45sec. The nano-pore pattern was written with a JEOL JBX-9300FS Electron Beam Lithography system (Peabody, MA) (Shot Size: 4nm, Voltage: 100kV, Current: 2nA) and developed with Xylenes for 30 sec. Samples were rinsed with IPA and dried with nitrogen. The exposed oxide was etched with an Oxford Instruments Plasmalab System 100 Reactive Ion Etcher (Abington, Oxfordshire, UK) (RF: 200W, ICP: 2000W, C₄F₈: 45sccm, O₂: 2sccm, pressure: 7mTorr, temperature: 15°C) at a rate of approximately 300nm/ min.

Microchannels

A photolithography mask with the fluidic network was written on a Heidelberg DWL 66 (Heidelberg, Germany) with a 20mm write head. The Si wafer with etched pores was coated with MicroPrime P20 adhesion promoter (Shin-Etsu Microsci, Phoenix, AZ) at 3000 rpm for 45 seconds. Rohm and Haas Electronic Materials Megaposit SPR 220-4.5 Positive Photoresist (Malborough, MA) was spin-coated onto the wafer at 3000 rpm for 45 seconds. The wafer was baked on a hot plate at 90°C for 90 sec. After cooling, the wafer and microchannel mask were aligned with a Neutronix Inc NxQ 7500 mask aligner (Morgan Hill, CA) with a dose of 165mJ/cm². The device was held at room temperature for 30 min to ensure no bubbling of the resist occurred during subsequent baking. Post exposure bake was done at 115°C for 90 seconds. The wafer was then developed in Microposit MF CD-26 developer (Malborough, MA) until clear.

Reactive Ion Etching of Fluidic Network and Membrane

SF₆ 1sccm, pressure 20mTorr, time 3sec, temperature 15°C. Etching: RF 7W, ICP 1750W, C₄F₈ 2sccm, SF₆ 120sccm, pressure 20mTorr, time 10sec, temperature 15°C). The wafer was then sonicated in an acetone bath for 5 minutes to remove the resist. A PVA TePla IonWave10 oxygen plasma (RF 6000W, O₂ 250sccm, Ar 25sccm, pressure 200mTorr, time 20 min) was used to remove any remaining resist. An additional 30 loops of the same Bosch etching process etched the pores and channel simultaneously to final depth of 13µm and 52µm respectively. The ratio between these two etch steps determined the ratio of pore depth to total channel height.

Silicon Dioxide Coating of Nanopores

The etched silicon nanopores were coated with an oxide layer in order to reduce the gap size in a controllable way. Silicon dioxide was deposited with an Oxford Instruments Plasmalab System 100 Plasma Enhanced Chemical Vapor Deposition (PECVD) (Abington, Oxfordshire, UK) tool (RF 20W, 5%SiH₄/Ar 85sccm, N₂O 157sccm, pressure 1000mTorr, time 14 min, temperature 350°C). The non-conformal deposition decreased the amount of scalloping left by the Bosch process. Oxford Instruments FlexAL Atomic Layer Deposition (ALD) System (Plasma: RF 400W, O₂ 60sccm, pressure 15mTorr, time 2sec, temperature 150°C Precursor: Bis(diethylamino)silane (BDEAS) time 0.7sec) with a deposition rate of 3Å for 27 cycles was used to further decrease the pore size by 8nm and tune the molecular weight cut off (MWCO) of the nanomembrane. After the bioreactor fabrication was complete, the devices were sealed by air plasma bonding with a Harrick Plasma PDC-001 air plasma cleaner (Ithaca, NY) a 5mm thick polydimethylsiloxane (PDMS) cover over the device. Inlets and outlets were punched using a Ted Pella 0.75mm biopsy punch (Redding, CA) and removed with tweezers.

Device Testing

Testing of the nanopores was done with fluorescein dye. Quantifying the MWCO of the membrane was done by loading one channel of the device with a protein ladder and the other with a buffer solution. Incubation overnight allowed proteins to diffuse across the membrane. Fluorescein dye (Sigma-Aldrich, St. Louis, MO) was suspended in phosphate buffered saline (PBS) to promote dissolution at a concentration of 10 μ M. The dye was loaded into one channel while PBS was loaded into the other. The channels were set to flow rates of 15 μ l/hr and 5.6 μ l/hr to maintain a constant velocity in the two differently sized channels. After coming to equilibrium, pictures were taken of the device with an Olympus IX51 microscope (Shinjuku, Tokyo) at loops 1, 20, and 150 of the device, which corresponded to 0, 5, and 66% of the total channel length to show diffusion across the membrane. Images were taken in epi-fluorescence using a Chroma 41001FITC (Bellows Falls, VT) filter cube (480nm excitation band pass filter with a 40nm band width and 535nm emission band pass filter with a 50nm band width). To determine the molecular weight cutoff of the nanoporous membrane, an Ultra-low Range Molecular Weight Marker ladder (Sigma-Aldrich, St. Louis, MO) with molecular weights of 1.060, 6.500, 14.200, 17.000, and 26.600kDa was used. One channel of the device was filled with the protein ladder, and the other with the accompanying sample buffer. Devices were covered in water-soaked wipes and placed in 30°C incubator overnight. Flushing each channel with water, samples were collected from the device. Samples were run on 16.5% Mini-PROTEAN Tris-Tricine Gel (BioRad, Hercules, CA) using the BioRad Mini-PROTEAN Tetra Cell (Hercules, CA) electrophoresis system. The gel was fixed in 4% paraformaldehyde diluted in PBS, rinsed in water, and stained with SimplyBlue SafeStain (Life Technologies, Carlsbad, CA). Gel image was analyzed for relative protein content at each molecular weight using gel analysis tool in Fiji.

Cell Culture Device

Devices to be used in cell culture studies were replicated from multi-scale masters. Two photolithography steps were used to assemble masters starting with a 200nm silicon dioxide layer used to form 1 μ m wide micropores. The fluidic network was formed over the pores in a second photolithography step. The device consisted of a 1mm square culture chamber flanked by two 100 μ m wide nutrient channels to supply nutrients to the cells. Pores 200nm thick were used to mimic the function of a sterile biological filter. The thickness can be altered based on the type of cells used by adjusting the thermal oxidation process. SU-8 photoresist was then used to form the culture chamber area over the pores. These are each separated by a 25 μ m membrane with pores at a pitch of 25 μ m. Figure 2 shows a micrograph of the culture device along with the steps involved in the fabrication process.

Photolithography

For PDMS reactor masters, 200nm of oxide were deposited onto a silicon wafer with a thermal oxide process (Temperature: 1000°C, O₂: 3000sccm, H₂O: 3mL/min, Pressure: 1atm, Time: 18 min). MicroPrime P20 adhesion promoter (Shin-Etsu Microsci, Phoenix, AZ) was spin-coated onto a wafer at 3000rpm for 45sec. JSR Micro Microphotoresist (negative) NFR 016D2-55cP (Sunnyvale, CA) was spin-coated on the P20 at 3000rpm for 45sec. The wafer was baked on a hot plate at 90°C for 90sec. After cooling, the pores and microchannel mask were aligned with a Neutronix Inc NxQ 7500 mask aligner (Morgan Hill, CA) with a dose of 36mJ/cm², and baked at 115°C for 90sec. The wafer was developed using Microposit MF CD-26 developer (Malborough, MA). The patterned wafers were then etched with an Oxford Instruments Plasmalab System 100 Reactive Ion Etcher (Abington, Oxfordshire, UK) with the same oxide etch parameters as used with the nanoporous device at a rate of 300nm/min through the oxide leaving 1 μ m pores. Devices were sonicated in acetone to remove the photoresist.

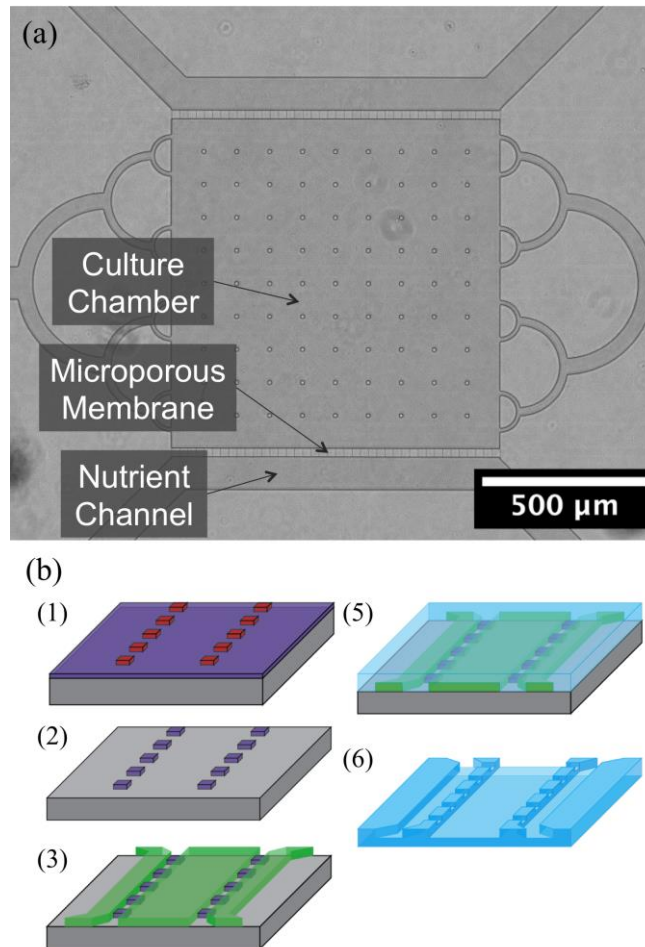


Figure 2 - Microporous cell culture device. (a) The device is made up of a central cell culture chamber flanked by two nutrient exchange channels. (b) (1) Lines defining the pore width are patterned into a 200nm oxide using photolithography and (2) reactive ion etching. (3) Fluidic network are then aligned and patterned over the pores in SU-8. (5) PDMS casting is then used to replicate the patterns. (6) The PDMS casting is removed and later plasma bonded to a glass slide.

Micro-Chem SU-8 2010 positive photoresist (Newton, MA) was spin-coated on the wafer at 3000rpm for 45 sec and baked at 90°C for 2.5 min. An exposure dose of 132mJ/cm² was used on a Neutronix Inc NxQ 7500 mask aligner (Morgan Hill, CA). Post exposure bake was done at 95°C for 3.5 min. The wafer was developed with the spray-puddle method with SU-8 developer (Micro Chem, Newton, MA) until clear. The wafer was then baked at 250°C for 5 min to promote adhesion. The master wafer was plasma cleaned with a Harrick Plasma PDC-001 air plasma cleaner (Ithaca, NY) and silanized with trichloro(1H,1H,2H,2H-perfluorooctyl) silane (Sigma-Aldrich, St. Louis, MO) by storing in a closed glass container with 20 µl of silane, at 85°C for 2 hr.

PDMS Casting and Device Bonding

Sylgard 184 PDMS from Dow Corning (Midland, MI) prepolymer and crosslinker components were used in a 5:1 prepolymer to crosslinker ratio to form devices. Doubling the amount of crosslinker from the base 10:1 ratio stiffens the resulting PDMS. This increases the yield for the nanopores, which can otherwise flex and bond to the glass, resulting in reduced or no transport across the membrane. The PDMS mixture was poured over the silanized master, degassed, and baked at 75°C for 1 hr. The devices were removed from the master with a razor blade and placed in a dish with the features facing up. The molded devices were baked at 75°C for an additional 48 hr to fully cure the elastomer and evaporate any remaining solvents in the PDMS. This further stiffens the PDMS, improving the number of open pores in the device.

Replication of the pores was consistent when using these techniques. Inlets and outlets were punched with a Ted Pella 0.75mm biopsy punch (Redding, CA). The device and a glass slide were plasma cleaned using a Harrick Plasma PDC-001 air plasma cleaner (Ithaca, NY) for 2 min, and brought into contact to form a permanent bond. The devices were baked at 75°C for 15 min to anneal the polymer and improve bonding. Devices were used the same day; otherwise pores were liable to collapse after a couple of days.

Device Testing and Cell Culture

Fluorescent species that were larger (fluorescent microspheres) and smaller (fluorescein dye) than the pore size were loaded into the culture chamber and monitored over a 30 min period. 750nm Fluoresbrite yellow green carboxylate microspheres (PolyScience, Niles, IL) in DI water, and fluorescein dye (Sigma-Aldrich, St. Louis, MO) in PBS were loaded into separate devices with their respective solvents loaded into the support channels using a New Era NE-1800 syringe pump (Farmingdale, NY) Fluorescence images of each device were taken on an Olympus IX70 (Shinjuku, Tokyo) inverted epi-fluorescence microscope. Image overlay was performed in Image J.

One Shot TOP10 chemically competent *E. coli* cells (Invitrogen, Waltham, MA) were transformed with a pUC19 vector containing eGFP and ampicillin resistance. The constitutively expressed eGFP was used to quantify cell growth under continuous perfusion of media. LB broth made with 10g/L tryptone, 5g/L yeast extract, and 10g/L sodium chloride (Sigma-Aldrich, St. Louis, MO) with 100µg/mL ampicillin (Sigma-Aldrich, St. Louis, MO) was inoculated with cell culture from an LB agar plate (LB broth with 15g/L agar (Fisher, Pittsburgh, PA)) with a similar concentration of ampicillin. The liquid culture was incubated at 37°C in a shaker incubator for 2 hr. The culture was then spun down in a centrifuge at 2500rpm for 5 min. The media was poured off and replaced with M9 minimal media broth (Amresco, Solon, OH) in order to minimize autofluorescence when imaging. Cells were then loaded into the culture chamber and blank M9 media was loaded into the nutrient channels via syringes. Media was perfused through the nutrient channels with a Harvard Apparatus Pump II Elite (Holliston, MA) at a rate of 5µL/hr over 72 hr. Fluorescent images were taken every hour with a Nikon Eclipse Ti-U inverted epifluorescent microscope (Tokyo, Japan). Image analysis was done with Image J.

Results and Discussion

Nanoporous Exchange Device

Verification of the fabrication process described in the experimental section began with SEM images of the device. The tested device had two channels each 52 μm deep and 1.8m long, the channels were 75 μm or 200 μm wide. The pore design, patterned by e-beam lithography, was 150nm wide. Pore width, measured by SEM, was 180nm at the oxide mask and decreased to a point. The depth of the pores was between 12.9 and 14.2nm. Figure 3 shows SEM micrographs of the completed device prior to closing the pores with silicon dioxide and after PECVD treatment.

Transport of fluorescein dye across the membrane was measured to verify the operation of the membrane. Fluorescent images were taken after the device had reached a steady state. Images were taken at the inlet of the device, after 10 loops, and after 150 loops or 5% and 66% of the serpentine channel. Figure 4 shows a diagram of the device with flow direction through the device and where on the device images were taken. At the inlet, fluorescein is in the large channel only. Fluorescein begins to diffuse across the membrane within 5% of the channel and the two channels are at a similar concentration at 66% of the channel.

Diffusion of the components of a small molecular weight protein ladder through the membrane was measured to allow estimation of the MWCO of the nanoporous membrane. Samples collected from each channel were run on a protein gel, which showed that the ratios of feeder to reactor concentrations for the 1.06 kDa and 6.5 kDa ladder components were higher in the feeder channel than with the larger 14.2 kDa, 17 kDa, and 26.6 kDa proteins. The slope of the graph is steepest, indicating a rapid change in permeability, between 6.5kDa and 17kDa. This range is the transition between restricted and unrestricted proteins due to size. The graph in Figure 5 shows the fraction of each of the proteins

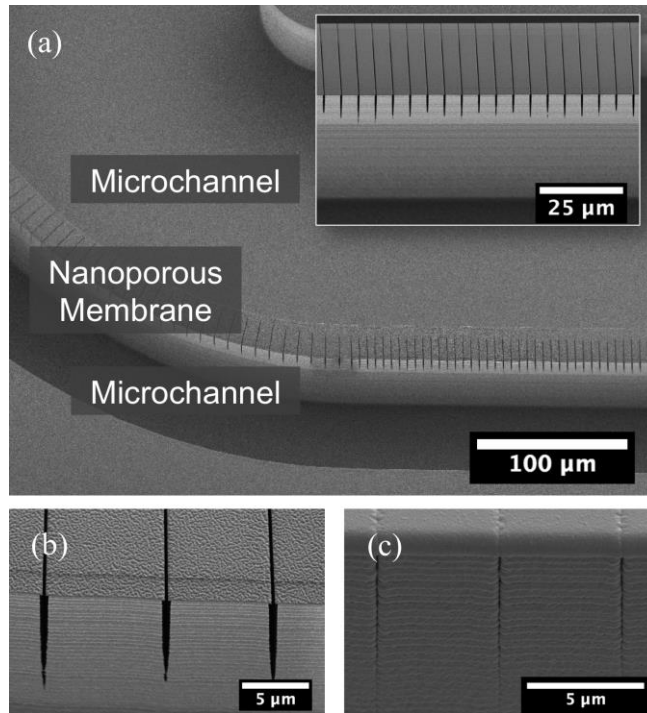


Figure 3 - Nanoporous membrane images. (a) Two microfluidic channels, 200 and 75μm wide, separated by a 25μm wide nanoporous membrane with an inset of the nanoporous membrane. (b) Nanopores prior to silicon dioxide deposition. (c) Nanopores coated with silicon dioxide to reduce pore size.

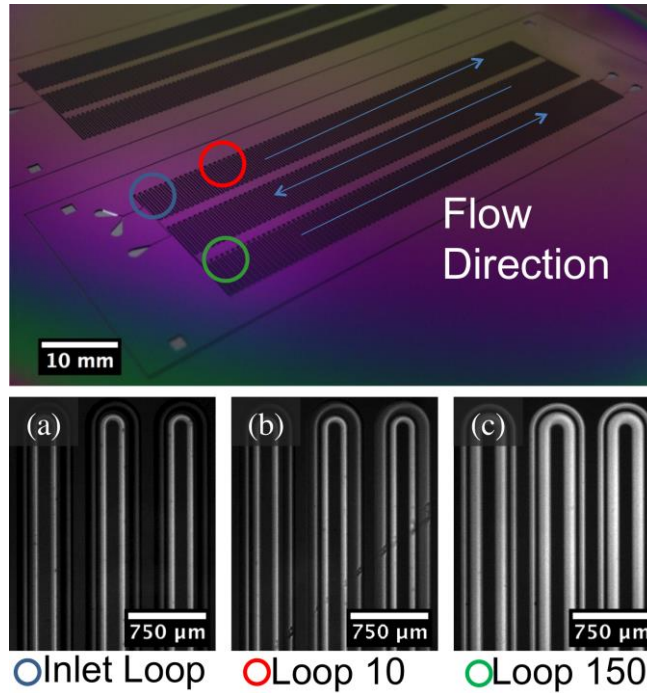


Figure 4 - Diffusion of fluorescein dye under constant flow. Top image shows the flow direction through the serpentine channel and the dots represent sampling points. (a) At the inlet fluorescein is in one channel only. (b) Diffusion begins within 92 μ m of the inlet, 5% of the total length. (c) After 1.2m, 66% of the channel, signals from each channel are similar.

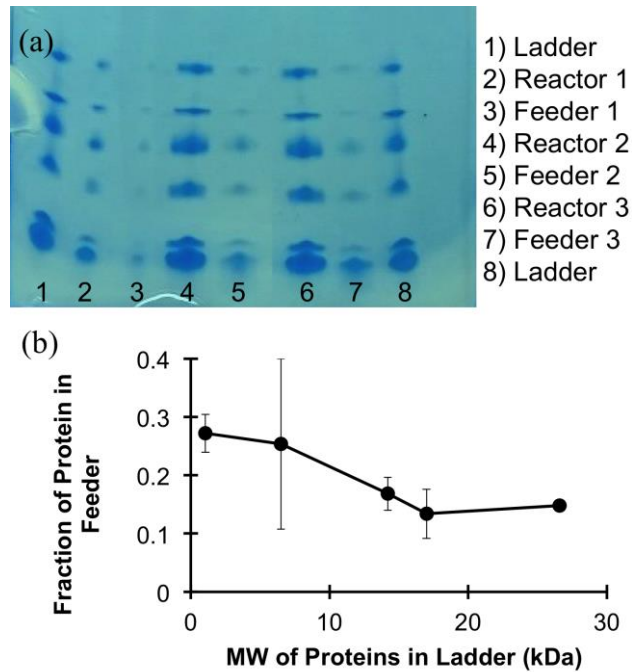


Figure 5 - Protein diffusion across the membrane of the nanoporous exchange device. (a) A protein gel run with effluent from the reaction and feeder channels of the device after a 24hr incubation. (b) Analysis of the gel shows that the steepest slope of the graph and the transition between restricted proteins and non-restricted proteins based on molecular weight happens occurs between 6.5kDa and 17kDa.

found in the feeder channel. This transition indicates that below the threshold MW of the membrane, diffusion of proteins is hindered by the pore size. Higher molecular weight proteins found in the feeder channel can result from defects in the membrane. Rather than diffusing through the pores of the membrane, it is possible that the proteins were moving through larger gaps between the PDMS lid and membrane.

The MWCO can be tuned further depending on the application by altering the number of ALD cycles performed. For biological applications, chemical energy and material transport across the membrane can be controlled based on MW. Multi-scale fluidic networks allow the channels to be controlled individually. The large MW components of a CFPS reaction can be contained on one side of the membrane while ATP and amino acids can be replenished from a support channel. The resulting protein can be contained in the reaction channel or allowed to diffuse into the support channel for purification while the reaction continues.

Cell Culture Device

The second fluidic device is designed to control transport of information and energy between nutrient channels and a cell culture chamber. The microporous membrane limits the movement of cells within the fluidic network. Operation of the microporous membrane was evaluated with fluorescent species. Figure 6 shows SEM images of the device and micropores on the silicon and SU-8 master. The pores were measured to be 27 μ m long, 240nm tall, and 1.38 μ m wide.

Transferring these small features to PDMS with conventional soft lithography procedures resulted in a large portion of the pores being sealed to the glass slide. Higher fidelity replication required stiffer PDMS to improve pore yield. Twice as much crosslinker was used in the PDMS formulation and extending baking times to a minimum of 48hr resulted in a stiff PDMS.

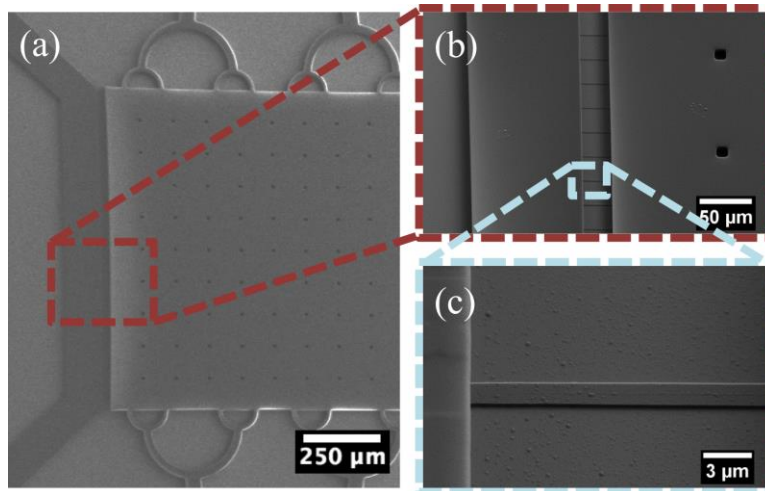


Figure 6 - Culture Device (a) SEM image of the entire device with two culture chambers and two nutrient exchange channels. (b) Expanded view of the membrane separating the nutrient channel and the culture chamber. (c) The pores are 200nm deep by 1 μ m wide and 25 μ m long.

Using these techniques, the 200nm features of the pores could be consistently reproduced. To verify operation of the pores, 750nm beads approximating the size of bacterial cells were flowed through the device. Aggregation of beads at the pores as shown in Figure 7 indicated that there was flow through the pores, but the beads were unable to pass through. Small molecules such as signaling molecules and nutrients were represented with fluorescein dye. Over a period of 30 min, the dye was able to diffuse across the membrane as shown in Figure 7.

Top10 *E. coli* cells expressing GFP were cultured in the device over a 48 hr period. Media was supplied to the culture chamber by the nutrient channel. Figure 8 shows fluorescence images of the device after loading, after 24, and after 48 hr. The cells grew rapidly within the first 24 hr and slowed as they reached a high density. Growth was not uniform across the device, showing higher concentrations of cells at the microporous membrane interface where nutrients were being replenished. This device makes long-term studies possible by providing nutrients to the microbial cultures.

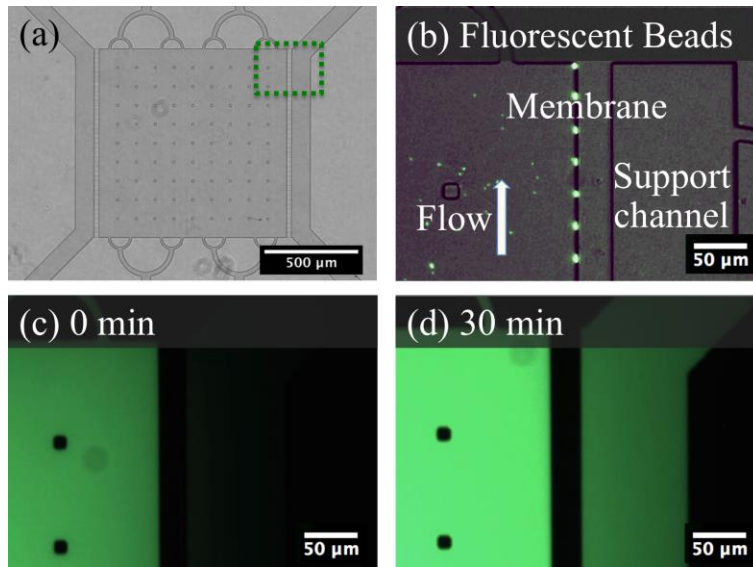


Figure 7 - (a) Overview of the culture chamber device with a dotted outline of the expanded section in b-d. (b) 750μm beads are isolated in the culture chamber and aggregate at the pores under positive pressure. (c) Fluorescein dye loaded into the culture chamber. (d) Fluorescent signal within the support channel increases over 30min due to transport of fluorescent dye.

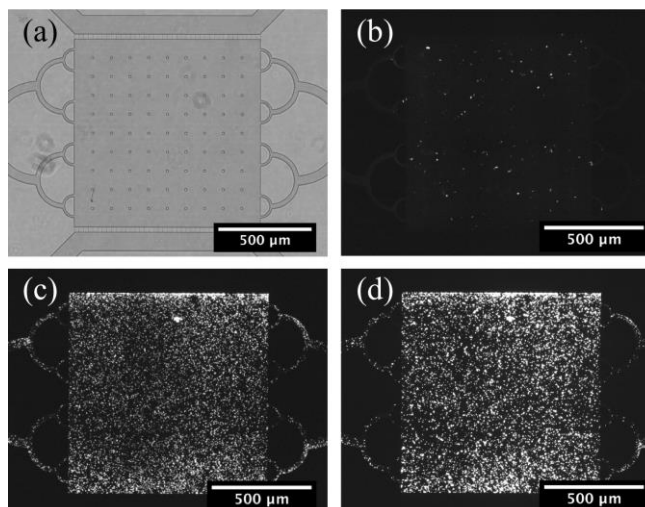


Figure 8 - *E. coli* growth in the culture chamber. (a) bright field image of the culture chamber. Fluorescent images show the chamber after (b) loading, (c) 24hr of incubation, and (d) 48hr of incubation.

The membrane within the device allows cultures to be addressed dynamically through the fluidic network. Cell culture within microfluidic devices can be used to address a number of biological questions pertaining to nutrient replenishment, chemical dosing, stress responses, or cell signaling. Spatial and temporal control over these problems requires the control afforded by multi-scale fluidic networks and specifically, microporous membranes.

Summary and Conclusions

Presently, we have shown that by combining fabrication techniques into multi-scale architectures, complex biological questions can be addressed. The two devices presented represent unique applications of microfluidic membranes, but have common elements in that they address the transport of energy, materials, or information within a fluidic network. The nanoporous membrane device is able to control transport of chemical species with a tunable MWCO. This device has applications in CFPS systems to prolong reactions with ATP and amino acid replenishment. The second device provides a method for interfacing

and culturing cells. Larger microporous membranes confine bacterial cells to culture chambers where they can be addressed via a nutrient channel or other culture chambers. Replenishment of nutrients for long term studies and chemical species can be dosed without perturbing the culture. Each device has unique applications, but the fundamentals of controlling transport are similar.

Acknowledgements

This work was supported by DARPA award HR001134005. The views expressed are those of the authors and do not reflect the official policy or position of the Department of Defense or the U.S. Government. This work was supported by NIH award 1R01DE024463-01 Culturing of the Uncultured. This research was performed at Oak Ridge National Laboratory (ORNL). ORNL is managed by UT-Battelle, LLC, for the US Department of Energy Under contract DE-AC05-00OR22725. The fabrication of nano- and microfluidic devices was conducted at the Center for Nanophase Materials Sciences, which is DOE Office of Science User Facilities.

CHAPTER 3
A NANOSTRUCTURED CO-CULTURE ENVIRONMENT ENABLED
STUDY OF CHEMICAL SIGNALING BETWEEN BACTERIA

Abstract

The architecture of multi-species bacterial communities emerges from the dynamic exchange of chemical and physical signals across the community and between community members and their host(s). Ultimately, this leads to enhanced function and fitness of the system as a whole. The collective response of multiple species across space and time works in concert, allowing the system to react to changes in nutrient availability, confinement, and transport limitations. Conventional culture techniques fail to enable studies of these complex interactions. Developing next-generation co-culture platforms enhances understanding of processes that link different bacterial species via chemical signaling, metabolic exchange, and competition for nutrients. Combining microfluidic approaches and finite element analysis, next generation culture platforms can control key features of chemical communication inherent in the natural environment while providing a more tractable platform to more fully characterize biochemical interactions. The platform consists of two culture chambers and two nutrient channels each separated by nanoporous barriers that support growth through diffusion and allow transport of signaling molecules between cell cultures. The spatial separation of cultures provides the ability to track the growth of each species individually and reduces the impact of crowding, providing room for slower growing bacteria to reproduce. Visualizing the movement of fluorescein dye through the systems and analyzing the growth and response of an engineered sender and receiver system of *E. coli* provided an understanding of transport through the system mediated by diffusion. This understanding was applied to culturing members of the oral microbiome and observing phenotypic changes associated with cross-species chemical signaling. This platform introduces new possibilities for quantifying subtle phenotypic changes within a biofilm subjected to spatial and temporal chemical gradients through analysis of bright field imaging and provides a tractable experimental

platform for building deeper understanding of the role of chemical signaling in shaping microbial interactions.

Introduction

Bacteria living in multispecies communities rely on physical and chemical cues to adapt to changes in their local environment and regulate community dynamics. The rich interplay between physical structure, chemical gradients, and inter and intra-kingdom communication shapes the physical architecture and composition of bacterial communities we observe in nature¹⁶². Traditional culture techniques reduce these complex system to a homogeneous platform that is effective for studying parts of the natural system in a controlled and measurable way, but eliminate the complex trophic interactions from interdependent metabolisms⁸⁹ and competition for resources¹⁶³ and signal exchange that impact co-evolution and spatial organization¹¹⁷. Studying these systems in their natural state also has its own drawbacks such as lacking access to information about spatial organization and limited control over the changing environment at a comparable scale. Microfluidics provide an intermediate for these two approaches combining key spatial and temporal properties of a natural system with the control and imaging capabilities of lab experiments. Figure 9 demonstrates this adaptation from the natural environment (a) to microfluidic platform (b).

Understanding which aspects of nature to replicate is critical to developing an effective microfluidic platform. Chemical communication among bacteria can be mediated through multiple quorum sensing (QS) molecules as a community density dependent signal^{90,164}. QS molecules are able to illicit changes in morphology by changing gene expression in the cells,⁹¹ whether it is motile bacteria transitioning from planktonic to sessile states, or increasing extra-cellular matrix (ECM) production¹⁶⁵. These changes regulate both colony growth and competition as well as provide resistance to antibiotics¹⁶⁶. Signaling events

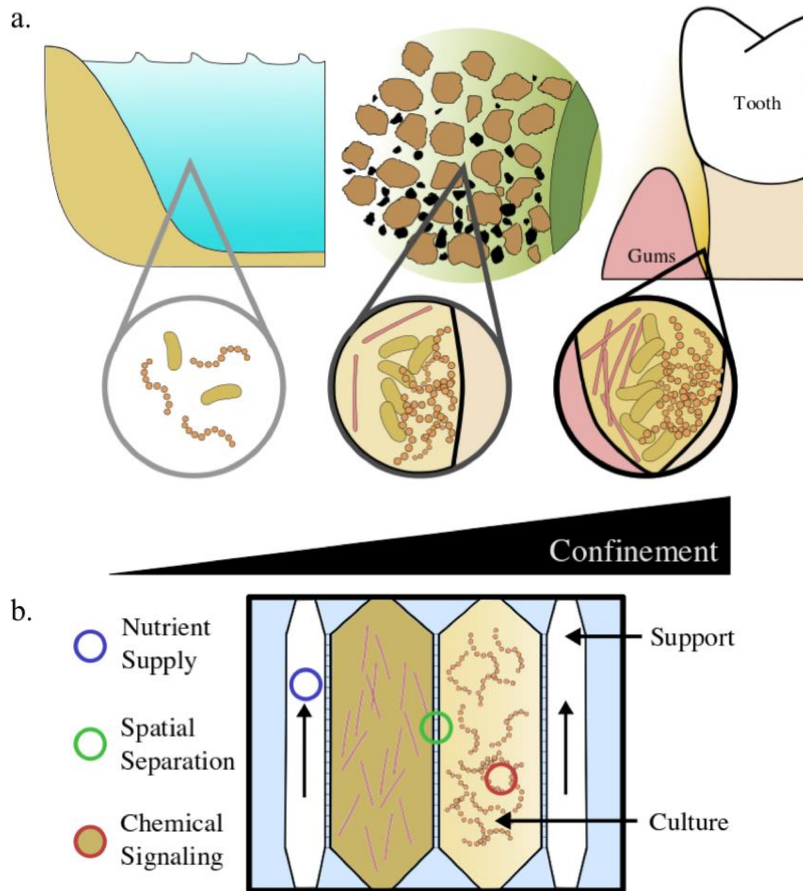


Figure 9 - Microfluidic design overview. (a) Natural environments are heterogeneous and vary in confinement and inversely, how they facilitate communication. Confinement varies across environments. (b) Confinement levels across natural environments mediate nutrient availability, spatial confinement, and chemical signaling. To incorporate these aspects into our platform (b) nanoporous barriers enable communication between spatially separated cultures and are maintained by support channels.

between species and across kingdoms impact the recruitment of microbes that become part of the host microbiome and the immediately surrounding environment^{108,162}. Current assays often aim to quantify these types of interactions by using a single measurement of culture density or specific fluorescently labeled biochemical activity rather than observing morphological and temporal changes in a community development.

While concepts discussed above are generally applicable to the study of microbial community development and signaling, this study focuses on the culture and interactions of members of the oral microbiome. The oral cavity is a highly variable environment with severe spatial and temporal fluctuation in hydrodynamics, nutrient availability, and oxygenation. Biofilm forming attributes of the oral microbiome are essential to community survival in this rapidly changing host environment. If this community makeup shifts, the state of the microbiome can shift from healthy to diseased, but what causes this shift is not well understood. One quorum sensing mechanism that has been studied in the oral microbiome is mediated by the auto-inducer two (AI-2) molecule involved in regulation of biofilm formation among oral bacteria^{121,163,167}. AI-2 produced by *Fusobacterium nucleatum* increased biofilm formation in *Streptococcus gordonii*¹²³. The EPS production has been measured by labeling the EPS with crystal violet and short term co-culture aggregation was shown to increase in co-culture with *F. nucleatum* under flow¹²². Using microfluidics, these interactions can be observed over longer periods of time to allow the study of morphological changes in biofilms in co-culture^{106,168,169}.

The heterogeneity of biofilms results from variation in oxygen content, nutrients, shear rate, and signal molecule concentrations throughout the environment. Microfluidics have been used to reconstruct aspects of the natural environment for cell culture with refined control over such parameters. Platforms that describe control over confinement and connectivity^{83,84,170}, temperature¹⁵⁵, chemical gradients^{79,80,102,155,171}, oxygen content^{16,172}, and shear^{70,173} have been

demonstrated. Combined with the ability to image and measure the community over time these tools can offer insights into the mechanisms that shape biofilm development^{94,101}. Co-culture configurations apply this control to interaction assays between bacteria or bacteria and a host organism. The introduced platform implements spatially separate culture chambers to isolate the chemical signaling and allow for imaging of individual species without fluorescent markers. Working with bacterial cells, the barrier must be on the order of hundreds of nanometers to confine cells, 100nm deep exchange channels in silicon have been used to provide nutrients to a culture^{155,160,174}, and we previously demonstrated 200nm pores in PDMS²⁸. With spatial separation of the culture chambers, flow can quickly remove any signal molecule being produced before it can reach concentrations needed to alter the system⁹⁵⁻⁹⁸. By moving nutrient supply to separate support channels, nutrients in the culture chambers were provided by diffusion across high resistance nanoporous barriers while maintaining a no-flow condition within the culture chambers to enable signal accumulation.

Imaging captures the impact of the chemical signaling by documenting changes in community morphology. Computer modeling is able interpret these observations by providing an understanding of the chemical gradients that form within the chambers as a result of the growing microbial communities. PDE based models of signaling and growth have provided a clear picture of chemical gradients and how they buildup within a growing biofilm within larger scale reactors¹³⁰. These types of models have also shown the effect of flow in microfluidic channels on quorum sensing in a biofilm¹³¹. The model implemented with our co-culture platform was a quasi-steady-state PDE based diffusion-reaction model to incorporate signal molecule production, diffusive transport, and abiotic degradation through the platform. Culture chamber coverage measurements from experiments were used to define the culture size at steady state time points. The results of the model show how signal molecules, produced

by one species, build in concentration within the culture chambers and diffuse across the nanoporous barriers. This brings an understanding of the signal gradients that are contributing to the response seen in the receiver chambers.

The co-culture platform was designed around facilitating analysis of biofilm growth using fluorescent markers and bright field imaging and allowed for the coupling of experiments and computational models to better understand the communication between species and morphological changes that they create. The device was made up of two culture chambers with two support channels on either side separated by nanoporous membranes. Diffusion and stability of the fluidics were tested with fluorescein dye within the chambers. Communication between chambers was validated using sender and receiver strains of *E. coli*¹⁶⁴ and computer simulations of signal diffusion across the nanoporous barriers. Interactions between oral microbes showed changes in morphology of the *S. gordonii* culture when grown in co-culture with *F. nucleatum*. Cluster analysis of the cultures showed that while the overall growth rates were similar between co-culture and mono-culture configurations, the co-culture configuration resulted in significant changes in the aggregation of the *S. gordonii* cells.

Materials and Methods

Cell Culture

Sender and receiver *E. coli* strains were used to visualize chemical signaling between chambers of the device. The PFNK502 plasmid in the sender strain produces a C₄-AHL signal molecule that is exported to the liquid culture media. After uptake by the receiver strain the PFNK503 plasmid is activated when the AHL molecule binds to the rhl repressor and induces expression of GFP in the cell. The production of these two *E. coli* strains was covered previously^{175,176}. Both plasmids contain kanamycin resistance as well. Sender and receiver strains were grown in Luria-Bertani (LB) broth and on LB agar plates with 50mg/ml kanamycin. For receiver-only experiments, the supernatant

of an overnight culture of sender cells was filtered through a .22mm syringe filter and diluted into fresh LB broth to create a crude extract of the signal molecule. Signal stocks were kept at -20° C. Receiver cultures were incubated for at least three hours and washed prior to loading. For sender and receiver experiments, both strains were grown up from a plate for at least three hours and washed prior to loading. Oral microbes consisted of *Fusobacterium nucleatum* and *Streptococcus gordonii*. The strains were grown in brain heart infusion (BHI) media with 0.2% dextrose under a nitrogen environment. Prior to experiments, the microbes were reinoculated and grown overnight.

Microfluidic Device Fabrication

The techniques for fabricating a PDMS culture chamber with sub-micron pores to contain bacterial cells was demonstrated previously²⁸. The device design has been optimized as shown in Figure 9B to better control the environment and provides more nutrients to the culture. The microfluidic design consists of two 200 µm wide support channels flanking two larger 500 µm wide culture chambers. Both are 1 mm long with a channel height of 10 µm. Between each of the channels are 10 µm thick nanoporous barriers that have 400 nm tall and 1 µm wide pores at a pitch of 10 µm that allow nutrients and other small molecules to pass through while confining bacteria to the chamber they were loaded into. Fabrication is done with three layers of photolithography. The first layer is a 400 nm thick silicon dioxide layer for the pores patterned with Microposit-NFR resist and dry etched to the silicon substrate surface. SiO₂ was used to provide a more even layer thickness to reduce the chances of membrane failure. The final two layers were created by patterning SU-8. The first layer was a 10 µm thick SU-8 2010 layer spun at 3k rpm. This layer was exposed with the pattern the culture chambers and support channels. The second layer was SU-8 2050 spun at 2,500 rpm and patterned to form the larger channels to a thickness of 40 µm. Both SU-8 layers were developed in a single step using the puddle

method and developed devices were annealed on a hot plate at 250°C for 10 min. Devices were silanized with trichloro(1H,1H,2H,2H-perfluorooctyl) silane (Sigma-Aldrich) by storing in a closed glass container with 20 µl of silane, at 85 °C for 2h.

PDMS (Dow Corning), at a 10:1 polymer to crosslinker ratio, was cast over the SU-8 mold, degassed in a vacuum chamber, and cured at 75°C for 1.5 hours. The PDMS devices were removed from the mold and cured at 75° C for at least two days to fully cure the PDMS and remove any residual solvents. For fluorescein dye and sender/receiver experiments, inlets and outlets were punched with a dermal punch and the devices were plasma bonded to a 1x3 glass slide (VWR). For anaerobic bacteria experiments, three devices were molded together and attached to the bottom of a 48-well plate (Corning) using a previously demonstrated method (manuscript in process). The well-plate was then used to interface with a Bioflux™ pressure controller (Fluxion) under an anaerobic environment.

Well-Plate Microfluidics Fabrication

Even simple microfluidic devices often require complex and expensive pumping and valving systems for accurately metering and controlling fluid flow. This often necessitates substantial and time-consuming set-up, and sometimes make these chips unwieldy and difficult to image. It can also represent a significant departure from the rather straight forward process of pipetting fluids from one small volume to another, making adoption by non-microfluidic experts unlikely. However, the recent development of well-plate microfluidics provides a high throughput, simplified method for studying fluid exchange and shear flow, while minimizing the set-up and need for multiple fluid connections. Here, individual wells can be interconnected via custom microchannels in a polydimethylsiloxane (PDMS) device attached to the bottom of the well-plate. The desired reagent is then added to an inlet well and, driven through the

underlying channel network into an outlet well via hydrostatic pressure or a pressure control system^{177,178}.

With the use of this platform, flow can be introduced into traditional well-plate studies allowing various physiological conditions to be more closely mimicked. Further, the compatibility of these custom devices with well-plate microfluidic control systems provides the opportunity to precisely and dynamically control experimental conditions including temperature, pressure, and gas environment^{177,178}. The use of multi-well plates also allows for multiple devices to be bonded in parallel to the same plate, increasing throughput without increasing the complexity of the control system¹⁷⁹. Additionally, the familiarity and ubiquity of the well-plate platform provides a familiar platform for technical professionals within the lab and is automatically compatible with the host of microscope stage attachments already available for use with conventional well-plates.

While successful bonding of PDMS to polystyrene(PS) has been demonstrated^{4, 5}, the process of bonding customized PDMS devices to well-plates for well-plate microfluidics has only been vaguely described by the commercial vendors that provide compatible pressure controllers^{179,180}. Herein, two approaches are presented that utilize either (3-Aminopropyl)triethoxysilane (ATPES) to modify the surface of the PS well-plate to bond with plasma treated PDMS, or uncured PDMS to act as a glue between the PS and PDMS surfaces¹⁸¹. While the APTES modification provides a stronger bond without adding additional material, the uncured PDMS bonding procedure requires less pressure, avoiding any distortion of nanoscale features. An overview of the process is shown in Figure 10.

Well-Plate Preparation

Prepare the well-plate by drilling a hole in the center of each well corresponding to an inlet or outlet on the PDMS replica (Figure 11). Using an X-Acto knife, clean the edges of the drilled holes such that the bottom surface of

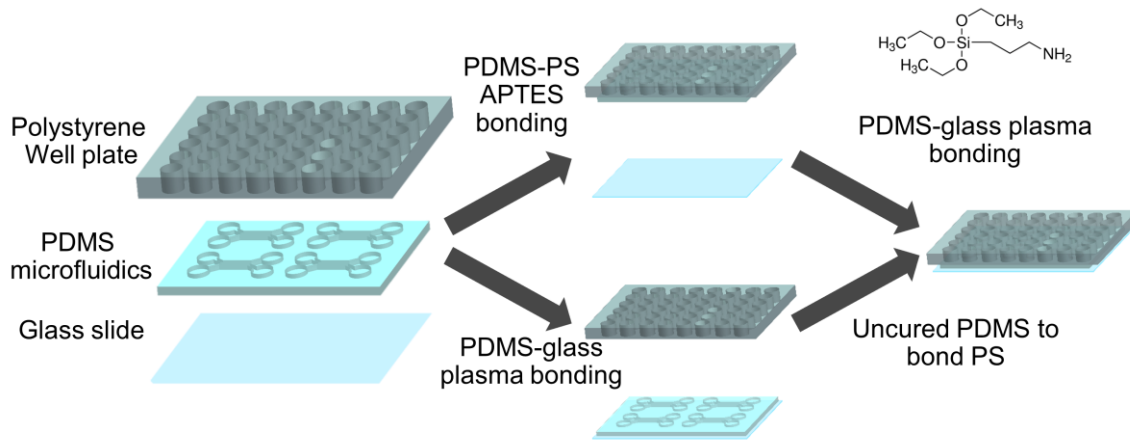


Figure 10 - Diagram of the fabrication process with the APTES process above and PDMS glue below.

the well-plate is smooth and any lips that may have formed from drilling have been removed.

APTES Bonding Procedure

The bottom surface of the well-plate was cleaned with IPA and exposed to oxygen plasma on high setting for 2 minutes, with the bottom surface of the plate facing up (Figure 12a). In a fume hood, a 100 mL aqueous solution of 1% v/v APTES was prepared and poured into a shallow, resealable container. The plasma treated well-plate was placed in the APTES container so that the bottom surface of the plate is completely submerged. The container was sealed and the plate soaked for 30 minutes (Figure 12b) The plate was removed from the APTES bath and rinsed with water. The well-plate was dried using compressed air and heated on a 50°C hot plate to ensure thorough drying.

Assembly

The top of the PDMS replica (opposite to the channels) was cleaned using clear adhesive tape and plasma cleaned on high for 1 minute. With the channeled side of the PDMS replica facing up, the inlets/outlets of the replica were aligned with the holes of the APTES-modified well-plate and joined

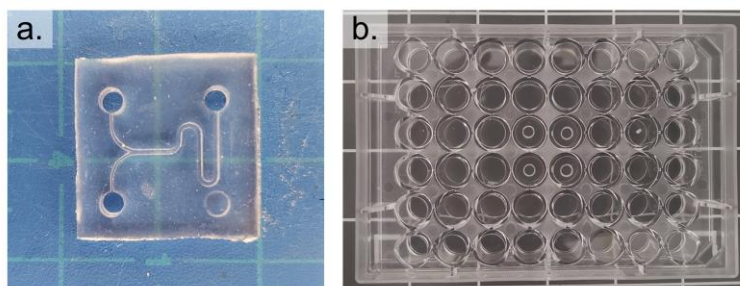


Figure 11 - The prepared PDMS device is shown in a. and the prepared well-plate is shown in b.

together. A brayer was rolled over the surfaces to remove any bubbles and ensure an even, uniform bond. The device was baked at 75°C for 20 minutes (Figure 12c). The well-plate with bonded device was removed from the oven and scotch tape removed debris from the channel-exposed PDMS. A glass coverslip was cleaned with IPA and an plasma cleaned with the well-plate on high for 1 minute. The coverslip was bonded to the PDMS replica, thus enclosing the channels and the device was baked at 75°C for 20 minutes.

Uncured PDMS Procedure

Dust was removed from the bottom (channel-exposed) side of the PDMS replica using clear adhesive tape and a glass coverslip was cleaned with IPA. Both were exposed to oxygen plasma for 1 minute on high setting and bonded together, enclosing the channels. The device was baked at 75°C for 1 hour (Figure 13a). The bottom surface of the prepared well-plate was cleaned with IPA. Using the tapered tip syringe, small droplets of uncured PDMS were placed onto the bottom surface of the well-plate (Figure 13b). Using clear adhesive tape, dust was removed from the top (opposite to the channels) of the coverslip-bonded PDMS replica. The inlets/outlets of the device were aligned with the holes of the well-plate and pressed onto the well-plate and baked at 75°C for 1 hour (Figure 13c).

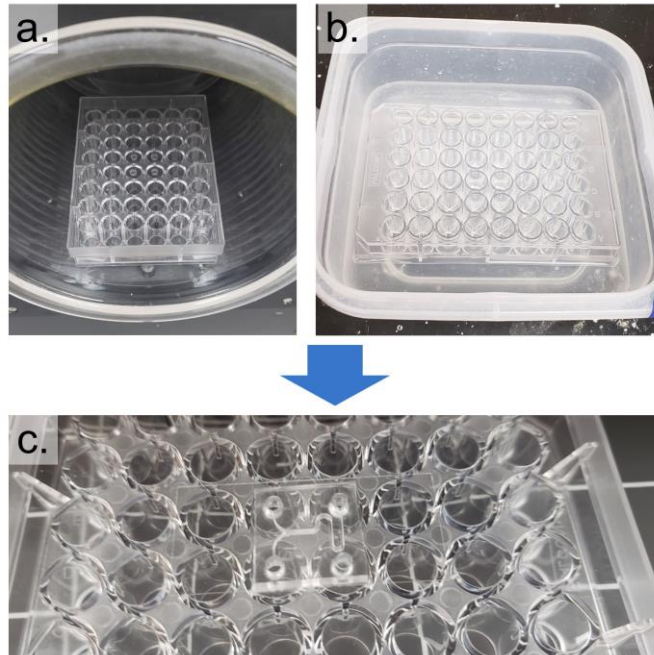


Figure 12 - The well-plate was exposed to air plasma and submerged in a water/APTES solution to modify the surface chemistry and enable bonding between PS and PDMS. A coverslip was then plasma bonded to the PDMS surface.

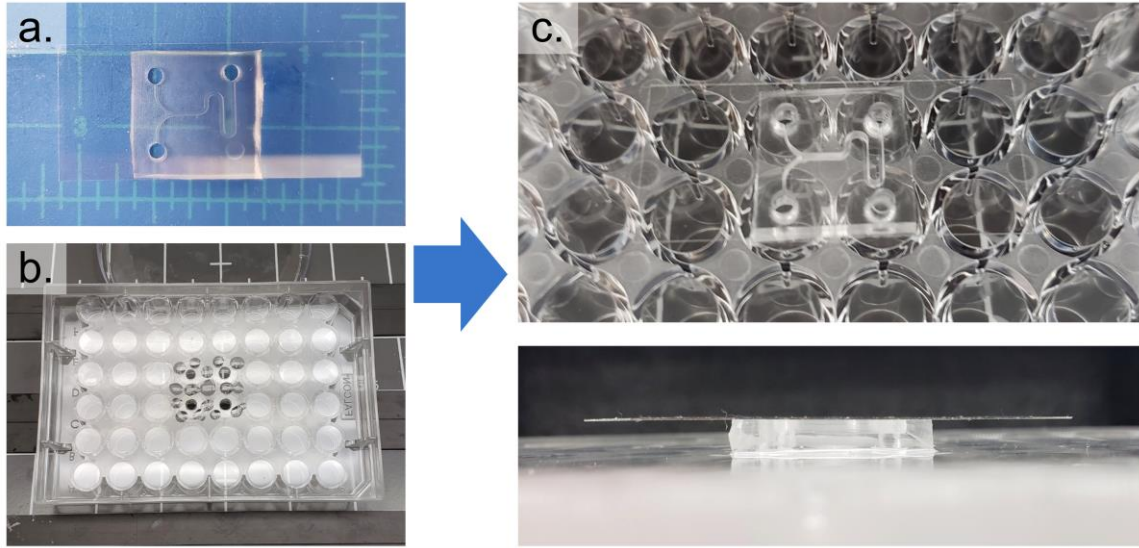


Figure 13 - The PDMS device was first bonded to a coverslip (a) and then bonded to a well-plate using uncured PDMS (b). c shows the completed device from the top and side view.

Two methods for attaching PDMS microfluidic devices to polystyrene well-plates were presented to provide the opportunity to utilize customized channels for well-plate microfluidics. Assays using these devices can be run in conjunction with well-plate microfluidic controllers or using simple pipetting methods by adding the desired reagent or media to the inlet wells (Figure 14). While the fabrication process is more involved than typical PDMS processing, well-plate microfluidics removes the need for complicated tubing connections by working with a single manifold controller, or hydrostatic flow using the well height to produce pressure.

Imaging

Characterization of the microfluidic devices was done with fluorescein dye in phosphate buffered solution (PBS) on an Olympus IX51 inverted epifluorescent microscope. Live imaging of the sender and receiver *E. coli* was done on a Nikon Ti-U microscope with a stage top incubator to maintain temperature and humidity in the cultures over extended periods. Flow control on both the Olympus and Nikon microscopes was accomplished using Harvard Apparatus syringe pumps. Oral microbe experiments were imaged on a Zeiss AXIO Observer Z1 with a Fluxion Bioflux™ incubator and pressure controller. All the images taken were background corrected and analyzed using imageJ software¹⁸², Biovoxxel plugin to imageJ, and Python. Background correction decreased variation caused by variations in illumination and facilitated image analysis. Biovoxxel was used to analyze cluster formation in oral microbe cultures, and the results were visualized in Python and Matplotlib.

Modeling

A model of the microfluidic platform was developed to determine the relative concentrations of acyl-homoserine lactone (AHL) that were being produced by the community and how they accumulate within the platform.

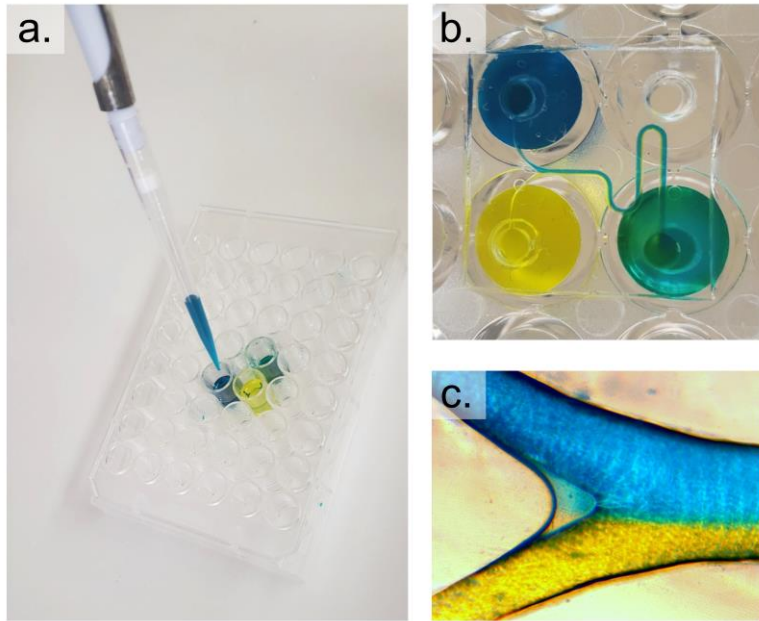


Figure 14 - Operation of the well-plate microfluidics can be done with either a pipet as shown (a) or a well-plate manifold pressure controller. The hydrostatic pressure within the wells is enough the cause flow through the fluidic channels (c) and fill the outlet well (b).

This system was developed in COMSOL Multiphysics® on a Dell workstation computer (Intel Xeon CPU, 64Gb RAM, Nvidia GeForce GTX 750Ti graphics card) using a time dependent solver to study transient development of the chemical gradient across the chamber. The model was a 3D quasi-steady-state finite element analysis of the microfluidic chambers, support channels, and nanofluidic membranes separating them.

During experimental characterization, there was no appreciable flow through the culture chambers during operation. Consequently, transport in the model was diffusion mediated only. The chemical signal was produced within the “sender” cells at a constant rate α and went through abiotic degradation at a constant rate $\sigma[\text{AHL}]$. The signal was not affected by the presence of receiver cells. The size of the cell cultures was taken from experimental values at 0, 8, 16, and 24 hours and estimated as a circular colony within the chamber. The chamber coverage at the given times was 0.0205, 0.2042, 0.3533, and 0.3779 respectively. A parameter sweep of the chamber coverage levels was completed with independent time dependent solvers. At each time point, the chemical gradient reached steady state after approximately two hours and the steady state values were used as the concentration profiles within the chambers at the different time points.

A PDE based approach adapted from Frederick et al. allowed the geometry to dictate the model characteristics¹³⁰. Fick’s second law of diffusion, shown in Equation 1, governs the diffusion reaction model of AHL within the microfluidic chambers. C_{AHL} is the concentration of AHL, D_{AHL} is the spatially dependent diffusivity constant, and R_{AHL} is the production rate of AHL. The diffusion rate of AHL through the cell cultures was half the diffusion rate through media from previous studies^{130,183}. The values used in the equation are shown in Table 1.

Equation 1

$$\frac{\partial c_{AHL}}{\partial t} + \nabla \cdot (-D_{AHL} \nabla c_{AHL}) = R_{AHL}$$

Table 1- Parameters and their values that are incorporated into the model

| Parameter | Value |
|--------------|---|
| C_{AHL} | Dependent variable |
| D_{AHL} | <i>culture</i> , $2.6 \cdot e - 10$ <i>media</i> , $5.2 \cdot e - 10$ |
| α | 9200 μ M/day |
| σ | 0.1109 |
| R_{AHL} | <i>sender</i> , $\alpha - \sigma \cdot c_{AHL}/day$ <i>other</i> , $-\sigma \cdot c_{AHL}/day$ |
| D_{eAHL} | Dependent variable |
| ϵ_p | 0.1 |
| T_F | 1 |

The nanoporous membrane dividing the chambers was modeled as a solid membrane with a porosity of 0.1 and tortuosity of 1 to represent the patterned, straight pores. Modeling the individual pores became computationally intensive due to the large variation in sizes between milliscale chambers and nanoscale pores. The continuous membrane at 400nm was a balance between the two systems. The effective diffusivity of the signal molecule through the membrane was throttled using Equation 2 to represent the low porosity of the membrane. D_{eAHL} is the effective diffusivity of AHL through the membrane, ϵ_p is the membrane porosity, and T_F is the tortuosity of the pores. These values are also shown above in Table 1.

Equation 2

$$D_{e_{AHL}} = \frac{\varepsilon_p}{\tau_F} D_{AHL}$$

The microfluidic model utilized Dirichlet boundary conditions for the support channels and a Neumann condition elsewhere. The boundary conditions representing the support channels held a constant concentration of zero. This represented the flowing support channels as a sink for the signal. There was a no-flux condition across the rest of the boundaries.

Experimental Procedure

Characterization of Chemical Gradients

The characterization of the device was done with fluorescein to visualize the movement of molecules within the microfluidic devices. The operation of the devices was done by filling all the chambers with PBS and flowing fluorescein dye in one support channel while flowing buffer solution in the other support channel at the same flow rate, 30 $\mu\text{L/hr}$. The resulting gradient forms as fluorescein diffuses from one side to the other. Images of the chambers were captured over time and analyzed. Images and quantified data illustrate the transient and steady state behavior. When the support channels flow rates were changed to be different (1 and 200 $\mu\text{L/hr}$) the net pressure difference between the channels caused flow to change the concentration within the chamber.

Microbial Signaling Experiments

The sender and receiver strains of *E. coli* were loaded into the culture chambers of the device. The flow to the chambers was then stopped, and flow of media through the outer support channels was started. Images were collected at specified intervals using fluorescence and brightfield channels. Work with oral microbes was done in a similar manner. The oral microbes being tested were loaded into the two center culture chambers and flow was then shutoff to the

chambers. BHI media was then pumped through the support channels to replace consumed media within the chambers. While culture was done in an anaerobic environment, the experiments were carried out under semi-anaerobic conditions of the Bioflux™ controller. Backing air in the system is anaerobic, but the system was not contained in an anaerobic chamber. Experiments were run with a pressure of 0.1psi in the nutrient channels.

Results and Conclusions

Signal Gradient Across Chambers

Chemical transport through the microfluidic platform was examined prior to introduction of cells. Fluorescein dye and PBS buffer were perfused through opposite support channels to determine the diffusion characteristics of small molecules through the system. The fluorescent signal within the no-flow culture chambers was monitored as a steady gradient formed. Figure 15a shows the fully developed steady-state gradient with the line profile shown in b. With the sender/receiver system, a similar gradient was established with AHL signal in Figure 15c. Both chambers were filled with receiver cells and the left support channel was perfused with supernatant from an overnight culture of sender cells. In the composite image the chamber adjacent to the signal channel shows higher GFP expression than the culture chamber farther from the signal. From the model and fluorescein experiments the exact concentration in each channel can be tuned by altering each of the support channel concentrations.

The high hydrodynamic resistance of the nanoporous barriers caused the fluorescent profile to assume a step-function type profile. Advection dominates transport when high porosity barriers are used as shown in Figure 19. While the high resistance of a patterned barrier slowed down the transport of nutrients into the culture chambers, they have two distinct advantages. Lowering the diffusion rate allowed the signal molecules produced by bacteria to build up within both culture chambers, and the high resistance maintains a no-flow condition within

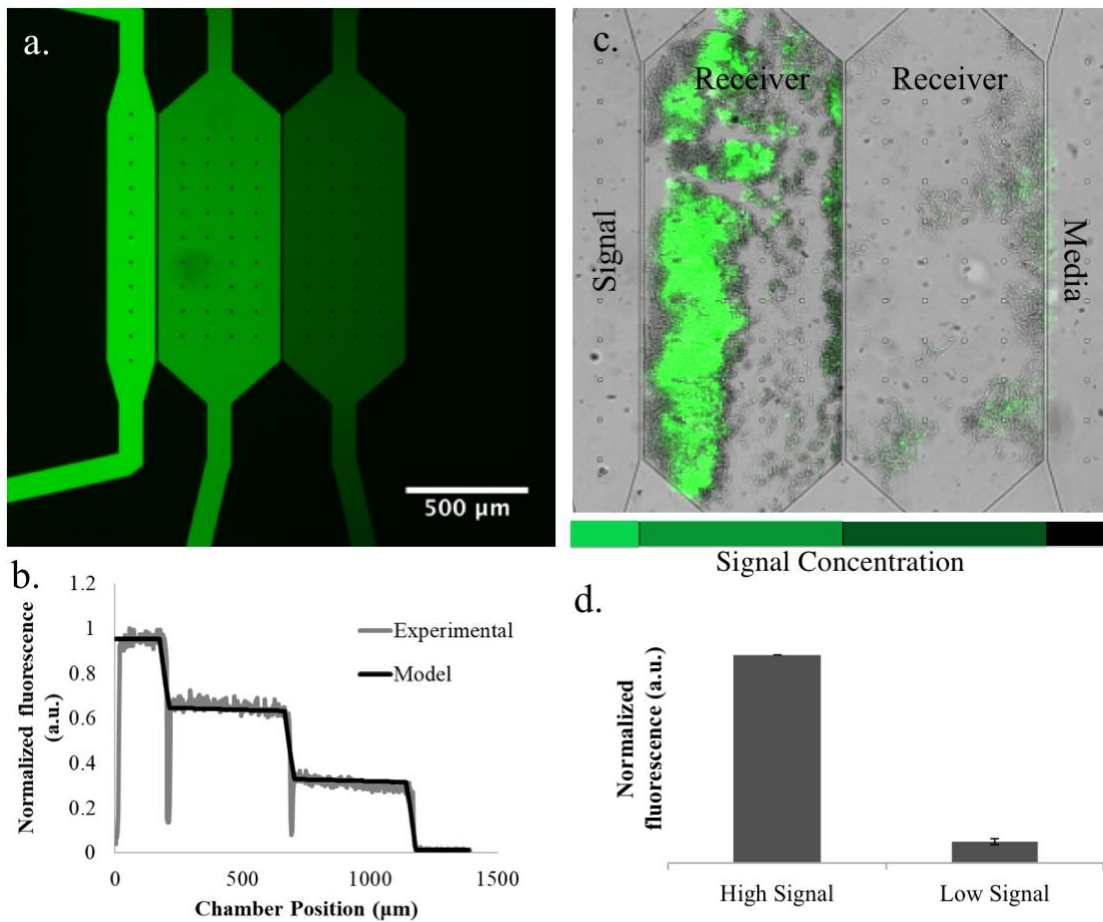


Figure 15 -Chemical gradient profiles measured using model dye and bioreporter. (a) Fluorescein dye and buffer solution flowing through the left and right support channels respectively create a signal profile in the culture chambers through diffusive transport. The fluorescent profile across support channels and culture chambers along with a diffusion-only model is shown (b). (c) Composite image of receiver cells, *E. coli* bioreporter, seeded into each culture chamber. The signal is provided from the support channel on the left. The relative fluorescence of each of the chambers in (d).

the culture chambers without the use of valving elsewhere on the platform. The high resistance was leveraged to virtually eliminate flow through the main culture chamber when flows were minimized in the adjacent support channels. Creating an imbalance between the flow rates of the support channels created a net flow across the culture chambers. Repeated transient switching was also possible using this technique (see supplementary Figure 20).

Cellular Signaling

Signaling between chambers in a co-culture configuration allows the users to observe the growth and development of a ‘sender’ or ‘support’ species that is producing a signal molecule and the corresponding development of a ‘receiver’ or ‘dependent’ strain as they react to a specific signal that diffuses across the membrane. The engineered sender and receiver *E. coli* strains were used to visualize signaling and compare growth and response to an idealized PDE based model. Visualizing the response of the receiver strain allows inference of the concentrations of signal molecule that are present in the receiver culture chamber. Figure 16a shows the ‘heatmap’ for the predicted AHL concentration throughout the device along with the relative concentration between the sender and receiver biofilms.

While the numerical solution of the model is dependent on the exact AHL production rate of the cells, the model was used to build an understanding of the relative concentrations of the AHL signal molecule. The AHL concentration ratio between the two culture chambers was relatively constant at later time points at around 0.4-0.5 receiver/sender average chamber concentration. The overall concentrations within the culture chambers increased dramatically with an increase in the number of sender cells. Figure 16 shows the increase in concentration between the earliest sample and the final communities. These results together are good evidence that the delay in response of the “receiver”

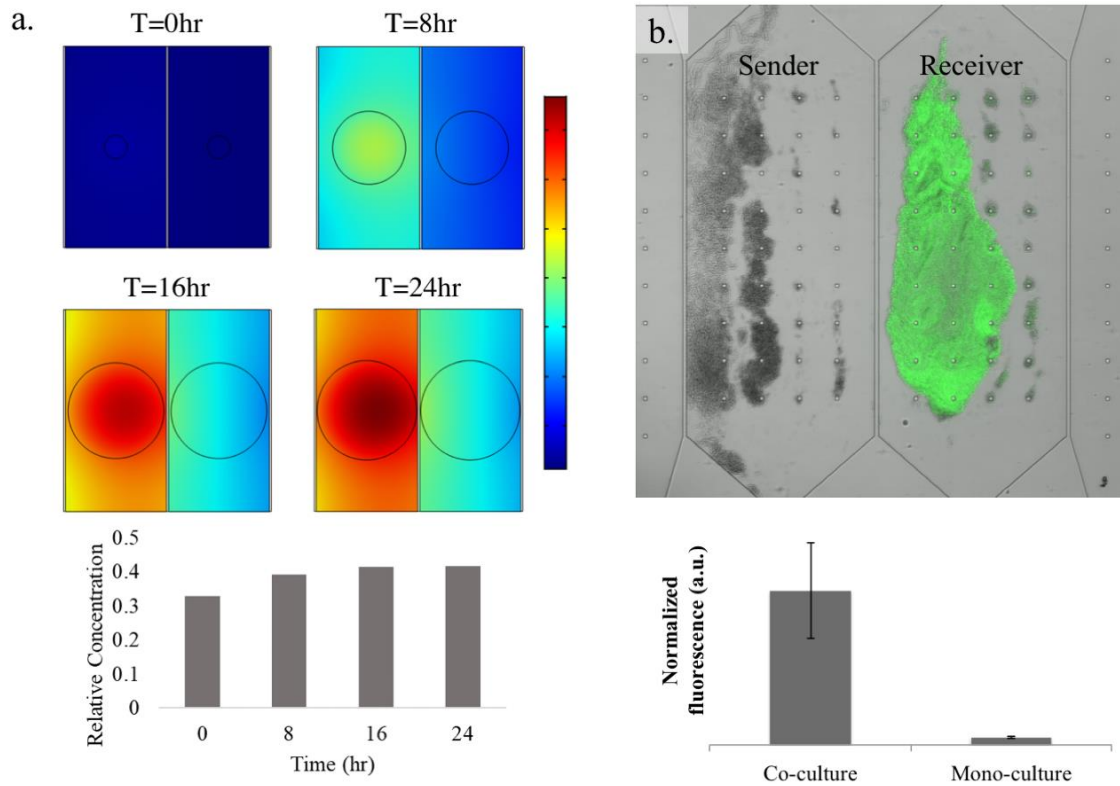


Figure 16 - Engineered sender and receiver signaling and AHL concentration model. (a) A quasi-steady state model built in COMSOL shows AHL concentrations in the culture chambers between 0 and 24 hrs. The relative AHL concentration between the chambers at each of the time points is shown below. (b) Receiver cells produce GFP in response to being grown in co-culture with sender cells. The graph below shows the fluorescence signal increase between mono-culture and co-culture experiments of the receiver cells.

bacteria can be attributed to a lower concentration in spatially separate cultures as compared to a mixed culture experiment.

The experimental results showed that the receiver cells produced GFP when cultured adjacent to sender culture. Even at less than half the concentration of the sender chambers, signal molecules built up within the receiver chamber and induced GFP production (co-culture) as shown in Figure 16b. The same device without pores in the center barrier shows that there was no GFP production under the same conditions (mono-culture). This model and engineered system of *E. coli* verify that the nutrient supply from the support channels and AHL signal concentration increases within adjacent chambers are ample enough to illicit a QS response from the receiver culture.

Oral Biofilm Signaling

Microfluidic platforms create idealized physical models of natural environments, like the oral microbiome, where nutrient, signal, and hydrodynamic gradients can vary significantly over space and time. As stated previously, *F. nucleatum* has been shown to influence the biofilm production of *S. gordonii* through AI-2 quorum sensing system, and biofilm production within *S. gordonii* causes aggregation of cells¹²². The signaling interactions between the members of the oral microbiome have been studied using fluorescent markers^{121,163,167}, but the approach outlined here allows for monitoring the growth of wild-type bacteria using bright field imaging to measure changes in the same culture over time. Beyond simple cell counts, image analysis was used to extract additional measures of community morphology, namely cluster analysis of stationary cultures over the extent of an experiment. Separated growth chambers make it possible to measure growth rates of individual strains, but additional morphological changes can also be used to assess response. Figure 17 shows the fluidic platform loaded with *F. nucleatum* in the left channel and *S. gordonii* in the right chamber. Figure 17a shows the mono-culture arrangement with a

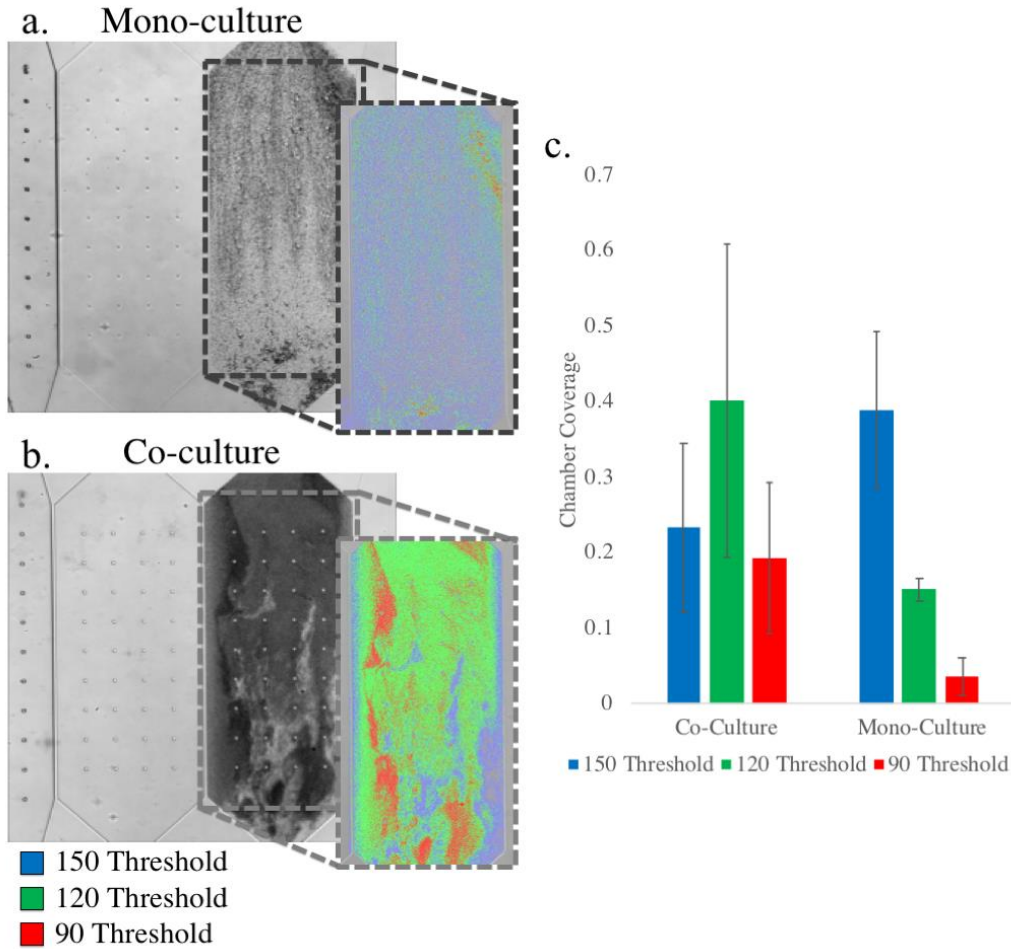


Figure 17 – Brightfield analysis of oral co-culture growth. The *Streptococcus gordonii* culture chamber was thresholded at pixel intensities 150, 120, and 90 to analyze chamber coverage and culture density (inset). Without chemical communication (a) the culture is more diffuse and lighter. In communication with *Fusobacterium nucleatum* (b) the *S. gordonii* forms aggregates. The total growth rate is similar in both cases (c), but the AI-2 causes aggregation of *S. gordonii* (d).

non-porous middle barrier between the chambers, and Figure 17b shows the cultures with a nanoporous barrier, freely communicating. The expanded views show pseudocoloring at pixel intensity thresholds of 150, 120, and 90 to show the variation in culture density as well as the overall chamber coverage of the *S. gordonii* bacteria. From the brightfield histograms of the culture chambers, the peak intensities of the culture area for the co-culture and mono-culture setups were 63 and 139 respectively. The chosen threshold levels covered all cells at 150 and gave levels of contrast between the peaks at 120 and 90 levels. The darker average peak intensity of the co-culture indicate that the cell areas are more dense. The coverage difference at each threshold is shown in Figure 17c. The co-culture case has a variety of different coverages, but the mono-culture is primarily in the 150-threshold level. The overall coverage is similar in both cases, but the coverage at a threshold level of 90 is significantly larger in the co-culture case. Using a two-sample p-test assuming equal variance with one tail analysis between the setups at thresholds of 150 and 90 showed the critical p value at the higher value at 0.249 and a critical p value of 0.028 at the lower threshold. These findings support our hypothesis that growth levels are similar with and without AI-2, but QS results in more dense cultures of *S. gordonii* cells.

Cultures of *S. gordonii* from co-culture (n=3) and mono-culture (n=3) were further analyzed using Biovoxxel to gather information on over 20,000 aggregates. The Matplotlib plugin to python was used to bin the clusters into sizes and plot the resulting histogram. Figure 18 shows the resulting histogram at five hours and 24 hours from the same experiments. Bright field imaging allowed data to be gathered throughout the experiment and does not rely on end-point fluorescent staining that can disrupt the structure of the biofilm during staining and washing steps. At five hours the mono and co-culture setups are very similar in cluster size, but the co-culture setup created aggregates cover over half of the chamber area ($>0.25\text{mm}^2$) after growing with AI-2 available while mono-culture created a range of cluster sizes.

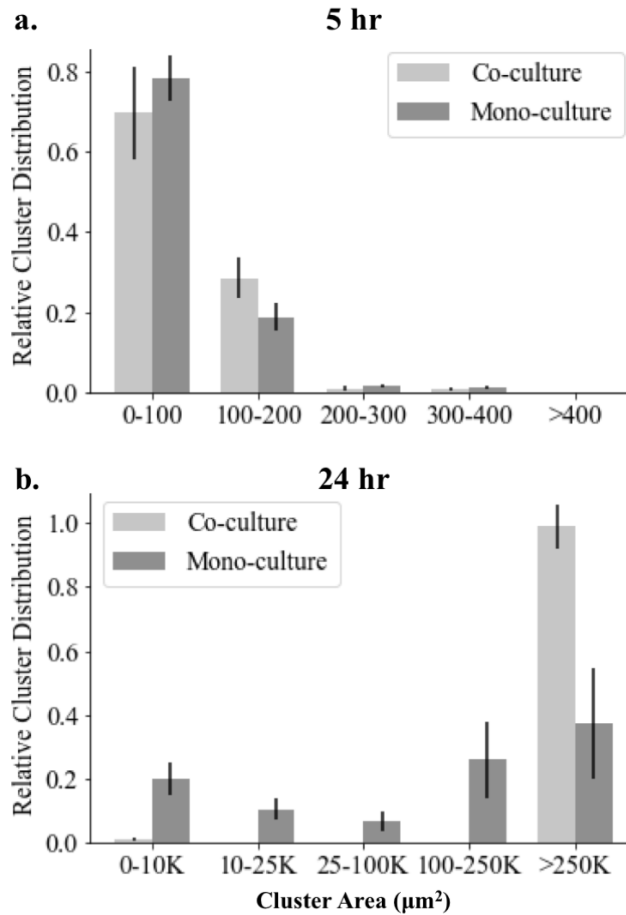


Figure 18 –Cell cluster sizes of *S. gordonii* increase in co-culture with *F. nucleatum* relative to mono-culture at a threshold of 150. (a) At five hours, the cluster sizes of *S. gordonii* with and without AI-2 present are similar. (b) After 24hr culture with AI-2 producing *F. nucleatum*, the average cluster size increased significantly more in the co-culture case.

Conclusion

The microfluidic environment provided a platform to observe and measure chemical interactions between spatially separate, co-cultured microbial isolates and engineered strains under variable chemical gradients. Microfluidics provided nutrients and allowed communication between culture chambers to facilitate long-term growth, no-flow culture conditions, and allowed tuning of confinement and connectivity to enable the observation of quorum sensing between spatially separate cultures. Fluorescein dye showed that a diffusion-only model could be used to predict species transport through the chambers. Engineered receiver *E. coli* responded to varying the concentrations of AHL between chambers to regulate signal response. Culturing the sender and receiver cells in adjacent chambers showed adequate accumulation of AHL signals in the receiver chamber to induce GFP production in the receiver culture.

The platform is tractable for both experiments and modeling where the no flow condition provides a route to modeling 3D diffusion without requiring substantial computational resources. With a quasi-steady state model, the relative levels of AHL for sender and receiver experiments revealed that the AHL concentration within the receiver chamber varied between 33% and 42% of the sender chamber concentration. Models and engineered bacteria provide an understanding of the device operation so that the platform can be applied to targeted biological questions. To measure the effect of QS in the oral microbiome on community morphology, *F. nucleatum* and *S. gordonii* were co-cultured in the platform. The chamber coverage was similar between the cultures matching previous findings, but co-culture experiments showed darker areas indicating a denser culture. Cell aggregation was measured from bright field imaging and showed that *S. gordonii* grown in co-culture formed large aggregates while mono-culture resulted in a diffuse culture. The platform introduced here provides a route to expanding co-culture studies and building upon genomic studies to verify proposed interactions in a tractable way that preserves quorum sensing

behaviors while providing resources to more deeply understand the effects of chemical communication between species and communities.

Acknowledgements

This work was supported by NIH award 1R01DE024463-01 Culturing of the Uncultured. This research was performed at Oak Ridge National Laboratory (ORNL). ORNL is managed by UT-Battelle, LLC, for the US Department of Energy Under contract DE-AC05-00OR22725. The fabrication of nano- and microfluidic devices was conducted at the Center for Nanophase Materials Sciences, which is DOE Office of Science User Facilities.

Appendix

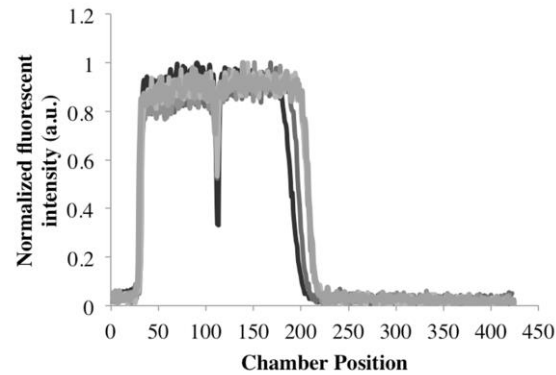
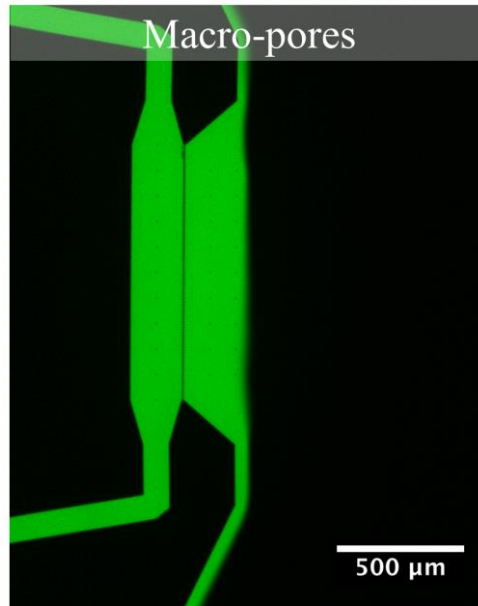


Figure 19 - Large pore fluorescent profile. When the diffusion profile experiment is run with a large pore device, the resulting fluorescent profile has a sharp change in concentration at the center of the culture chamber. This indicates that transport is dominated by advection rather than diffusion as seen in the nanoporous device.

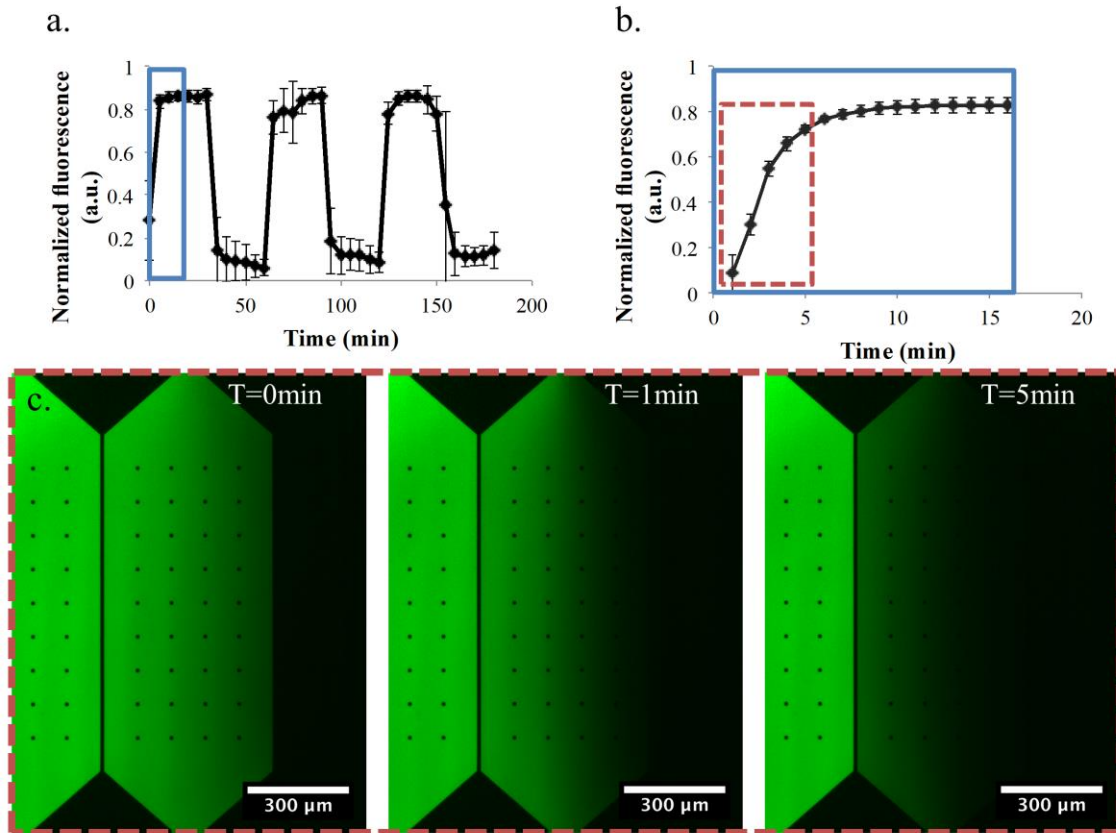


Figure 20 - Signal switching the culture chamber with imbalanced support channel flow rates. (a) The relative flow rate is changed between the fluorescein and buffer support channels every 30 min. (b) shows a detailed version of one transition from the buffer support channel to the fluorescein support channel. (c) epifluorescent micrographs of the culture chamber in the beginning of a transition period at 0, 1, and 5 min.

CHAPTER 4
ACCESSING MICROFLUIDICS THROUGH FEATURE-BASED
DESIGN SOFTWARE FOR 3D PRINTING

A version of this chapter was originally published by Peter G. Shankles, Larry J. Millet, Jayde A. Aufrecht, and Scott T. Retterer:

Peter G. Shankles, Larry J. Millet, Jayde A. Aufrecht, and Scott T. Retterer. "Accessing microfluidics through feature-based design software for 3D printing." *Plos One* 13 (2018): e0192752.

The work presented in this paper demonstrates a new piece of software and a workflow to mold and fabricate microfluidic designs using a desktop 3D printer. This process removes the need for cleanroom facilities to create microfluidics and take advantage of laminar flow regimes resulting in predictable flow patterns. This lends itself to prototyping designs and academic applications where a larger number of designs can be printed for a classroom type setting without taking up time on expensive equipment. This paper also demonstrates its usefulness in simplifying the fluidic architecture of microfabricated designs by creating 3D structures to incorporate with micro and nanoscale features. The process was demonstrated with common biological applications of droplet formation and gradient generation to show the applicability in interfacing biology with the 3D printed microfluidics.

Abstract

Additive manufacturing has been a cornerstone of the product development pipeline for decades, playing an essential role in the creation of both functional and cosmetic prototypes. In recent years, the prospects for distributed and open source manufacturing have grown tremendously. An expanding library of printable materials, low-cost printers, and communities dedicated to platform development has enabled this growth. The microfluidics community has embraced this opportunity to integrate 3D printing into the suite of manufacturing strategies used to create novel fluidic architectures. The rapid

turnaround time and low cost to implement these strategies in the lab makes 3D printing an attractive alternative to conventional micro- and nanofabrication techniques. In this work, the production of multiple microfluidic architectures using a hybrid 3D printing-soft lithography approach is demonstrated and shown to enable rapid device fabrication with channel dimensions that take advantage of laminar flow characteristics. The fabrication process outlined here is underpinned by the implementation of custom design software with an integrated slicer program that replaces less intuitive computer aided design and slicer software tools. Devices are designed in the program by assembling parameterized microfluidic building blocks. The fabrication process and flow control within 3D printed devices were demonstrated with a gradient generator and two droplet generator designs. Precise control over the printing process allowed 3D microfluidics to be printed in a single step by extruding bridge structures to 'jump-over' channels in the same plane. This strategy was shown to integrate with conventional nanofabrication strategies to simplify the operation of a platform that incorporates both nanoscale features and 3D printed microfluidics.

Introduction

Additive manufacturing is poised to change how we design, manufacture, and receive goods ¹⁸⁴. Traditionally, it has allowed engineers and product designers to rapidly produce physical 3D objects in an iterative process to refine ergonomics, identify manufacturing challenges, and communicate marketing concepts rapidly and with minimal cost. The recent availability of a broader range of printable materials coupled with the increased accessibility of lower cost, higher quality printers, and the growth of online innovation and design communities are reshaping how we think about manufacturing and product distribution. Complex, low quantity production parts fabricated by 3D printing have been demonstrated in the aerospace industry ¹⁸⁵. Open source designs for

products like prosthetic limbs are being modified and used across the globe ¹⁸⁶. Retailers are even exploring the use of 3D printers for on-demand product customization ^{187,188}.

In the same manner that it has impacted other industries, 3D printing has begun to capture the attention and imagination of the microfluidics community. Additive manufacturing provides an alternative to conventional microfabrication techniques and allows designers to think about fluidic systems in three-dimensions, (e.g. printing unique modular components that can be pieced together to achieve new functions) ^{58,189}. Issues that had previously slowed the utilization of 3D printing in fluidics such as poor resolution and printer availability are diminishing as printing platforms improve. A recent STL technology has shown internal fluidic channels with dimension as small as $20\mu\text{m} \times 18\mu\text{m}$ ¹⁹⁰. This is minimizing the barriers-to-entry and reducing maintenance costs, thus making 3D printing an attractive alternative to maintaining a conventional cleanroom facility ³⁷.

Direct writing of microfluidic systems with additive manufacturing involves printing the fluidic networks in a resin or thermoplastic so that the channels are fully or mostly enclosed ^{50,191}. Inlet and outlet ports can be designed so that fluidic connections can be made easily with commercially available parts such as Luer locks or compression fittings ^{34,51}. Direct-print polypropylene (PP) devices have been successfully used to create custom multi-chamber platforms for organic chemistry experimentation ^{60,192}. Bhargava et al. demonstrated a parts based system where fluidic components could be printed and assembled much like Lego® bricks to create a fluid network ⁵⁸. Further work has been done to develop whole printed devices that integrate off-the-shelf control features such as valves and pumps ⁵⁶. However, a major disadvantage of the direct-write method is the surface roughness of the final product. While surface roughness may not significantly impact the flow profile of the microfluidics, it can turn transparent materials translucent, preventing high-resolution imaging ¹⁹³. Dolomite

Microfluidics has developed a direct write microfluidics platform that is able to create internal channels, but the exterior surface of the device is still cloudy without substantial post processing or the use of embedded glass windows ^{52,194}. Additionally, many of the resins used are proprietary and biocompatibility and solvent compatibility need to be established for each material ³¹.

3D printers have also been used to fabricate molds for soft lithography in lieu of SU-8 patterning or silicon deep reactive-ion etching (DRIE) ⁴⁶. Masters are created with a 3D printer and the final device material is cast over the design, cured, and removed from the master mold. These molds are primarily used with Poly-dimethylsiloxane (PDMS) ^{39,40}, but have been used with other cast materials such as epoxy ⁴⁸ or Norland Optical Adhesive (NOA)(Norland Products) ¹⁹⁵. We have previously shown that crude acrylonitrile butadiene styrene (ABS) filaments can be hand-shaped and incorporated into a microfabricated silicon mold to connect individual modules and change the fluidic network for a given application to create fluidic bridges ¹⁹⁶, however there is a need for an automated fabrication process for incorporating fluidic bridges into microfluidic systems. Currently, 3D printed microfluidics take less time and require less infrastructure than those created using conventional photolithography, but further advancements are required to make 3D printing a more accessible alternative. Simplifying the design process with more intuitive, application-specific software and implementing a more robust workflow can accomplish this. Groups that want low cost fabrication techniques for quicker turnaround time and teaching purposes can use these techniques to replicate larger microfluidic designs. The FDM process is limited in resolution to a few hundred microns. The highest resolution STL processes can be on the order of 20 μ m. This remains orders of magnitude larger than photolithography or electron beam lithography techniques. As 3D printing technologies increase in resolution, precision, and extrusion uniformity, the principles in this work will improve on-the-fly microfluidics prototyping and

expand the possibilities for creating and using 3D fluidic systems across a broader community.

This work aims to improve the throughput, design process, and optical transparency of 3D printing techniques and strategies for microfluidics. Our feature-based software simplifies the design process by providing a graphical user interface (GUI) for piecing together common microfluidic features into a single custom device. The software's direct control of the printing order allows for quick iteration of small microfluidic features during the print process and control over the conversion of channels into printer operations in a specific order. This ordering allows optimization of both the resolution and stability of the printed master. A filament deposition modeling (FDM) 3D printer was used to print master molds. After printing, a solvent annealing process was used to smooth the channels. Subsequently, PDMS was deposited and cured directly on the print bed. The devices utilized the same bonding techniques and connections as conventional soft lithography. A linear gradient generator and two types of droplet generators were fabricated to demonstrate flow stability and the impact of process optimization on the function of these highly utilized designs. Beyond replicating traditional commonly used 2D fluidic designs, 3D printing and layered microfluidics have been used to create bridging structures, but they require either multiple layers of PDMS bonded together¹³ or 3D printed support material that has to be removed prior to molding PDMS⁴⁸. Our current process prints three-dimensional bridge structures in a single step that can be used to simplify fluidic networks or reconfigure existing microfabricated designs. This workflow provides a method for rapidly prototyping and replicating microfluidics through a streamlined 3D writing and encapsulation process that is beyond current manual placement techniques.

Materials and Methods

Feature-Based Design Software

The software GUI and code were developed in Matlab R2015a for Mac (MathWorks) on a MacBook Air computer (Apple, 13-inch, mid 2012, 2 GHz Intel i7, 8 GB 1600 MHz DDR3). The Graphical User Interface Design Environment (GUIDE) plugin was used to layout the GUI of the program. The GUIDE generated a code structure for each button and menu within the GUI. Utility was added to each of the defined functions with Matlab code. The Application Compiler tool was used to package the GUI for distribution so that it could be run on Windows and Mac systems without a full Matlab license. The CAD software has been made available on Github for both Mac and Windows systems (<https://github.com/shankles/FluiCAD>). The Supplementary folder contains gcode and fig design files for each of the designs used in this manuscript.

Printer Setup

A consumer grade FDM 3D printer (Solidoodle 3, \$799 as of 2013) was used to demonstrate the functionality of the Designer software and the fabrication process. Black ABS plastic in a 1.75mm filament (Solidoodle) was used as the mold material with a 0.35mm diameter nozzle at 200°C. The 200mm x 200mm aluminum print bed covered with polyamide tape (Tapes Master) provided an even surface to cast PDMS (Sylgard 184, Dow Corning) molds. ABS mold material and polyamide covering allowed the PDMS to be cast and cured without adhering to the printer or mold. The Solidoodle system heated print bed was set to 85°C to promote mold adhesion during printing and to cure the cast elastomer. Printing was performed with the extruder at 200°C.

Fabrication Process

Our feature-based design software was used to layout the microfluidic devices. Common parameterized microfluidic features were pieced together to

form the final device layout in Figure 21(a). Features were organized into a list showing the print order. The viewing area was used to visualize the layout of the device as it was being assembled. The design was then converted to a g-code file and sent to the 3D printer host software, Repetier Host (Hot-World GmbH & Co.). Repetier can send commands in the g-code to the printer for manually moving the extruder or stage, extruding or retracting the filament, and heating the print bed and hot end. With modest adjustments to the printer parameters in the design software, the host software and g-code are compatible with any 3D printer running Marlin firmware. The host software allowed for final visualization of the g-code prior to printing.

The design was transferred to the printer from the host software over a USB cord and printed in ABS in Figure 21(b). The heated extruder was turned off and the print bed was set to 50°C. At just under the boiling point, acetone was applied to the device molds using a fine-point paintbrush and allowed to evaporate to solvent anneal the surface of the printed channels. The print bed was then turned off and allowed to cool. A PDMS retaining barrier was placed on the print bed around the ABS mold and liquid PDMS resin (10:1 polymer to cross linker ratio) was cast over the mold. A desiccator lid hooked to a vacuum pump (Gast) was placed on the print bed and used to degas the PDMS. After removing all air bubbles from the elastomer, the PDMS was cured directly on the print bed at 85°C for a minimum of 1.5 hrs.

The cured PDMS was removed from the print bed, the devices were cut out with an X-acto knife (Elmer's), and the ABS mold was removed with forceps in Figure 21(c). At this point the process can be repeated to print additional devices, or an array of devices can be printed simultaneously for higher throughput applications. The remainder of the process follows the workflow of a conventional soft lithography device assembly¹². Inlets and outlets were punched with dermal biopsy punches (Miltex). The resulting PDMS devices were

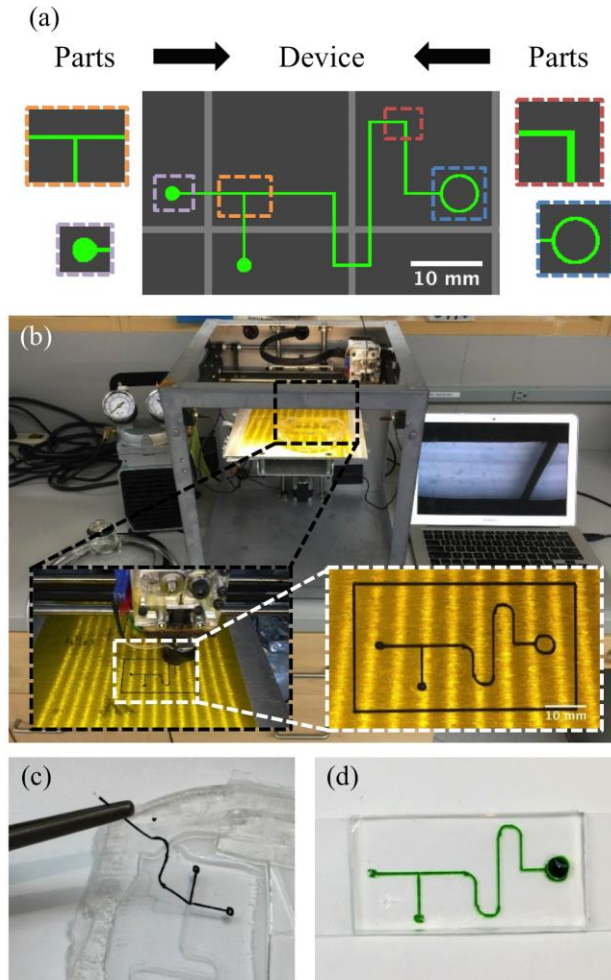


Figure 21 - Fabrication process. (a) The device was designed by combining fluidic parts into a custom fluidic network. (b) The design was sent to an FDM 3D printer. (c) The ABS mold is removed from the PDMS device after being cast on the heated print bed. The device was cut into individual devices, and (d) bonded to a substrate for use.

plasma treated, and can be bonded to glass, PDMS, or silicon substrates. Figure 21(d) shows the device bound to a glass slide and filled with food coloring to show the channels.

Droplet Generator

Two types of droplet generators were constructed as a proof-of-concept for the printing method. A T-junction device and a flow focusing design were chosen based on previous micro-scale work⁷⁷⁻⁸¹. Fluorescein dye (10mM in PBS, Life Technologies) was the aqueous phase and mineral oil was the oil phase. The fluorescein dye was injected at a constant rate (1 μ L/min), while the mineral oil was modulated (2 μ L/min to 20 μ L/min) to control droplet size. Epifluorescent images were taken using a Nikon Ti-U inverted microscope with a FITC filter. The images were analyzed in ImageJ to quantify droplet length within the channel¹⁸².

Gradient Generator

A three-step linear gradient generator was fabricated to test control of fluidic connections. From two inlets, microchannels divide three times to produce five channels that recombine and diffuse in a single channel to form a gradient of the two inlet solutions^{197,198}. The concentrations recombine in a main channel and diffusion evens out the concentrations, forming a continuous gradient¹⁹⁹. Fluorescein dye (10mM in PBS) and PBS were used to characterize the operation of the device. The inlets had a balanced flow rate of 0.5 μ L/min in each. After equilibrium was reached, epifluorescent images were taken on a Nikon Ti-U inverted microscope with a FITC filter cube at each of the channels prior to mixing within the large channel. Epifluorescence images were analyzed in ImageJ to measure the maximum intensity of the fluorescent dye within each channel.

3D Microfluidics

By controlling the extrusion paths of the 3D print head, 3D microfluidics can be fabricated using a bridge structure in a continuous, vertical extrusion process rather than conventional layer-by-layer deposition. The initial portion of the 3mm long bridge feature (600 μ m diameter) is an extruded filament created in the vertical direction away from the print bed, this is allowed to solidify for 3sec prior to completing the bridge by drawing the filament from the top of the vertical post to a user-specified final position on the print bed. The resulting bridging structure is a right triangle with filament spanning the points specified. A “braid” of three channels was fabricated with overlapping channels to demonstrate functionality. The braid printing is demonstrated in Figure 27. The bridge structure is limited to a single filament width (400 μ m diameter). After casting and curing PDMS over the device, the bridge structures can be removed by pulling on the exposed filament. The weakest point at the top of the bridge separates and the ABS mold can be removed in two pieces from either opening leaving open channels through the PDMS.

The bridge structure was combined with microfabricated masters to create multiscale devices. The silicon master contained nanoscale features similar to ones demonstrated previously²⁸. A thin layer of PDMS was spin-coated onto the master (500rpm for 45sec), vacuum degassed, and cured at 75°C for 30min. A fluidic architecture was created in the design software to simplify the network of the silicon master, bridging together inlets and outlets. 3D printed channels were fabricated and cast to form a PDMS replica. The 3D printed PDMS layer was then bonded to the coated wafer to form a multilayer device. The PDMS-to-PDMS plasma-bonded device was baked at 75°C for 10min then removed from the wafer. The inlets and outlets connected by 3D structures were opened with an X-acto knife and the other inlets and outlets were punched with a dermal punch. The PDMS was plasma-bonded to a glass slide to complete the

assembly. With this method, the fluid network of the device can be altered without additional nanofabrication steps.

Results and Discussion

We created an integrated workflow built on a feature driven design platform to produce functional fluidic platforms for common microfluidic applications including gradient generation for chemotaxis and other cellular studies, droplet generation for single cell analysis and small volume reactions, as well as 3D microfluidics that can be used to form complex fluidic architectures and simplify fluidic networks for microfabricated designs by allowing for overlapping channels in a single step. To overcome limitations (lower resolution, surface roughness, and low transparency)^{38,62} of FDM-produced microfluidics, we employ 3D printing with an acetone finishing step to create a smooth microfluidic master for fabricating transparent, 3D microfluidics. By solubilizing the surface of the ABS print with acetone, the surface is chemically polished without greatly altering the channel geometry. The smooth ABS prints were used as molds to cast PDMS devices. Using the heated print bed on the printer, the casting process was done directly where the device was printed, reducing the likelihood of deformation and breakage.

Design Software

The feature-based design software was developed in the Matlab GUIDE environment, and the final program packaging was achieved with the Application Compiler, allowing it to be run on other computers without a full Matlab license. Common 3D printed microfluidic techniques often use CAD software to design fluidic networks. CAD programs provide powerful tools for design, but training and maintenance costs for professional packages are limiting factors. Completed CAD design files are imported to a slicer program that processes the geometry into g-code to be used with the 3D printer. With our feature based design the process is simplified by giving the user a list of

parameterized microfluidic features to choose from in order to build a custom fluidic system. The program writes the g-code to print the device directly. This allows the user to correct any writing problems quickly by changing the printing order, unlike typical slicer software.

The GUI of the program is organized into several operational blocks. The printer parameters are set based on the printer selected for use and the print resolution. The required feature is selected from a dropdown window and the user defines the associated parameters Figure 22(b). The feature is added to the visual area Figure 22(c). The visual area is a graphical representation of the entire print bed. The inserted feature is also added to the feature list at the right side of the GUI Figure 22(d). Features making up the current device can be reordered or replaced with different parameters to improve the printing process. From the feature list, the print order can be changed to quickly correct printing problems. Individual features can be deleted, and the entire feature list can be cleared.

The list of features includes an inlet for tubing connections, a straight channel, an elbow for sweeping corners, a y-intersection to join and separate channels, a ring feature that can be used for radial patterns, and a bridge structure to overlap channels. The parameters to construct each of these parts are based on the coordinate system of the 3D printer bed. Parameters such as starting position and channel dimensions are used to construct each part. Figure 28 shows the list of features available and all the parameters required for each.

With the designs completed, the “write” button creates g-code for each part in the feature list to replicate the device on a 3D printer. The printer parameters and a barrier around the device are written first. The barrier acts to prime the extruder and reveals errors in the print bed calibration (poor adhesion from the print head being too far away or flat or split channels from being too close to the print bed). The features are then written to the file. The Matlab code works through the feature list, writing g-code based on the type of channel being

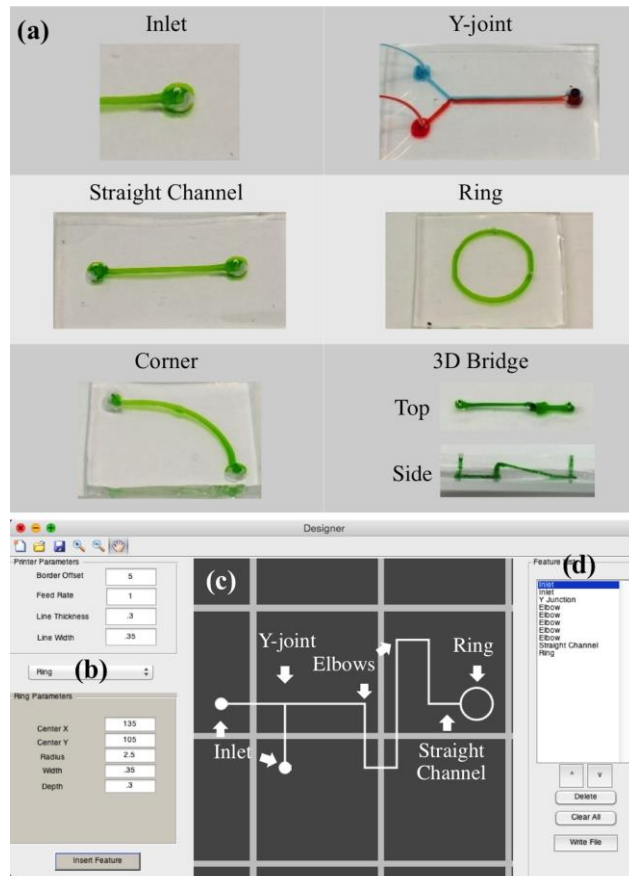


Figure 22 - Feature parameters and program GUI. (a) Table of features available for the design process. The GUI consists of 3 sections (b) the printer and feature parameters are given, (c) the design is represented graphically, and (d) the parameter list of all the parts in the current design for editing.

printed and the parameters of the printer and the individual devices. This g-code can be visualized and sent to the printer using a 3D printer host program. The designs of each of the devices featured in this work are provided in the Supplementary Figure 29.

Printing Process

The 3D printing process focuses on efficient use of the printer's capabilities to print a mold to form channels in PDMS elastomer. The resulting device is a PDMS device that functions in the same manner as those made in traditional soft lithography using silicon masters. The 3D printer used dictates the feature resolution. The Solidoodle printer was able to fabricate channels with consistent results between prints. The characterization results for the Solidoodle printer used are shown in Supplementary Figure 30. By directly writing the microfluidic channel master, designs can be replicated in PDMS, and bonded to glass within 3hr. Figure 23 summarizes the fabrication process. By comparison, the conventional process of fabricating a mold with photolithography using SU-8 or DRIE dry plasma etching of silicon wafers can take several days or weeks if new photomasks have to be ordered rather than fabricated on site.

The resulting printed designs were tested for accuracy by printing a series of straight channels with increasing numbers of filaments in width and height. For a single filament extrusion, the channels were on average 180 μ m deep and 940 μ m wide with a standard deviation of 2 μ m and 14 μ m respectively. As the number of filaments increase in the width of a channel the width increased by 470 μ m (n=3, SD \pm 240 μ m). Stacking layers to increase the channel height adds an average of 270 μ m (n=3, SD \pm 46 μ m) in channel height. Using a smaller diameter extruder tip can potentially reduce these incremental dimensions. From the user defined channel height and width, the feature-based design software divides the channel into the correct number of filaments to have a channel width and height as close to the designed value as possible.

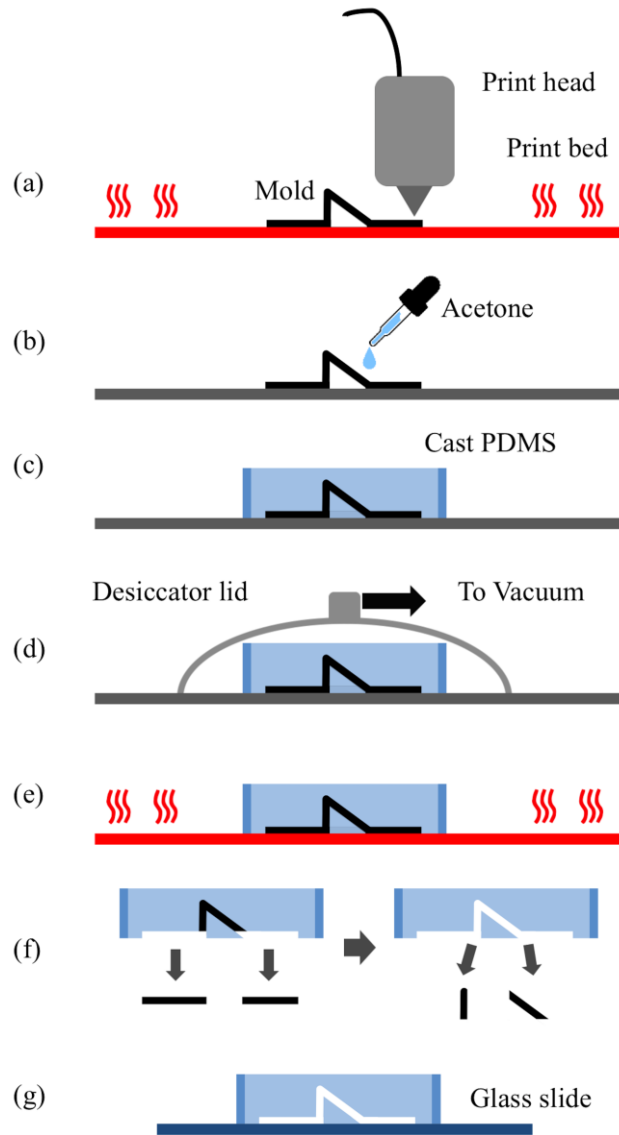


Figure 23 - Fabrication process diagram. (a) The device was printed on a heated print bed. (b) Acetone was applied to the surface of the device to anneal the ABS surface. (c) PDMS was cast over the mold, (d) a vacuum degassed the PDMS, and (e) the heated print bed cured the device. (f) The device was removed from the bed and ABS mold and (g) bound to a glass slide.

Layers of filament that make up the channels were clearly visible and had a rough surface after printing. Surface roughness of the channels was minimized through an acetone solvent annealing treatment. The annealing process was adapted from common 3D printing techniques that use solvents to solubilize the surface of a printed model to smooth out the layering effect of FDM 3D printing. Printed models are exposed to an acetone vapor, within a closed container, to dissolve and smooth the surface. For our process, a small amount of acetone was applied to the surface of the printed channels using a fine-tip paint brush and allowed to evaporate with the print bed set to 50°C to accelerate the process. Temperatures > 50°C caused bubbles in the ABS as the acetone evaporates. Ultimately, this process removes roughness in the surface and smooths individual layers from the printing process Figure 24(a) this improves the optical properties and makes the flow resistance of the channels more uniform.

Applications

To demonstrate the utility of direct write microfluidic designs and 3D microfluidics using our feature-based design utility, common fluidic architectures were designed, printed, assembled, and tested. A gradient generator was fabricated to test the replication of the printing process. Uneven resistance within the bifurcating channels of a gradient generator will cause variations in the concentration gradient, indicating variations between the identically designed channels. The device worked by splitting and recombining channels to form combinations of the two inlet solutions. The five channels recombine in a larger channel where diffusive mixing makes a continuous gradient. Solvent annealing the channels removed microscale irregularities that interfere with laminar flow and uniform gradient formation (Figure 24a). Fluorescence intensity profiles (Figure 24e) show a linear decrease in intensity across the combined flow as a result of combinatorial mixing. Line profiles of the fluorescence in each channel were taken where the numbers indicate in Figure 24b prior to recombination in

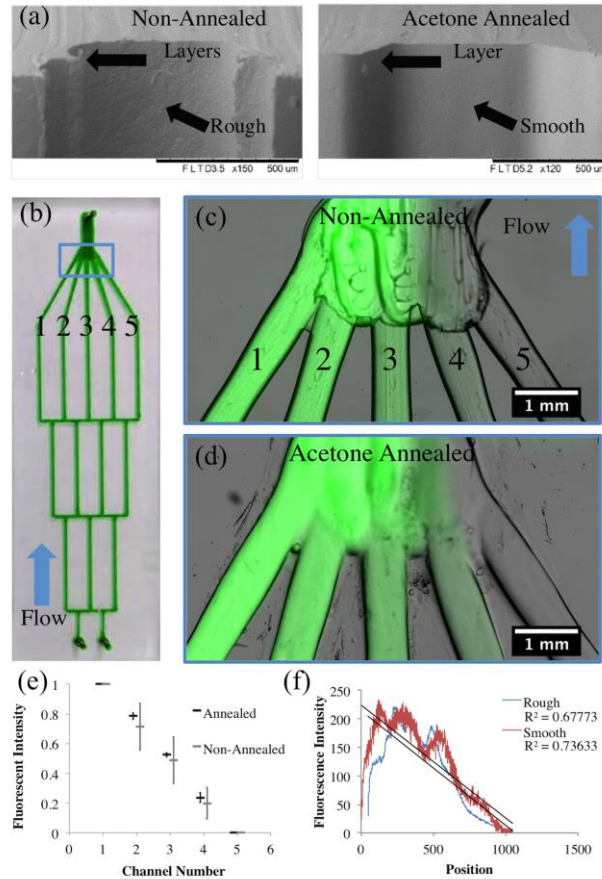


Figure 24 - Acetone annealing gradient generators. (a) SEM images show the surface of the ABS mold annealed by applying acetone. (b) A microfluidic gradient mixer produced using our ABS mold printing process. (c-d) Images of the device show dilution channels recombining. (c) Annealing smooths the surface for more even imaging. (d) Non-annealed device shows rough surfaces from the printing process. (e) The maximum fluorescent intensity from the individual channels prior to rejoining shows greater variability in non-annealed devices. (f) The fluorescent intensity profile in the channels after recombining show the gradient forming. Variation in the chamber height from 3D printing causes variation across the profile deviating from the expected linear gradient.

the final channel. The concentrations of fluorescein in the annealed device show lower variability between devices demonstrated by the standard deviation. The annealed channels had a maximum standard deviation of 0.032, N=3, and the non-annealed channels had a maximum standard deviation of 0.16, N=3. The fluorescence gradient after recombination in the large channel is shown in Figure 24f. The device that was acetone annealed is a better fit to a linear gradient, but the varying thickness of the chamber complicates the optical measurement unlike single filament channels prior to joining together.

Two designs for a droplet generator using both a flow focusing design and a T-junction device were fabricated. Even with larger channel sizes than typical microfluidic droplet generators, the 3D printed designs were able to form droplets consistently. Figure 25a-b shows the completed chips bonded to glass and filled with food coloring as well as the flow-focusing device forming droplets as the oil phase shears off droplets of fluorescein dye. The droplets formed in both devices were shown to vary in size as the flow rate of the oil phase was modulated from 2 μ L/min to 20 μ L/min with a constant flow rate of the aqueous phase at 1 μ L/min. Droplets formed at 20 μ m/min had a volume of 0.14 μ L. These are similar to other droplets formed using 3D printing techniques⁵⁸.

3D Microfluidics

The power of using 3D printers is the ability to create microfluidics that are free to move in all spatial dimensions rather than the planar construction of conventional techniques. Design aspects of 3D printing allow for the fabrication of common designs as well as designs that have unique architectures, however, traditional slicer programs limit the design capabilities by building a device out of multiple layers of material. The feature-based design software writes paths in the z-direction continuously to form structures. This ability was used to create bridges that effectively suspend channels over the printing surface. Figure 26

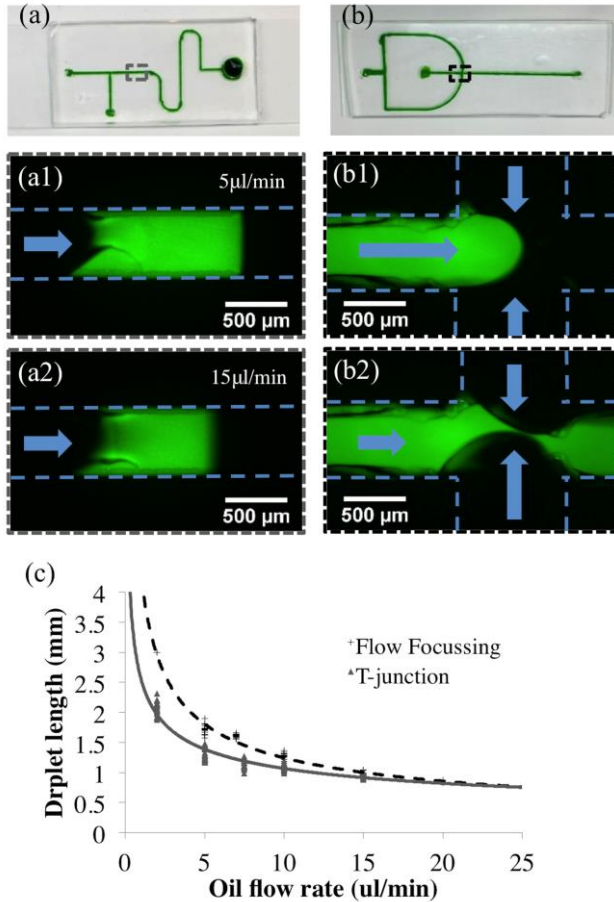


Figure 25 - Droplet generators. (a) The T-junction device was operated with the fluorescein flow rate at $1\mu\text{L}/\text{min}$ and the oil at (a1) $5\mu\text{L}/\text{min}$ and (a2) $20\mu\text{L}/\text{min}$. (b) The flow-focusing device operates with the same flow rates. (b1-2) show the oil channels pinching off a droplet from the fluorescein channel. (c) Formed droplets are highly replicable and can be controlled by altering the oil flow rate from $2\mu\text{L}/\text{min}$ to $20\mu\text{L}/\text{min}$.

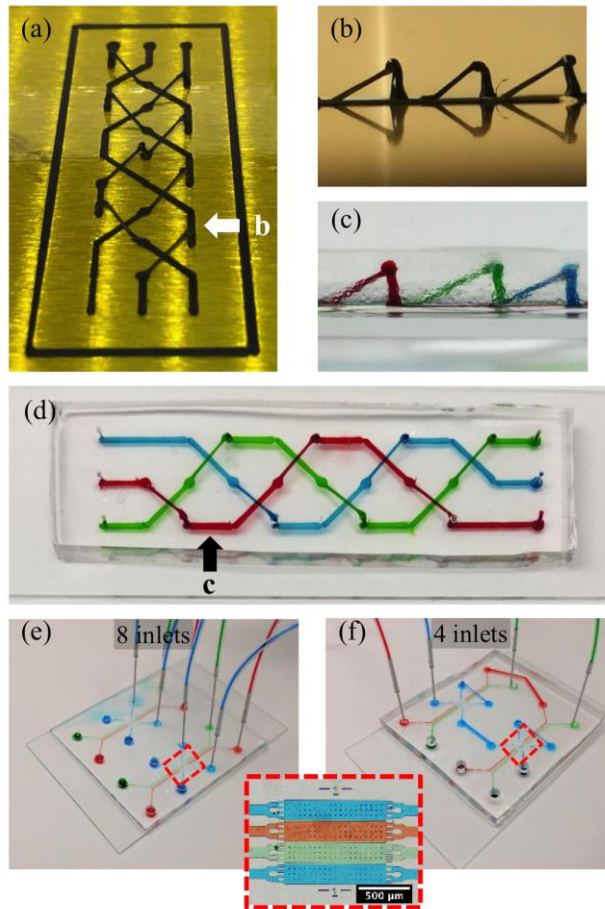


Figure 26 - 3D microfluidics. Using 3D capabilities of the feature-based software, bridges were printed to create an overlapping design with three channels from an offset (a) and side (b) view. (d)Top view - overlapping channels remain separate from one another. (c) Side view - the bridging structure raises off the plane of the glass slide. The expanded view shows the printing direction for the bridging structures. (e) The microfabricated structure along with an inset of the chambers with each channel independent of one another. (f) Shows 3D printed structures connecting channels and overlapping to simplify the device control.

shows bridges created in a braid pattern so that channels can pass across one another without being connected. Extruding a pillar to a height of 3mm, allowing the ABS to solidify for a short time, and extending a filament diagonally down to the final position forms 3D bridge structure. The ABS printed mold is shown in Figure 26(a) with a side view (b). After casting PDMS over the structures, the ABS molds were removed with tweezers leaving internal channels without multiple layers of PDMS. The resulting device was bound to a glass slide to complete the fabrication Figure 26(c-d).

In order to take advantage of the 3D printing without the drawback of lower resolution, 3D printed fluidic networks were combined with microfabricated architectures. These multiscale devices have micro and nanoscale chambers that are routed to one another with 3D printed channels. By 3D printing new networks, the microfabricated devices can be repurposed for multiple experiments without further cleanroom fabrication. Bridges can be incorporated into the design to overlap network channels and simplify fluidic control of the device. Figure 26(e) shows a microfabricated device with eight inlets and eight outlets to individually control each of the four channels of the two devices. Figure 26(f) shows the completed bridged device with the blue and red channels being controlled through a single inlet and outlet. The two green channels remain independent and can be changed between the devices, holding the other chambers constant. This structure can be adjusted to allow for changes in the operation of the device without further cleanroom fabrication.

Conclusions

The feature-based design software and associated method for direct molding PDMS microfluidic devices using an FDM 3D printer was shown to be able to fabricate frequently used microfluidic devices, as well as complex 3D designs that photolithography or micromachining are not capable of. By increasing the accessibility of 3D printed microfluidics, the number of applications

and user base of microfluidics can be broadened. This technology could be adapted to academia for teaching the basics of microfluidics by taking advantage of the ease of use and low cost of the approach. Additional work to develop teaching modules that adjust to the time required to iterate through multiple designs. Our feature-based design utility allows researchers to fabricate microfluidics quickly without the need for cleanroom facilities.

The software interface described here was developed to simplify the design process by giving the user a list of common microfluidic building blocks that can be combined into novel fluidic architectures. The software controls the conversion of the design to g-code to improve control of the printing process. Printing was done using a Solidoodle 4 3D printer, but the Matlab code can be used with any FDM 3D printer running the Marlin firmware. This technique fabricates devices in less time, with lower costs, and with similar results to conventional soft lithographic techniques. The process was shown to be a good alternative to soft lithography and can be integrated with micro and nanofabricated devices to reconfigure systems through 3D fluid networks.

Acknowledgements

This work was supported by NIH award 1R01DE024463-01 Culturing of the Uncultured. This research was performed at Oak Ridge National Laboratory (ORNL). ORNL is managed by UT-Battelle, LLC, for the US Department of Energy Under contract DE-AC05-00OR22725. The fabrication of nano- and microfluidic devices was conducted at the Center for Nanophase Materials Sciences, which is DOE Office of Science User Facilities. JA is supported, in part, by a National Science Foundation Graduate Research Fellowship. There was no additional external funding received for this study.

Appendix

Supporting Information

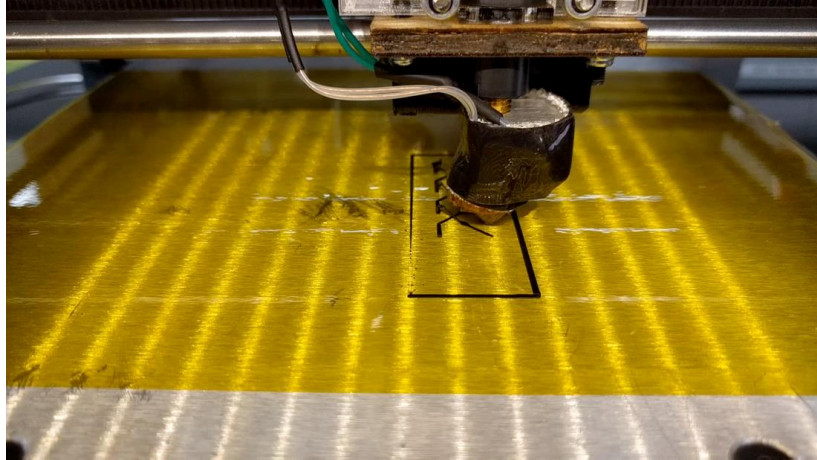



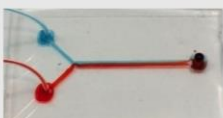



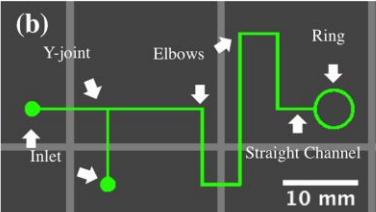


Figure 27 - 3D bridge printing process. The printer extrudes posts, allows them to solidify, and suspends a filament from the post to the print bed. The process is done continuously rather than layer by layer.

| (a) | | |
|------------------|---|---|
| Features | Sample | Parameters |
| Inlet |  | Initial (x,y) Radius Depth |
| Straight Channel |  | Initial (x,y) Final (x,y) Width Depth |
| Corner |  | Initial (x,y) Final (x,y) Corner direction Width, Depth |
| Y-joint |  | Point 1 (x,y) Point 2 (x,y) Point 3 (x,y) Intersection (x,y) Width, Depth |
| Ring |  | Center (x,y) Radius Width Depth |
| 3D Bridge | Top  Side  | Initial (x,y) Final (x,y) Single filament only |

(b)



(c)


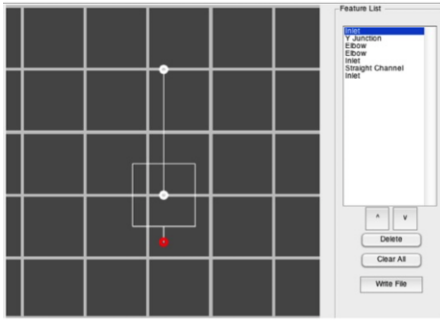
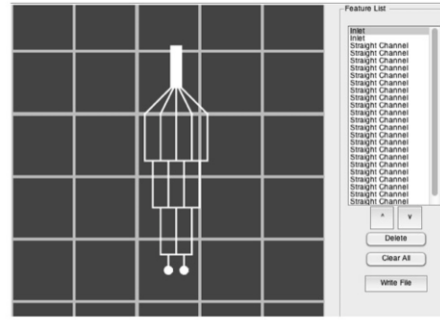


Figure 28 - Feature parameters and part list. Printer parameters for each parameter are shown in (a). Adding parts to a design populates the graphical area (b) as well as the Feature list (c). The order of parts in the list indicates the printing order.

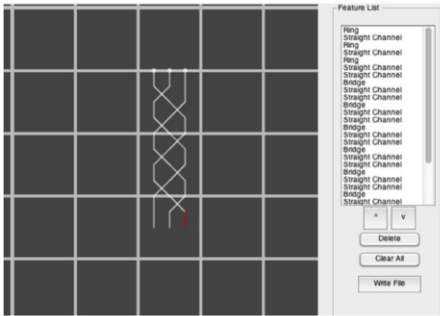
(a) Droplet Generator



(b) Gradient Generator



(c) 3D Bridge Coil



(d) Network Design

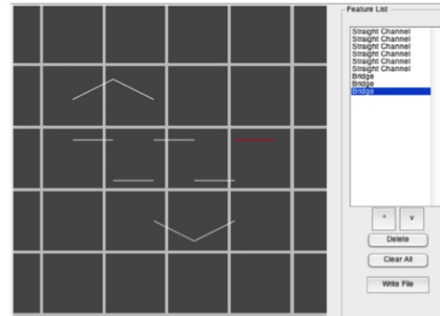


Figure 29 - Device designs used. The completed designs for each device used are shown in the Matlab design environment. The droplet generator (a) and gradient generator (b) show replication of common microfluidic designs. The second droplet generator design is not shown. The coil design (c) and the network architecture (d) were used to show the 3D capabilities of the printing process.

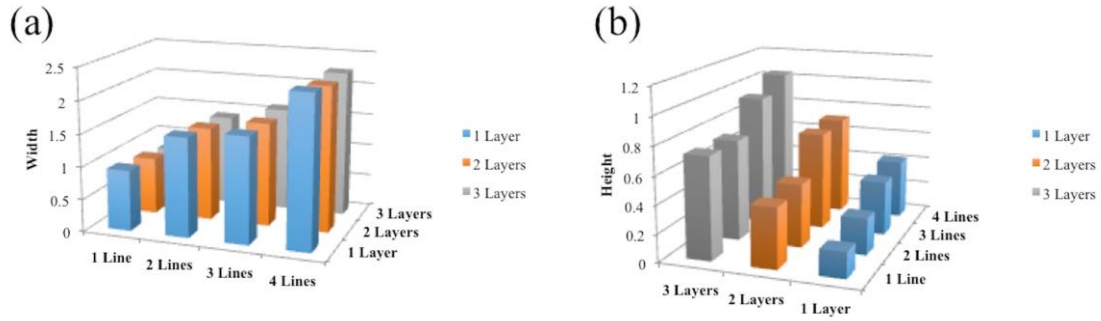


Figure 30 - Printer characterization from the Solidoodle printer used. The number of layers do not affect the width of the channel (a), but the number of lines can affect the height of the channel. The smallest channels were roughly 1mm wide and 200 μ m in height.

CHAPTER 5

CONCLUSION

Biological systems are wonderfully complex and fascinating. Developing an understanding of this complexity is what gives humans the ability to develop new medicines, provide food to sustain a growing population, and hopefully maintain the world we live in. The goal of this thesis was to create microfluidic technologies that allow for more in-depth studies of the natural world. The scale and efficiency of microfluidics provide avenues to enhance the experimental reproduction of the natural world in a way that can be studied. The efficiency of microfluidics was used to enhance the yields in CFPS reactions geared towards point-of-use therapeutic protein production. The scale of microfluidics enhanced culture techniques to study signaling in biofilm formation with nanofluidic barriers. The final target was to provide new technology in design and fabrication to broaden the audience of microfluidics using 3D printing. Separately these concepts touch on different aspects of microfluidics, but together they act to enhance the interface between researchers and natural systems.

The goal of the first project was to optimize the yield of a CFPS system for military applications when the cost of transportation is the limiting factor. Many groups have prioritized a biochemical approach to optimize the utilization of reactants, but we took a reactor-focused approach by concentrating on how the scale of the reactor and chemical exchange can increase the yield of the reaction. The CFPS reaction took place on one side of the reactor while nutrients and energy would be constantly supplied by the adjacent channel. The nanofabricated membrane separating the two channels limited transport between the channels by size exclusion size exclusion. The yield of the system was increased by using microfluidic channels and decreasing diffusion distances, and the yield of the exchange reactor after 8 hours was higher than a commercial

macro scale exchange reactor after 24 hours. The scale of microfluidics alone increased the efficiency of a CFPS reaction in two different reaction setups.

The field of microfluidics is growing and expanding to incorporate new technologies to expand the functionality and scale of fluidics. 3D printing is becoming a prevalent technology used in the fabrication and implementation of microfluidics. 3D printing technology complements microfabrication, excelling in larger scales that microfabrication struggles to obtain. While the concept has been shown, technology specific to 3D printed microfluidics has not been fully developed outside of a few proprietary applications. The proposed workflow and design software provide microfluidic specific design tools and a simple and efficient fabrication process. The purpose of the process is to show what is possible with 3D printers and encourage people to think beyond the layering techniques that are ever present in 3D printing. The bridging structures rely on printing vertically to build 3D structure in a single step rather than layering. The future for 3D printing in microfluidics is not yet defined, but the opportunities are rich.

Biofilms composed of synergistic bacteria rely on each other for survival. The chemical fluxes and gradients that form within a bacterial biofilm change based on the species present as well as the environment. Developing multi scale microfluidics allows for manipulation of the physical environment on multiple levels. Nanoscale pores provide confinement of bacterial cells while providing chemical communication and nutrient transport between cultures. The interactions between spatially separate bacterial species were studied using these microfluidics and were shown to exhibit morphological changes based on the co-cultured species. Characterization of the transport properties of the microfluidic device was done using fluorescent dyes and GFP producing bacteria. Further characterization was done using COMSOL Multiphysics modeling of the production and diffusion of the signal molecule throughout the system. The morphology of the *S. gordonii* cells changed over time when

cultured with autoinducer two producing *F. nucleatum*. Developing a better understanding of the complex interactions within biofilms could influence how we deal with bacterial cultures.

Individually, these chapters act to provide new insights and technology to advance the fields of microfluidics, synthetic biology, microbiology. Together they demonstrate a step forward in interfacing to the natural world. When the spatial structure of the environment is manipulated on the scale of cells or molecules, the synthetic environment can be tuned to replicate aspects of the natural environment or provide access to information not obtainable from nature. Transparent materials allow for high resolution microscopy. The spatial structure replicates natural heterogeneity. Or, interactions between bacteria are controlled, measured, and modeled to build deeper meaning. The multiscale nature of the applications applies to a broad range of biology and broaden the potential applications of microfluidics.

REFERENCES

- 1 G. M. Whitesides, *Nature*, 2006, **442**, 368–373.
- 2 A. Grünberger, W. Wiechert and D. Kohlheyer, *Curr. Opin. Biotechnol.*, 2014, **29**, 15–23.
- 3 S. M. Prakadan, A. K. Shalek and D. A. Weitz, *Nat. Rev. Genet.*, 2017, **18**, 345–361.
- 4 M. Mehling and S. Tay, *Curr. Opin. Biotechnol.*, 2014, **25**, 95–102.
- 5 Y. Gao, D. Majumdar, B. Jovanovic, C. Shaifer, P. C. Lin, A. Zijlstra, D. J. Webb and D. Li, *Biomed. Microdevices*, 2011, **13**, 539–48.
- 6 M. A. Unger, H. P. Chou, T. Thorsen, A. Scherer and S. R. Quake, *Science*, 2000, **288**, 113–6.
- 7 K. Chung, M. M. Crane and H. Lu, *Nat. Methods*, 2008, **5**, 637–643.
- 8 T. V Nguyen, P. N. Duncan, S. Ahrar and E. E. Hui, *Lab Chip*, 2012, **12**, 3991–4.
- 9 P. N. Duncan, T. V Nguyen and E. E. Hui, *Proc. Natl. Acad. Sci. U. S. A.*, 2013, **110**, 18104–9.
- 10 P. N. Duncan, S. Ahrar and E. E. Hui, *Lab Chip*, 2015, **15**, 1360–1365.
- 11 H. Becker and C. Gärtner, *Electrophoresis*, 2000, **21**, 12–26.
- 12 D. C. Duffy, J. C. McDonald, O. J. A. Schueller and G. M. Whitesides, *Anal. Chem.*, 1998, **70**, 4974–4984.
- 13 J. R. Anderson, D. T. Chiu, R. J. Jackman, O. Chemiavskaya, J. C. McDonald, H. Wu, S. H. Whitesides and G. M. Whitesides, *Anal. Chem.*, 2000, **72**, 3158–3164.
- 14 S. Waheed, J.-M. Cabot Canyelles, N. Macdonald, R. M. Guijt, T. Lewis, B. Paull and M. C. Breadmore, *Lab Chip*, , DOI:10.1039/C6LC00284F.
- 15 V. Nock, R. J. Blaikie and T. David, *Lab Chip*, 2008, **8**, 1300.
- 16 R. H. W. Lam, M.-C. Kim and T. Thorsen, *Anal. Chem.*, 2009, **81**, 5918–24.
- 17 M. Skolimowski, M. W. Nielsen, J. Emnéus, S. Molin, R. Taboryski, C. Sternberg, M. Dufva and O. Geschke, *Lab Chip*, 2010, **10**, 2162–2169.
- 18 S. Campopiano, R. Bernini, L. Zeni and P. M. Sarro, *Opt. Lett.*, 2004, **29**,

- 1894.
- 19 K. Grenier, D. Dubuc, P. E. Poleni, M. Kumemura, H. Toshiyoshi, T. Fujii and H. Fujita, in *IEEE MTT-S International Microwave Symposium Digest*, 2009, pp. 1329–1332.
 - 20 A. Groisman, C. Lobo, H. Cho, J. K. Campbell, Y. S. Dufour, A. M. Stevens and A. Levchenko, *Nat. Methods*, 2005, **2**, 685–689.
 - 21 E. D. Carlson, R. Gan, C. E. Hodgman and M. C. Jewett, *Biotechnol. Adv.*, 2012, **30**, 1185–1194.
 - 22 J. F. Zawada, G. Yin, A. R. Steiner, J. Yang, A. Naresh, S. M. Roy, D. S. Gold, H. G. Heinsohn and C. J. Murray, *Biotechnol. Bioeng.*, 2011, **108**, 1570–1578.
 - 23 A. Zemella, L. Thoring, C. Hoffmeister and S. Kubick, *ChemBioChem*, 2015, **16**, 2420–2431.
 - 24 Q. Mei, C. K. Fredrickson, A. Simon, R. Khnouf and Z. H. Fan, *Biotechnol. Prog.*, , DOI:10.1021/bp070133p.
 - 25 K. Madin, T. Sawasaki, T. Ogasawara and Y. Endo, *Proc. Natl. Acad. Sci. U. S. A.*, 2000, **97**, 559–564.
 - 26 J. R. Swartz, *AIChE J.*, 2012, **58**, 5–13.
 - 27 J. A. Stapleton and J. R. Swartz, *PLoS One*, , DOI:10.1371/journal.pone.0015275.
 - 28 P. G. Shankles, A. C. Timm, M. J. Doktycz and S. T. Retterer, *J. Vac. Sci. Technol. B*, 2015, **33**, 06FM03.
 - 29 A. C. Timm, P. G. Shankles, C. M. Foster, M. J. Doktycz and S. T. Retterer, *J. Vac. Sci. Technol. B, Nanotechnol. Microelectron. Mater. Process. Meas. Phenom.*, 2015, **33**, 06FM02.
 - 30 A. C. Timm, P. G. Shankles, C. M. Foster, M. J. Doktycz and S. T. Retterer, *Small*, 2016, **12**, 810–817.
 - 31 S. Sivashankar, S. Agambayev, K. Alamoudi, U. Buttner, N. Khashab and K. N. Salama, *Micro Nano Lett.*, 2016, **11**, 654–659.

- 32 E. K. Sackmann, A. L. Fulton and D. J. Beebe, *Nature*, 2014, **507**, 181–9.
- 33 P. F. O'Neill, A. Ben Azouz, M. Vázquez, J. Liu, S. Marczak, Z. Slouka, H. C. Chang, D. Diamond and D. Brabazon, *Biomicrofluidics*, 2014, **8**, 052112.
- 34 A. K. Au, W. Huynh, L. F. Horowitz and A. Folch, *Angew. Chemie - Int. Ed.*, 2016, **55**, 3862–3881.
- 35 N. Bhattacharjee, A. Urrios, S. Kang and A. Folch, *Lab Chip*, 2016, **16**, 1720–1742.
- 36 W. Gao, Y. Zhang, D. Ramanujan, K. Ramani, Y. Chen, C. B. Williams, C. C. L. Wang, Y. C. Shin, S. Zhang, P. D. Zavattieri and W. Gao, *Comput. Des.*, 2015, **69**, 65–89.
- 37 D. I. Walsh, D. S. Kong, S. K. Murthy and P. A. Carr, *Trends Biotechnol.*, 2017, **xx**, 1–10.
- 38 Y. He, Y. Wu, J. Fu, Q. Gao and J. Qiu, *Electroanalysis*, 2016, 1–22.
- 39 J. C. McDonald, M. L. Chabinyk, S. J. Metallo, J. R. Anderson, A. D. Stroock and G. M. Whitesides, *Anal. Chem.*, 2002, **74**, 1537–1545.
- 40 A. Bonyar, H. Santha, M. Varga, B. Ring and G. Harsanyi, *Int. J. Mater. Form.*, 2014, **7**, 189–196.
- 41 K. Kamei, Y. Mashimo, Y. Koyama, C. Fockenber, M. Nakashima, M. Nakajima, J. Li and Y. Chen, *Biomed. Microdevices*, 2015, **17**, 36.
- 42 Y. Hwang, O. H. Paydar and R. N. Candler, *Sensors Actuators A Phys.*, 2015, **226**, 137–142.
- 43 P. G. Shankles, L. J. Millet, J. A. Aufrecht and S. T. Retterer, *PLoS One*, 2018, **13**, e0192752.
- 44 H. N. Chan, Y. Chen, Y. Shu, Y. Chen, Q. Tian and H. Wu, *Microfluid. Nanofluidics*, 2015, **19**, 9–18.
- 45 C. I. Rogers, K. Qaderi, A. T. Woolley and G. P. Nordin, *Biomicrofluidics*, , DOI:10.1063/1.4905840.
- 46 Z. Li, J. Yang, K. Li, L. Zhu and W. Tang, *RSC Adv.*, 2017, **7**, 3313–3320.

- 47 V. Saggiomo and A. H. Velders, *Adv. Sci.*, 2015, n/a-n/a.
- 48 M. K. Gelber and R. Bhargava, *Lab Chip*, 2015, **15**, 1736–1741.
- 49 G. Comina, A. Suska and D. Filippini, *Lab Chip*, 2014, **14**, 424–30.
- 50 S. Knowlton, C. H. Yu, F. Ersoy, S. Emadi, A. Khademhosseini and S. Tasoglu, *Biofabrication*, 2016, **8**, 025019.
- 51 K. B. Anderson, S. Y. Lockwood, R. S. Martin and D. M. Spence, *Anal. Chem.*, 2013, **85**, 5622–5626.
- 52 A. J. L. Morgan, L. H. San Jose, W. D. Jamieson, J. M. Wymant, B. Song, P. Stephens, D. A. Barrow and O. K. Castell, *PLoS One*, , DOI:10.1371/journal.pone.0152023.
- 53 G. Gaal, M. Mendes, T. P. de Almeida, M. H. O. Piazzetta, ??ngelo L. Gobbi, A. Riul and V. Rodrigues, *Sensors Actuators, B Chem.*, 2017, **242**, 35–40.
- 54 A. I. Shallan, P. Smejkal, M. Corban, R. M. Guijt and M. C. Breadmore, *Anal. Chem.*, 2014, **86**, 3124–30.
- 55 A. Bonyár, H. Sántha, B. Ring, M. Varga, J. G. Kovács and G. Harsányi, in *Procedia Engineering*, 2010, vol. 5, pp. 291–294.
- 56 A. K. Au, N. Bhattacharjee, L. F. Horowitz, T. C. Chang and A. Folch, *Lab Chip*, 2015, **15**, 1934–41.
- 57 O. H. Paydar, C. N. Paredes, Y. Hwang, J. Paz, N. B. Shah and R. N. Candler, *Sensors Actuators, A Phys.*, 2014, **205**, 199–203.
- 58 K. C. Bhargava, B. Thompson and N. Malmstadt, *Proc. Natl. Acad. Sci. U. S. A.*, 2014, **111**, 15013–8.
- 59 K. G. Lee, K. J. Park, S. Seok, S. Shin, D. H. Kim, J. Y. Park, Y. S. Heo, S. J. Lee and T. J. Lee, *RSC Adv.*, 2014, **4**, 32876.
- 60 P. J. Kitson, M. D. Symes, V. Dragone and L. Cronin, *Chem. Sci.*, 2013, **4**, 3099–3103.
- 61 A. Urrios, C. Parra-Cabrera, N. Bhattacharjee, A. M. Gonzalez-Suarez, L. G. Rigat-Brugarolas, U. Nallapatti, J. Samitier, C. A. DeForest, F. Posas, J.

- L. Garcia-Cordero and A. Folch, *Lab Chip*, 2016, **16**, 2287–2294.
- 62 C. M. B. Ho, S. H. Ng, K. H. H. Li and Y. Yoon, *Lab Chip*, 2015, **15**, 3627–3637.
- 63 D. Chudobova, K. Cihalova, S. Skalickova, J. Zitka, M. A. M. Rodrigo, V. Milosavljevic, D. Hynek, P. Kopel, R. Vesely, V. Adam and R. Kizek, *Electrophoresis*, 2015, **36**, 457–466.
- 64 L. Krejcova, L. Nejdil, M. A. M. Rodrigo, M. Zurek, M. Matousek, D. Hynek, O. Zitka, P. Kopel, V. Adam and R. Kizek, *Biosens. Bioelectron.*, 2014, **54**, 421–427.
- 65 B. N. Johnson, K. Z. Lancaster, I. B. Hogue, F. Meng, Y. L. Kong, L. W. Enquist and M. C. McAlpine, *Lab Chip*, 2015, Ahead of Print.
- 66 W. Shumi, J. Lim, S.-W. Nam, K. Lee, S. H. Kim, M.-H. Kim, K.-S. Cho and S. Park, *BioChip J.*, 2010, **4**, 257–263.
- 67 A. Y. Ozkumur, B. a. Goods and J. C. Love, *Small*, 2015, **11**, 4643–4650.
- 68 S. W. Rhee, A. M. Taylor, C. H. Tu, D. H. Cribbs, C. W. Cotman and N. L. Jeon, *Lab Chip*, 2005, **5**, 102–107.
- 69 S. Kim, F. Qiu, S. Kim, A. Ghanbari, C. Moon, L. Zhang, B. J. Nelson and H. Choi, *Adv. Mater.*, 2013, **25**, 5863–5868.
- 70 J. Shemesh, I. Jalilian, A. Shi, G. Heng Yeoh, M. L. Knothe Tate and M. E. Warkiani, *Lab Chip*, 2015, **15**, 1072–1083.
- 71 I. Meyvantsson and D. J. Beebe, *Annu. Rev. Anal. Chem. (Palo Alto, Calif.)*, 2008, **1**, 423–449.
- 72 J. El-Ali, P. K. Sorger and K. F. Jensen, *Nature*, 2006, **442**, 403–411.
- 73 H. Dongeun, D. M. Benjamin, M. Akiko, M.-Z. Martín, Y. H. Hong and E. I. Donald, *Science (80-.)*, 2010, **328**, 1662–1668.
- 74 H. Andersson and A. van den Berg, *Lab Chip*, 2004, **4**, 98–103.
- 75 S. Chung, R. Sudo, P. J. Mack, C.-R. Wan, V. Vickerman and R. D. Kamm, *Lab Chip*, 2009, **9**, 269–275.
- 76 M. R. Bennett and J. Hasty, *Nat. Rev. Genet.*, 2009, **10**, 628–638.

- 77 P. Garstecki, M. J. Fuerstman, H. a. Stone and G. M. Whitesides, *Lab Chip*, 2006, **6**, 437.
- 78 Y. C. Tan, V. Cristini and A. P. Lee, *Sensors Actuators, B Chem.*, 2006, **114**, 350–356.
- 79 S.-Y. Jung, S. T. Retterer and C. P. Collier, *Lab Chip*, 2010, **10**, 2688.
- 80 S. Wang, O. Jeon, P. G. Shankles, Y. Liu, E. Alsberg, S. T. Retterer, B. P. Lee and C. K. Choi, *Biomicrofluidics*, , DOI:10.1063/1.4941339.
- 81 E. Brouzes, M. Medkova, N. Savenelli, D. Marran, M. Twardowski, J. B. Hutchison, J. M. Rothberg, D. R. Link, N. Perrimon and M. L. Samuels, *Proc. Natl. Acad. Sci. U. S. A.*, 2009, **106**, 14195–200.
- 82 J. J. Agresti, E. Antipov, A. R. Abate, K. Ahn, A. C. Rowat, J.-C. Baret, M. Marquez, A. M. Klibanov, A. D. Griffiths and D. A. Weitz, *Proc. Natl. Acad. Sci. U. S. A.*, 2010, **107**, 4004–9.
- 83 R. R. Hansen, A. C. Timm, C. M. Timm, A. N. Bible, J. L. Morrell-Falvey, D. A. Pelletier, M. L. Simpson, M. J. Doktycz and S. T. Retterer, *PLoS One*, 2016, 11.
- 84 J. L. Wilmoth, P. W. Doak, A. Timm, M. Halsted, J. D. Anderson, M. Ginovart, C. Prats, X. Portell, S. T. Retterer and M. Fuentes-Cabrera, *Front. Microbiol.*, 2018, **9**, 1–11.
- 85 P. C. Blainey, *FEMS Microbiol. Rev.*, 2013, **37**, 407–427.
- 86 F. K. Balagadde, L. You, C. L. Hansen, F. H. Arnold and S. R. Quake, *Science (80-.)*, 2005, **309**, 137–140.
- 87 K. S. Lee, P. Boccazzi, A. J. Sinskey and R. J. Ram, *Lab Chip*, 2011, **11**, 1730.
- 88 J. S. Odorico, D. S. Kaufman and J. a Thomson, *Stem Cells*, 2001, **19**, 193–204.
- 89 P. D. Straight and R. Kolter, *Annu. Rev. Microbiol.*, 2009, **63**, 99–118.
- 90 C. M. Waters and B. L. Bassler, *Annu. Rev. Cell Dev. Biol.*, 2005, **21**, 319–346.

- 91 M. R. Parsek and E. P. Greenberg, *Proc. Natl. Acad. Sci. U. S. A.*, 2000, **97**, 8789–93.
- 92 L. Goers, P. Freemont and K. M. Polizzi, *J. R. Soc. Interface*, 2014, **11**, 20140065-.
- 93 Z. Ge, P. R. Girguis and C. R. Buie, *Lab Chip*, 2015, **16**, 480–488.
- 94 M. C. Hesselman, D. I. Odoni, B. M. Ryback, S. de Groot, R. G. A. van Heck, J. Keijsers, P. Kolkman, D. Nieuwenhuijse, Y. M. van Nuland, E. Sebus, R. Spee, H. de Vries, M. T. Wapenaar, C. J. Ingham, K. Schroën, V. A. P. Martins dos Santos, S. K. Spaans, F. Hugenholtz and M. W. J. van Passel, *PLoS One*, 2012, **7**, e36982.
- 95 M. K. Kim, F. Ingremeau, A. Zhao, B. L. Bassler and H. A. Stone, *Nat. Microbiol.*, , DOI:10.1038/nmicrobiol.2015.5.
- 96 A. Meyer, J. A. Megerle, C. Kuttler, J. Müller, C. Aguilar, L. Eberl, B. A. Hense and J. O. Rädler, *Phys. Biol.*, , DOI:10.1088/1478-3975/9/2/026007.
- 97 M. J. Kirisits, J. J. Margolis, B. L. Purevdorj-Gage, B. Vaughan, D. L. Chopp, P. Stoodley and M. R. Parsek, in *Journal of Bacteriology*, 2007, vol. 189, pp. 8357–8360.
- 98 B. Purevdorj, J. W. Costerton and P. Stoodley, *Appl. Environ. Microbiol.*, 2002, **68**, 4457–4464.
- 99 R. D. Lovchik, N. Tonna, F. Bianco, M. Matteoli and E. Delamarche, *Biomed. Microdevices*, 2010, **12**, 275–82.
- 100 M. B. Byrne, L. Trump, A. V Desai, L. B. Schook, H. Rex Gaskins and P. J. a Kenis, *Biomicrofluidics*, 2014, **8**, 044104.
- 101 H. J. Kim, J. Q. Boedicker, J. W. Choi and R. F. Ismagilov, *Proc. Natl. Acad. Sci. U. S. A.*, 2008, **105**, 18188–18193.
- 102 G. Lambert, A. Bergman, Q. Zhang, D. Bortz and R. Austin, *New J. Phys.*, 2014, **16**, 045005.
- 103 S. L. Kuchma and G. A. O’Toole, *Curr. Opin. Biotechnol.*, 2000, **11**, 429–433.

- 104 N. Bagge, M. Schuster, M. Hentzer, O. Ciofu, M. Givskov, E. P. Greenberg and N. Høiby, *Antimicrob. Agents Chemother.*, 2004, **48**, 1175–1187.
- 105 J. K. M. Knobloch, K. Bartscht, A. Sabottke, H. Rohde, H. H. Feucht and D. Mack, *J. Bacteriol.*, 2001, **183**, 2624–2633.
- 106 P. S. Stewart and M. J. Franklin, *Nat. Rev. Microbiol.*, 2008, **6**, 199–210.
- 107 T. K. Wood, A. F. González Barrios, M. Herzberg and J. Lee, *Appl. Microbiol. Biotechnol.*, 2006, **72**, 361–367.
- 108 J. Aufrecht, C. M. Timm, A. Bible, J. L. Morrell-Falvey, D. A. Pelletier, M. J. Doktycz and S. T. Retterer, *Adv. Biosyst.*, 2018, **1800048**, 1–12.
- 109 K. Drescher, Y. Shen, B. L. Bassler and H. a. Stone, *Proc. Natl. Acad. Sci.*, 2013, **110**, 4345–4350.
- 110 J. Kim, H.-D. Park and S. Chung, *Molecules*, 2012, **17**, 9818–9834.
- 111 Y. Yawata, J. Nguyen, R. Stocker and R. Rusconi, *J. Bacteriol.*, 2016, **198**, 2589–2595.
- 112 J. Kim, H.-S. Kim, S. Han, J.-Y. Lee, J.-E. Oh, S. Chung and H.-D. Park, *Lab Chip*, 2013, **13**, 1846.
- 113 K. K. Jefferson, *FEMS Microbiol. Lett.*, 2004, **236**, 163–173.
- 114 B. Manz, F. Volke, D. Goll and H. Horn, *Biotechnol. Bioeng.*, 2003, **84**, 424–432.
- 115 T. Chen, W.-H. Yu, J. Iazard, O. V. Baranova, A. Lakshmanan and F. E. Dewhirst, *Database*, 2010, **2010**, baq013-baq013.
- 116 J. a Aas, B. J. Paster, L. N. Stokes, I. Olsen and F. E. Dewhirst, *J. Clin. Microbiol.*, 2005, **43**, 5721–5732.
- 117 X. Xu, J. He, J. Xue, Y. Wang, K. Li, K. Zhang, Q. Guo, X. Liu, Y. Zhou, L. Cheng, M. Li, Y. Li, Y. Li, W. Shi and X. Zhou, *Environ. Microbiol.*, 2014, **17**, 699–710.
- 118 R. P. Darveau, *Nat. Rev. Microbiol.*, 2010, **8**, 481–90.
- 119 S. R. Vartoukian, R. V Moazzez, B. J. Paster, F. E. Dewhirst and W. G. Wade, *J. Dent. Res.*, 2016, **95**, 1308–1313.

- 120 S. R. Vartoukian, A. Adamowska, M. Lawlor, R. Moazzez, F. E. Dewhirst and W. G. Wade, *PLoS One*, DOI:10.1371/journal.pone.0146926.
- 121 I. Mashima and F. Nakazawa, *J. Bacteriol.*, 2015, **197**, 2104–2111.
- 122 Y. J. Jang, J. Sim, H. K. Jun and B. K. Choi, *Arch. Oral Biol.*, 2013, **58**, 1594–1602.
- 123 G. Cuadra-Saenz, D. L. Rao, A. J. Underwood, S. a Belapure, S. R. Campagna, Z. Sun, S. Tammariello and A. H. Rickard, *Microbiology*, 2012, **158**, 1783–95.
- 124 P. E. Kolenbrander, R. J. Palmer, S. Periasamy and N. S. Jakubovics, *Nat. Rev. Microbiol.*, 2010, **8**, 471–480.
- 125 R. H. W. Lam, X. Cui, W. Guo and T. Thorsen, *Lab Chip*, 2016, **16**, 1652–1662.
- 126 W. C. Nance, S. E. Dowd, D. Samarian, J. Chludzinski, J. Delli, J. Battista and A. H. Rickard, *J. Antimicrob. Chemother.*, 2013, **68**, 2550–2560.
- 127 H. Horn and S. Lackner, *Adv. Biochem. Eng. Biotechnol.*, 2014, **146**, 53–76.
- 128 C. D. Nadell, K. R. Foster and J. B. Xavier, *Plos Comput. Biol.*, 2010, **6**, 9.
- 129 J. G. Scott, A. G. Fletcher, A. R. A. Anderson and P. K. Maini, *PLoS Comput. Biol.*, 2016, **12**, 1–24.
- 130 M. R. Frederick, C. Kuttler, B. A. Hense and H. J. Eberl, *Theor. Biol. Med. Model.*, 2011, **8**, 8.
- 131 V. Janakiraman, D. Englert, A. Jayaraman and H. Baskaran, *Ann. Biomed. Eng.*, 2009, **37**, 1206–1216.
- 132 C. Westerwalbesloh, A. Grünberger, B. Stute, S. Weber, W. Wiechert, D. Kohlheyer and E. von Lieres, *Lab Chip*, 2015, **15**, 4177–4186.
- 133 R. Holdich, S. Kosvintsev, I. Cumming and S. Zhdanov, *Philos. Trans. R. Soc. A Math. Phys. Eng. Sci.*, 2006, **364**, 161–174.
- 134 R. L. Fleischer, P. B. Price and E. M. Symes, *Science*, 1964, **143**, 249–250.

- 135 A. P. Russo, S. T. Retterer, A. J. Spence, M. S. Isaacson, L. A. Lepak, M. G. Spencer, D. L. Martin, R. MacColl and J. N. Turner, *Sep. Sci. Technol.*, 2004, **39**, 2515–2530.
- 136 S. Rahong, T. Yasui, T. Yanagida, K. Nagashima, M. Kanai, G. Meng, Y. He, F. Zhuge, N. Kaji, T. Kawai and Y. Baba, *Anal. Sci.*
- 137 Y. Zeng and D. J. Harrison, *Anal. Chem.*, 2007, **79**, 2289–2295.
- 138 C. C. Striemer, T. R. Gaborski, J. L. McGrath and P. M. Fauchet, *Nature*, 2007, **445**, 749–753.
- 139 L. Zhang, A. V. Melechko, V. I. Merkulov, M. A. Guillorn, M. L. Simpson, D. H. Lowndes and M. J. Doktycz, *Appl. Phys. Lett.*, 2002, **81**, 135–137.
- 140 B. L. Fletcher, E. D. Hullander, A. V. Melechko, T. E. McKnight, K. L. Klein, D. K. Hensley, J. L. Morrell, M. L. Simpson and M. J. Doktycz, *Nano Lett.*, 2004, **4**, 1809–1814.
- 141 J. D. Fowlkes, B. L. Fletcher, E. D. Hullander, K. L. Klein, D. K. Hensley, A. V. Melechko, M. L. Simpson and M. J. Doktycz, *Nanotechnology*, , DOI:10.1088/0957-4484/16/12/063.
- 142 J. D. Fowlkes, E. D. Hullander, B. L. Fletcher, S. T. Retterer, A. V. Melechko, D. K. Hensley, M. L. Simpson and M. J. Doktycz, *Nanotechnology*, , DOI:10.1088/0957-4484/17/22/021.
- 143 R. E. Beck and J. S. Schultz, *Science (80-)*, 1970, **170**, 1302–1305.
- 144 P. Apel, *Radiat. Meas.*, 2001, **34**, 559–566.
- 145 W.-H. H. Chu, R. Chin, T. Huen and M. Ferrari, *J. Microelectromechanical Syst.*, 1999, **8**, 34–42.
- 146 H. D. Tong, H. V. Jansen, V. J. Gadgil, C. G. Bostan, E. Berenschot, C. J. M. Van Rijn and M. Elwenspoek, *Nano Lett.*, 2004, **4**, 283–287.
- 147 P. Siuti, S. T. Retterer, C. K. Choi, J. D. Fowlkes and M. J. Doktycz, *2009 1st Annu. ORNL Biomed. Sci. Eng. Conf. BSEC 2009*, , DOI:10.1109/BSEC.2009.5090477.
- 148 B. R. Srijanto, S. T. Retterer, J. D. Fowlkes and M. J. Doktycz, *J. Vac. Sci.*

- Technol. B Microelectron. Nanom. Struct.*, 2010, **28**, C6P48.
- 149 S. T. Retterer, P. Siuti, C.-K. Choi, D. K. Thomas and M. J. Doktycz, *Lab Chip*, 2010, **10**, 1174–1181.
- 150 P. Siuti, S. T. Retterer and M. J. Doktycz, *Lab Chip*, 2011, **11**, 3523–3529.
- 151 P. Siuti, S. T. Retterer, C.-K. Choi and M. J. Doktycz, *Anal. Chem.*, 2011, **84**, 1092–1097.
- 152 R. Kurita, N. Yabumoto and O. Niwa, *Biosens. Bioelectron.*, 2006, **21**, 1649–1653.
- 153 D. Branton, D. W. Deamer, A. Marziali, H. Bayley, S. A. Benner, T. Butler, M. Di Ventra, S. Garaj, A. Hibbs, X. Huang, others, S. B. Jovanovich, P. S. Krstic, S. Lindsay, X. S. Ling, C. H. Mastrangelo, A. Meller, J. S. Oliver, Y. V Pershin, J. M. Ramsey, R. Riehn, G. V Soni, V. Tabard-Cossa, M. Wanunu, M. Wiggin and J. a Schloss, *Nat. Biotechnol.*, 2008, **26**, 1146–1153.
- 154 P. J. Hung, P. J. Lee, P. Sabounchi, R. Lin and L. P. Lee, *Biotechnol. Bioeng.*, 2005, **89**, 1–8.
- 155 J. E. Keymer, P. Galajda, C. Muldoon, S. Park and R. H. Austin, *Proc. Natl. Acad. Sci. U. S. A.*, 2006, **103**, 17290–17295.
- 156 M. L. Kovarik, P. C. Gach, D. M. Ornoff, Y. Wang, J. Balowski, L. Farrag and N. L. Allbritton, *Anal. Chem.*, 2012, **84**, 516–540.
- 157 P. Wang, L. Robert, J. Pelletier, W. L. Dang, F. Taddei, A. Wright and S. Jun, *Curr. Biol.*, 2010, **20**, 1099–103.
- 158 L. Ma, S. S. Datta, M. A. Karymov, Q. Pan, S. Begolo and R. F. Ismagilov, *Integr. Biol.*, 2014, **6**, 796–805.
- 159 G. Lambert, D. Liao, S. Vyawahare and R. H. Austin, *J. Bacteriol.*, 2011, **193**, 1878–1883.
- 160 R. H. Austin, C. Tung, G. Lambert, D. Liao and X. Gong, *Chem. Soc. Rev.*, 2010, **39**, 1049.
- 161 J. E. Keymer, P. Galajda, G. Lambert, D. Liao and R. H. Austin, *Proc. Natl.*

- Acad. Sci.*, 2008, **105**, 20269–20273.
- 162 A. L. Schaefer, Y. Oda, B. G. Coutinho, D. A. Pelletier, J. Weiburg, V. Venturi, E. P. Greenberg and C. S. Harwood, *MBio*, 2016, **7**, 1–8.
- 163 L. Guo, X. He and W. Shi, *Front. Microbiol.*, 2014, **5**, 1–13.
- 164 K. Brenner, D. K. Karig, R. Weiss and F. H. Arnold, *Proc. Natl. Acad. Sci. U. S. A.*, 2007, **104**, 17300–17304.
- 165 O. Constantin, *Innov. Rom. Food Biotechnol.*, 2009, **5**, 18–22.
- 166 H. C. Flemming and J. Wingender, *Nat. Rev. Microbiol.*, 2010, **8**, 623–633.
- 167 Y.-J. J. Jang, Y.-J. J. Choi, S.-H. H. Lee, H.-K. K. Jun and B.-K. K. Choi, *Arch. Oral Biol.*, 2013, **58**, 17–27.
- 168 J. Merritt, G. Niu, T. Okinaga and F. Qi, *Appl. Environ. Microbiol.*, 2009, **75**, 7725–7733.
- 169 S. Yazdi and A. M. Ardekani, *Biomicrofluidics*, , DOI:10.1063/1.4771407.
- 170 C. M. Timm, R. R. Hansen, M. J. Doktycz, S. T. Retterer and D. A. Pelletier, *Biomicrofluidics*, 2015, **9**, 17–19.
- 171 J. Q. Boedicker, L. Li, T. R. Kline and R. F. Ismagilov, *Lab Chip*, 2008, **8**, 1265–1272.
- 172 J. M. Higgins, D. T. Eddington, S. N. Bhatia and L. Mahadevan, *Proc. Natl. Acad. Sci. U. S. A.*, 2007, **104**, 20496–20500.
- 173 H. Lu, L. Y. Koo, W. M. Wang, D. a. Lauffenburger, L. G. Griffith and K. F. Jensen, *Anal. Chem.*, 2004, **76**, 5257–5264.
- 174 G. Lambert, D. Liao, S. Vyawahare and R. H. Austin, *J. Bacteriol.*, 2011, **193**, 1878–1883.
- 175 R. Weiss and T. F. Knight, in *Lecture Notes in Computer Science*, 2001, vol. 2054, pp. 1–16.
- 176 D. Karig and R. Weiss, *Biotechnol. Bioeng.*, 2005, **89**, 709–718.
- 177 Fluxion, *White Pap.*, 2008, 1–6.
- 178 2012, US00825796.
- 179 C. G. Conant, J. T. Nevill, M. Schwartz and C. Ionescu-Zanetti, *J. Lab.*

- Autom.*, 2010, **15**, 52–57.
- 180 P. J. Lee, N. Ghorashian, T. A. Gaige and P. J. Hung, *J. Lab. Autom.*, , DOI:10.1016/j.jala.2007.07.001.
- 181 V. Sunkara, D.-K. Park, H. Hwang, R. Chantiwas, S. a. Soper and Y.-K. Cho, *Lab Chip*, 2011, **11**, 962–965.
- 182 C. a Schneider, W. S. Rasband and K. W. Eliceiri, *Nat. Methods*, 2012, **9**, 671–675.
- 183 P. S. Stewart, 1996, **40**, 2517–2522.
- 184 S. H. Huang, P. Liu, A. Mokasdar and L. Hou, *Int. J. Adv. Manuf. Technol.*, 2013, **67**, 1191–1203.
- 185 L. Radis, GE Aviation gets FAA Certification for First 3D Printed Jet Engine Part, <https://3dprinting.com/news/ge-aviation-gets-faa-certification-for-first-3d-printed-jet-engine-part/>, (accessed 20 July 2002).
- 186 G. P. Kontoudis, M. V. Liarokapis, A. G. Zisimatos, C. I. Mavrogiannis and K. J. Kyriakopoulos, in *IEEE International Conference on Intelligent Robots and Systems*, 2015, vol. 2015–Decem, pp. 5857–5862.
- 187 Shapeways, <https://www.shapeways.com/>, (accessed 1 February 2017).
- 188 C. Albaugh, Adidas Makes First 3D Shoe Available for Purchase with Exclusive Drop, <http://news.adidas.com/US/Latest-News/adidas-makes-first-3d-shoe-available-for-purchase-with-exclusive-drop/s/7004e8fa-324b-4b71-bc2f-aacf3d61b135>, (accessed 20 July 2002).
- 189 K. Vittayarukskul and A. P. Lee, *J. Micromechanics Microengineering*, 2017, **27**, 35004.
- 190 H. Gong, B. P. Bickham, A. T. Woolley and G. P. Nordin, *Lab Chip*, 2017, **17**, 2899–2909.
- 191 A. M. Tohill, M. Partridge, S. W. James and R. P. Tatam, *J. Micromechanics Microengineering*, 2017, **27**, 35018–35026.
- 192 P. J. Kitson, M. H. Rosnes, V. Sans, V. Dragone and L. Cronin, *Lab Chip*, 2012, **12**, 3267.

- 193 A. K. Au, W. Lee and A. Folch, *Lab Chip*, 2014, **14**, 1294–1301.
- 194 Dolomite Microfluidics, <https://www.dolomite-microfluidics.com/product/fast-microfluidic-prototyping/>, (accessed 1 January 2017).
- 195 H. Kim, Y. Yang, M. Kim, S. W. Nam, K. M. Lee, N. Y. Lee, Y. S. Kim and S. Park, *Adv. Funct. Mater.*, 2007, **17**, 3493–3498.
- 196 L. J. Millet, J. D. Lucheon, R. F. Standaert, S. T. Retterer and M. J. Doktycz, *Lab Chip*, 2015, **15**, 1799–1811.
- 197 D. Irimia, D. A. Geba and M. Toner, *Anal. Chem.*, 2006, **78**, 3472–7.
- 198 L. Cao, X. Zhang, A. Grimley, A. R. Lomasney and M. G. Roper, *Anal. Bioanal. Chem.*, 2010, **398**, 1985–1991.
- 199 J. Atencia, G. a Cooksey and L. E. Locascio, *Lab Chip*, 2012, **12**, 309–16.

APPENDIX

Plasma Bonding Protocol

May 2015

General use protocol for plasma bonding PDMS to glass and silicon.

PDMS to Glass

Process for bonding a PDMS device to a flat glass slide or coverslip

Materials

Fabricated PDMS device

Glass slide or coverslip

Kimwipes

IPA

Scotch tape

Bonding Protocol

- Apply a small amount of IPA to the glass slide or coverslip
- Wipe the glass clean with a Kimwipe
- Cut pieces of tape and use them to cover the side of the glass that will be bound to the device (This may not be possible with thin coverslips)
- Apply tape in the same way to the side of the PDMS device with channels
- Remove the tape from both the glass and the PDMS and place them immediately into the plasma cleaner, supporting them on junk glass slides
- Seal the door and turn on the pump
- ~5 sec. after starting the vacuum, start the plasma generator
- When the vacuum reaches an appropriate pressure, the plasma will ignite
- Adjust the valve to maintain the plasma
- Maintain the plasma for 90 sec.
- Turn off the plasma

- Gently vent the chamber (venting too fast may cause things fly around the chamber)

Remove the glass slide and place it flat on the counter

Remove the PDMS device and immediately apply it to the glass

Use your finger or a pair of tweezers to bond the device completely

Bake at 75°C for 15min.

Plasma Bonding Silicon to PDMS

Process for binding a silicon device to a flat layer of PDMS

Materials

Fabricated silicon device

Flat PDMS slab

Scotch tape

Note: IPA and acetone may be necessary to clean silicon device

Bonding Protocol

- 1) Blow off the silicon device with N₂ to remove any particles
- 2) If pieces of debris remain, rinse with IPA or soak in acetone and rinse with IPA
 - a. Dry with nitrogen
- 3) Cut pieces of tape and use them to cover the side of the PDMS slab that will contact the silicon
- 4) Remove the tape from the PDMS and place the silicon device and PDMS immediately into the plasma cleaner, supporting them on junk glass slides (full wafers can be placed directly in the vacuum chamber)
- 5) Seal the door and turn on the pump
- 6) ~5 sec. after starting the vacuum, start the plasma generator
- 7) When the vacuum reaches an appropriate pressure, the plasma will ignite

- 8) Adjust the valve to maintain the plasma
- 9) Maintain the plasma for 90 sec.
- 10) Turn off the plasma and vacuum pump
- 11) Gently vent the chamber (venting too fast may cause things fly around the chamber)
- 12) Remove the silicon device and place it flat on the counter
- 13) Remove the PDMS slab and immediately apply it to the glass
- 14) Use your finger or a pair of tweezers to bond the device completely
- 15) Bake at 75°C for 15min.

Form 2 3D Printer Operation:

June 2018

Protocol for operating the Form 2 3D printer and post processing the finished prints

Materials

IPA

Wipes for cleaning resin

Operation

- 1) (Note) Contact Peter Shankles if the resin tray needs to be changed
- 2) Design 3D part and export as an STL file
- 3) Load STL file into Preform software and layout print
- 4) Connect computer to the printer and upload the print files
- 5) Follow instructions on the Form 2 touchscreen to start print
- 6) Allow print to finish

Post Processing

- 1) (Note) Clean up drips and spills with IPA and a wipe immediately before the resin cures
- 2) Remove print platform from the printer
- 3) Use tools to pry printed part off of the platform
- 4) Put the print into the IPA bath and wait 10 min, shaking occasionally
- 5) Remove print from the bath and dry with compressed air
- 6) Allow the print to dry completely
- 7) Bake the print in a 60° oven for 1 hr (Room 105)
- 8) Allow the print to cool
- 9) Cure in the UV oven for 1 hour (rotating as needed to fully expose the print)

10) Remove supports and smooth any rough areas with an Exacto knife

PDMS Casting in 3D Printed Molds

August 2018

Protocol for printing molds using the Form 2 3D printer and preparing them for casting PDMS over the channels

Materials

IPA

Wipes for cleaning resin

PDMS

Mold Design Considerations

- Design the fluidic channels in a CAD program with a flat base ~2mm thick to have good rigidity but not use too much resin
- The platform should be large enough to contain the fluidics and have space to seal to a glass slide ~5mm
- Walls to contain the PDMS during curing should be included around the base of the mold ~2mm thick and ~5-10 mm high depending on the desired thickness of the final PDMS device.
- Walls higher than the final PDMS thickness will cause a meniscus to form around the edges of the device and could interfere with optics at the perimeter of the final device.
- When designing a device, keep in mind the final application of the device and plan the size accordingly. Will it fit on a 1x3 slide for microscopy or a coverslip for confocal experiments?
- The design constraints for molded channel dimensions have not been completely explored. Channels below 0.5mm have been achieved, but the roughness of the mold itself may start to interfere with molding below this point.

Mold Preparation

- Follow 3D printing protocol to print and process the mold
- When laying out the mold for printing the supports can usually be arranged only on the back of the mold to reduce the amount and precision required in the postprocessing steps.
- The mold must be fully rinsed, dried, and cured during the postprocessing or residual solvents or polymer will result in sticky PDMS after curing.

PDMS Molding and Bonding

1. Cast mixed PDMS into the mold filling to level with the top of the walls of the mold
2. Degas in a vacuum chamber
3. Cure at 75° C for 1.5 hours
4. Let the mold cool
5. Remove the molded PDMS with a spatula. The mold can then be reused
6. Punch inlets and outlets
7. Plasma bond the PDMS to a glass slide or coverslip
8. If the roughness of the surface is interfering with bonding the surface can be smoothed with additional PDMS following steps 9-
9. Spin uncured PDMS on a 2x3 glass slide
10. Place the channel-side of the molded PDMS down on the PDMS
11. Remove the coated PDMS and place it on a slide or coverslip of desired size and cure
12. If a stronger bond is required, the PDMS can be peeled off and plasma bonded to the glass to form a tight seal

Fluxion Device Fabrication

June 2016

Process for fabrication of well-plate microfluidics and use on the Fluxion Bioflux™.

PDMS Device Fabrication and Bonding to the Bottom of a 48-Well Plate

This is the process for bonding a PDMS nanoporous culture chamber device to the bottom of a 48-well plate and bonding a coverslip to the bottom of the device. Special care must be taken to ensure the proper replication of nanoscale features.

Materials

- 5:1 PDMS
- Silicon mold
- Polystyrene 48-well plate
- 3-APTES

Device Fabrication

- 7) Mix together PDMS and cross linker in a 5:1 ratio
- 8) Cast PDMS over the silicon mold (15 g)
- 9) Degas until bubbles are removed
- 10) Set in a level position and allow to cure at room temperature for 24hr
- 11) Bake at 75°C for 1 hr.
- 12) Cut directly around the device and cut around the device again ~5mm beyond the first cut so that there is no lip when casting the device next time
- 13) Remove the outer ring and carefully remove the PDMS device
- 14) Punch inlets with a 3mm dermal punch

- 15) Place on in a 150mm petri dish with the channels facing up (mark the date on the dish)
- 16) Bake at 75°C for a minimum of 48 hrs.

Well Plate Preparation

- 1) Drill through the bottom of each of the 48 wells with a 3mm drill bit
- 2) Drill out every other space between the wells (12 total for the well plate)
- 3) Use the side of the drill bit to widen the holes between wells
- 4) Use an X-acto knife to remove burrs around each opening

Bonding PDMS to Well Plate

- 1) Plasma clean the prepared well-plate for ~2min
- 2) Mix 100ml of water with 1ml of 3-APTES in a 100ml autoclave bottle.
- 3) Pour 3-APTES mixture into shallow dish and submerge plasma treated well plate
- 4) Allow to sit for at least 40 min
- 5) Remove the well plate and pour off as much water as possible
- 6) Blow off the bottom of the dish with N₂ and set aside to dry the rest of the way
- 7) Remove the PDMS device from the oven and place the channels down onto a 2x3in glass slide and clean the flat surface with tape
- 8) Plasma clean the PDMS device for ~1min
- 9) Remove the device from the glass slide and bond it to the well plate by bringing them into contact
- 10) Remove any bubbles and adhere the device with a pair of tweezers or a roller
- 11) Bake the well plate for 15 min

Bonding Glass Coverslip to Well Plate Device

- 1) Clean enough 25x50mm coverslips to bond each device using IPA

- 2) Place coverslips onto 2x3 glass slides and plasma clean for 2min
- 3) Remove and set aside
- 4) Plasma treat the well-plate device for 1:30
- 5) Remove the device and place on a flat surface
- 6) Quickly and gently bond the coverslips to the device (press the coverslips onto the PMDS device with a pair of tweezers taking care not to press directly onto the culture chambers)
- 7) Place the completed well plate device into the oven for 15min or until it is ready to be used

***E. coli* 502/503 Signaling in Microfluidic Culture Chambers Protocol**

June 2015

Protocol for running cell interaction experiments in the dual chamber microfluidic culture platform. This protocol work with engineered sender and receiver strains of *E. coli* to determine the interactions across a nanofluidic barrier.

Microbe Culture

Process for culturing microbes for use in culture devices

Materials

Fabricated PDMS device (see microbe culture chamber fab protocol)

LB media

M9 media

Kanamycin (50mg/ml stock)

IPTG (1M stock)

15ml. centrifuge tubes

1ml. BD syringes

30G blunt tip needles

Small diameter Tygon tubing

Syringe pump

502/503 plates

Inoculation loops

Kimwipes

Day 1: Media and Device Prep

Media

- Aliquot 10ml of LB and M9 into two 15ml centrifuge tubes

- Add 10 μ l of Kanamycin and IPTG stocks to each of the tubes
 - a. Final concentrations
 - i. 50 μ g/ml Kanamycin
 - ii. 1 mM IPTG

Device Prep

- 1) Attach a needle tip to 2 syringes and fit a length of Tygon tubing over each needle
- 2) Fill the syringe with 0.5ml of prepared M9 media
- 3) Connect the outlet of each nutrient channel with one of the culture chambers as shown in the figure below using a short length of Tygon tubing.
- 4) Load the syringes into the syringe pump and prime the system by pumping at 30 μ l/min until a droplet forms at the end of each tube.
- 5) Stop the syringe pump and connect the tubes to nutrient channels

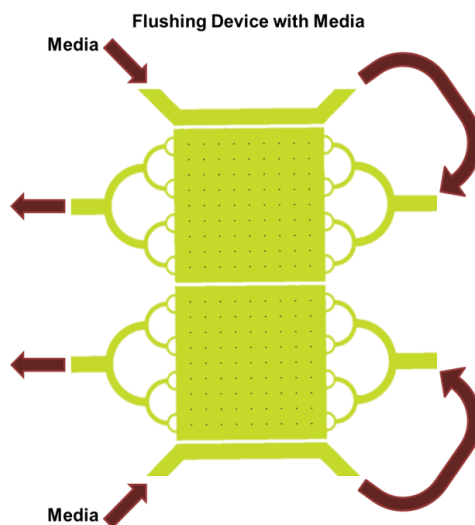


Figure 31 - Fluidic connections and flow direction during priming.

- 6) Start the pump with a rate of 10 μ l/hr. and allow to run overnight.
- 7) Store remaining media at 4°C.

Day 2: Experiment

Culture

- 1) Remove media from the fridge and add 2ml of prepared LB media to two 15ml centrifuge tubes.
- 2) Inoculate the tubes with *E. coli* 502/503 strains using inoculation loop.
- 3) Place the tubes in a shaker incubator at 37°C for 1hr.
- 4) After one hour, remove the tubes from the incubator. Centrifuge at 2500rpm for 5 min.
- 5) Pour off supernatant and replace with 2ml of prepared M9 media.

Plate Reader

- 1) Load 100 μ l samples into a 384 well plate with the layout shown below.
 - a. Co-Culture samples are 50 μ l of 502 and 50 μ l of 503 culture.
 - b. All wells are with M9 media, not LB
 - c. Position within the plate not important. Leave one blank space to reduce possible signal bleeding

Table 2 - Microwell plate layout for baseline 502 and 503 growth and fluorescence.

| | | | | | | |
|-------|-----|-----|-----|-----|-----|------------|
| Blank | Air | 503 | Air | 502 | Air | Co-Culture |
| Blank | Air | 503 | Air | 502 | Air | Co-Culture |
| Blank | Air | 503 | Air | 502 | Air | Co-Culture |

- 2) Plate reader protocol: Fluorescence_absorbance_timeseries
- 3) Change protocol to include the correct wells
- 4) Change plate layout to match
- 5) Run experiment (log the time in the google calendar so that others know)

Device

- 1) Remove the short lengths of tubing that redirected flow from the nutrient channel outlets to the chamber outlets.
- 2) Attach a blunt needle tip and Tygon tubing to two syringes.
- 3) Draw 200-300µl of 502 and 503 culture into the prepared syringes.
- 4) Prime the syringes by pressing the plunger until a droplet formed at the tip.
- 5) Insert the tubing into the culture chamber inlets. The figure below shows the flow.

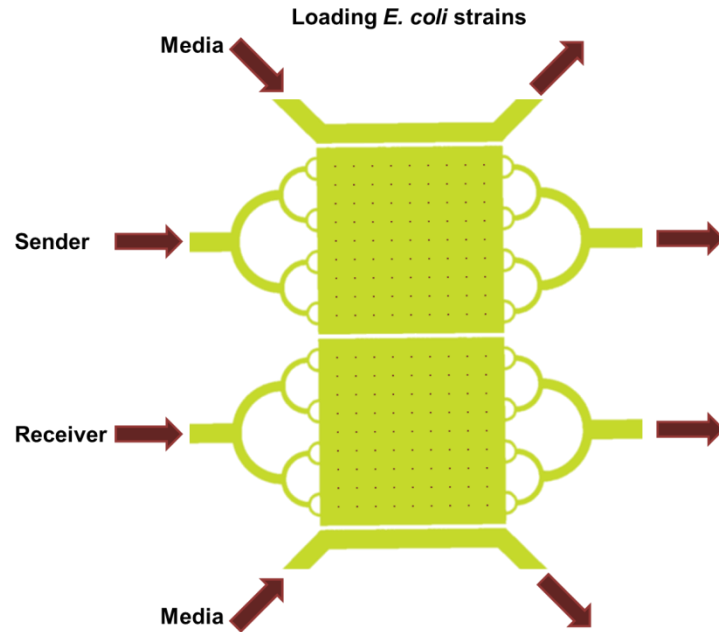


Figure 32 - Fluidic connections and flow direction during experiment.

- 6) Monitor loading with a microscope.
- 7) Adjust the syringes to achieve a slow flow of cells through the device.
- 8) To start the experiment, cut both culture tubes just above the inlet. This stops flow without causing negative pressure associated with pulling out the tubes.
- 9) At this point, the media channels should be the only part with flow.
- 10) Take a phase contrast image and a FITC image every 15min.
- 11) Continue to take images over a 6 hour period.

Protocol for Analyzing Cell Chamber Pictures

May 2015

This protocol covers early analysis that was done on cell culture images of culture chambers. Current protocols were covered in chapter 4.

Required Software

ImageJ (FIJI)

StackReg (<http://bigwww.epfl.ch/thevenaz/stackreg/>)

TurboReg (<http://bigwww.epfl.ch/thevenaz/turboreg/>)

Bright Field Images for OD Measurements

- 1) Stack pictures
 - a. Highlight in folder and drag and drop them into Image J
 - b. Image -> Stack -> Images to stack
 - i. If the last picture is put on the front of the stack
 - ii. Image -> Stack -> Delete Slice
 - iii. Drag and drop the last picture into imagej
 - iv. Image -> Stack -> Tools -> Concatenate...
 - v. Hit enter
 - vi. Save the stack
- 2) Align Images
 - a. Plugins -> StackReg
 - b. Hit enter
- 3) Set Threshold
 - a. Image -> Adjust -> Threshold...
 - b. Adjust limits until the background is removed
 - c. Apply black and white filtering
- 4) Remove any features that bled through the threshold with the paintbrush

- 5) Select each chamber taking care to not include white space and the edge of the image
- 6) Measure Areas
 - a. Analyze -> Measure
 - b. Do this for each slice (press m)
 - c. Copy into Excel
- 7) Get percent area covered
 - a. $\text{area} = 1 - (\text{average intensity}) / 255$
 - i. For 8-bit images
- 8) Graph

FITC Images for Signal Response

- 1) Stack pictures as before
- 2) Align images
 - a. Plugins -> StackReg
 - b. Hit enter
- 3) Select each chamber taking care to not include the edge of the image
- 4) Measure the intensity of the chamber
 - a. Analyze -> Measure
 - b. Do this for each slice (press m)
 - c. Copy into Excel
- 5) Remove background
 - a. Average intensity of 503 chamber – average intensity of 502 chamber
 - b. Do this for each time point
- 6) Normalize the intensity for cell density
 - a. Removed background intensity / %area for 503 BF images
- 7) Graph

VITA

Peter Shankles was born in Knoxville, TN to Roland and Karen Shankles. He completed his undergraduate studies at Georgia Institute of Technology in Atlanta, GA with a degree in Polymer, Textile, and Fiber Engineering. While there, he participated in fluid mechanics research under Dr. Hu studying the effects of rain and fog on mosquito flight. He also taught Matlab as a teaching assistant for eight semesters and led a physics lab for a semester. In addition, he sat as the programs coordinator for a residence hall on campus. After graduation, he traveled back to Knoxville to pursue a Ph.D. in Energy Science and Engineering in the Bredesen Center and The University of Tennessee with a graduate minor in computational sciences. His research work was advised by Dr. Scott T. Retterer studying microfluidics with a focus on enhancing the applications of microfluidics for biological-based studies.